

**THE THERMAL DECOMPOSITION OF BIOFUELS IN A HEATED
MICRO-REACTOR: KETONES, CARBOHYDRATES, AND ESTERS**

by

Jessica Paige Porterfield

B.S., University of Oklahoma, 2010

A thesis submitted to the
Faculty of the Graduate School of the
University of Colorado in partial fulfillment
of the requirement for the degree of
Doctor of Philosophy
Department of Chemistry and Biochemistry

2016

This thesis entitled:
THE THERMAL DECOMPOSITION OF BIOFUELS IN A HEATED MICRO-REACTOR:
KETONES, CARBOHYDRATES, AND ESTERS
by Jessica Paige Porterfield

has been approved for the Department of Chemistry and Biochemistry

G. Barney Ellison

Mark Nimlos

Date _____

The final copy of this thesis has been examined by the signatories, and we find that both the content and the form meet acceptable presentation standards of scholarly work in the above mentioned discipline.

Porterfield, Jessica Paige (Ph. D., Chemistry [Physical Organic])

THE THERMAL DECOMPOSITION OF BIOFUELS IN A HEATED MICRO-REACTOR:
KETONES, CARBOHYDRATES, AND ESTERS

Thesis directed by Professor G. Barney Ellison

Abstract

This thesis describes the thermal, unimolecular decomposition pathways of the following potential biofuels: cyclohexanone ($C_6H_{10}=O$), glycolaldehyde ($HCOCH_2OH$), methyl acetate (CH_3COOCH_3), and methyl butanoate ($CH_3CH_2CH_2COOCH_3$) as well as many products of their decomposition. These fuels have been diluted in a buffer gas (less than 0.1% in He, Ne, Ar, or Kr) and decomposed in a heated micro-reactor. The micro-reactor is a resistively heated silicon carbide (SiC) tube that can be heated to temperatures of up to 1800 K; it is 2 - 3 cm long and 0.6 to 1 mm in diameter. Residence times in the tiny reactor are roughly 25 - 150 microseconds. As the gas mixture exits the reactor, it expands supersonically into a vacuum chamber (1×10^{-6} Torr), which effectively quenches any further chemistry. Mass data of the products are provided by both tunable synchrotron photoionization mass spectrometry (PIMS) conducted at Lawrence Berkeley National Laboratory's Advanced Light Source, and by pulsed, 10.487 eV PIMS conducted at the University of Colorado. Vibrational spectra are collected utilizing matrix isolation infrared spectroscopy (IR). Attempts to validate computational results of pressure within the reactor are also discussed, in which X-ray fluorescence studies were conducted inside the reactor using Kr as a fluorescent tag. With internal temperature and pressure characterized, the micro-reactor will also be a useful tool in determining rate constants of decomposition reactions. The complementary diagnostics of PIMS and IR detect all of the atoms, metastables, and radicals that results from pyrolysis of these fuels. Chemical decomposition pathways are then constructed to justify the observed product distribution.

Dedicated to my parents, Dr. Garland and Winnie Porterfield

Acknowledgements

I'd like to give thanks to a number of people that also participated in the completion of this thesis. I could never thank my family, Garland and Winnie Porterfield and Katelyn Hudson, enough for their support. I'm eternally grateful for their guidance and love. I owe a huge thank you to Dr. Kimberly Urness, who trained me on all of the equipment in the Ellison lab. I'd also like to thank Dr. Josh Baraban and Dr. Grant Buckingham, excellent members of the Ellison group who helped me complete a number of projects. I want to say thank you to Dr. Margaret Asirvatham, Dr. Veronica Bierbaum, and Dr. Nabilah Carlon Rontu who encouraged and gave me many opportunities to explore teaching. I'd like to thank the machine shop for their never ending support, Don David, Ken Smith, Jim Kastengren, Wayne Winkler, and Yehor Novikov. I'd like to thank Dr. John Daily, Dr. John Stanton, and Dr. Robert Tranter for their research mentorship. I'd like to thank Dr. Barney Ellison for taking me under his wing and being a fun, tough loving, unbelievably bright and enthusiastic mentor over the last three years. I wouldn't have made it through the first two years without the help of the incoming class in Physical Chemistry 2011. Last but certainly not least, I'd like to thank all of my friends for their tremendous support throughout this process.

Contents

Abstract	iii
1 Introduction to Biofuel Pyrolysis	1
1.1 The Study of Biofuels	1
1.2 Pyrolysis Experiments	2
1.2.1 The Micro-Reactor	2
1.2.2 Photoionization Mass Spectrometry	5
1.2.3 Matrix Isolation Infrared Spectroscopy	7
1.3 Additional Projects	8
1.3.1 Methyl Allyl Radical Generation	8
1.3.2 Synchrotron Studies	10
2 Cyclohexanone	12
2.1 Introduction	12
2.2 Plausible Decomposition Pathways	13
2.3 Secondary Decomposition	16
2.4 Results	18
2.4.1 Theoretical Thermochemistry	18
2.4.2 Photoionization	20
2.4.3 Product Identification with Tunable VUV Radiation	21
2.4.4 Matrix Infrared Absorption Spectroscopy	28
2.4.5 H-Atom Catalysis	29
2.4.6 Discussion	31

2.5	Supporting Information	37
2.6	Supplemental Figures and Schemes	40
3	Glycolaldehyde	45
3.1	Introduction	45
3.2	Pyrolysis Experiments	45
3.3	Heat of Formation of Glycolaldehyde	47
3.3.1	Calorimetry	47
3.3.2	Experimental Heat of Formation of Glycolaldehyde	48
3.3.3	Electronic Structure Calculations	52
3.3.4	Molecular Structure Results	52
3.4	Ionization Energy of Glycolaldehyde	54
3.5	Results of Glycolaldehyde and Glyoxal Pyrolysis	56
3.6	Conclusions	66
3.7	Supporting Information	69
4	Methyl Esters	74
4.1	Introduction	74
4.2	Experimental	75
4.3	Plausible Decomposition Pathways	76
4.3.1	Methyl Acetate	76
4.3.2	Methyl Butanoate	78
4.4	Results	81
4.4.1	Methyl Acetate	81
4.4.2	Methyl Butanoate	82
4.5	Discussion	95
4.6	Conclusions	102
5	X-ray Fluorescence Studies	104
5.1	Introduction	104
5.2	Experimental	105

5.2.1	X-ray diagnostics	107
5.3	Results	110
5.4	Conclusions	113

List of Schemes

1.1	Synthesis of 3-methylbut-3-enyl nitrite, and 2 possible decomposition pathways. . . .	9
2.1	Possible pathways for cyclohexanone pyrolysis	14
2.2	Decomposition of cyclohexanone via α , β , and γ cleavage	16
2.3	Further decomposition of primary products from cyclohexanone pyrolysis.	17
2.4	Predicted cyclohexanone d_0 and d_4 H/D atom chemistry with H catalysis.	31
2.5	Diradical disproportionation pathways for cyclohexanone	34
2.6	Supplemental: Cyclohexanone dissociative ionization scheme	40
2.7	Supplemental: Methyl vinyl ketone dissociative ionization scheme	43
3.1	Ground and excited states of the $\text{CHO}-\text{CH}_2\text{OH}^+$ cation	56
3.2	Unimolecular decomposition of glycolaldehyde	58
3.3	H atom chemistry with glycolaldehyde	60
3.4	Dissociative ionization of glycolaldehyde	61
4.1	Transesterification of triglycerides in methanol to produce fatty acid methyl esters .	75
4.2	Alcohol and radical fragmentation in the pyrolysis of methyl acetate	77
4.3	Part 1: Decomposition pathways of methyl butanoate	79
4.4	Part 2: Decomposition pathways of methyl butanoate	80
4.5	Part 3: Decomposition pathways of methyl butanoate	80

List of Figures

1.1	The size and setup of the SiC micro-reactor	4
1.2	Photo of the silicon carbide micro-reactor in a pulsed valve assembly	4
1.3	Photoionization mass spectrometry experimental configuration	6
1.4	Matrix isolation infrared spectroscopy experimental setup.	7
2.1	Pulsed PIMS of heated cyclohexanone in He at 10.487 eV	21
2.2	Cyclohexanone pyrolysis products arising from radical disproportionation	22
2.3	Continuous PIMS of heated cyclohexanone at 9.7 eV	24
2.4	Continuous PIMS of cyclohexanone at 10.1 eV, PIE(m/z 41), and PIE(m/z 42) . . .	25
2.5	Continuous PIMS of heated methyl vinyl ketone at 10.0 eV	26
2.6	PIE (m/z 70) from heated methyl vinyl ketone	26
2.7	PIEs from heated methyl vinyl ketone of m/z 15, m/z 26, and m/z 42	27
2.8	PIMS of heated cyclohexanone in He at 10.7 eV and 11.8 eV	28
2.9	Infrared spectrum of heated cyclohexanone in Ar, evidence for ethylene, methyl vinyl ketone, and allyl radical	29
2.10	Infrared spectrum of heated cyclohexanone in Ar, evidence for acetylene, ketene, allene, and carbon monoxide	30
2.11	PIMS of cyclohexanone d_0/d_4 crossover experiment at 10.487 eV	32
2.12	Supplemental: PIE(m/z 26) and PIE(m/z 28) from cyclohexanone at 1200 K	41
2.13	Supplemental: Cyclohexanone 1200 K PIE(m/z 15) and PIE(m/z 54)	41
2.14	Supplemental: PIMS of 1-butene at 10.487 eV	42
2.15	Supplemental: PIMS of cyclopentane at 10.487 eV	42
2.16	Supplemental: PIMS of 1,3-butadiene at 10.487 eV	44

3.1	Chemical structures of glyceraldehyde and glycolaldehyde.	46
3.2	Structures of the <i>trans</i> -glycolaldehyde dimers.	46
3.3	Molecular structures for 1A glycolaldehyde that result from CCSD(T) electronic structure calculations of the molecular geometry of CHO-CH ₂ OH	53
3.4	PIE of m/z 60 from heated glycolaldehyde	55
3.5	Pulsed PIMS of heated glycolaldehyde in He at 10.487 eV	59
3.6	Infrared spectrum of heated glycolaldehyde, evidence for CH ₂ =O and CHO-CHO	64
3.7	Infrared spectrum of heated glycolaldehyde in Ar, evidence for CH ₂ =C=O	65
3.8	PIMS of heated glyoxal in He at 10.487 eV	66
3.9	Infrared spectrum of heated glyoxal trimer dihydrate in Ar. Evidence for glyoxal decomposition to carbon monoxide at 1500 K	67
4.1	PIMS of 0.07% methyl acetate heated to 1600 K	84
4.2	Infrared spectrum of 0.13% methyl acetate heated to 1500 K, ketene ν_1 , ν_2 and ν_4	85
4.3	Infrared spectrum of 0.13% methyl acetate heated to 1500 K, evidence for methanol ν_3 and ν_8	86
4.4	Infrared spectrum of 0.13% methyl acetate heated to 1500 K, formaldehyde ν_1 , ν_2 , and ν_3	87
4.5	Infrared spectrum of 0.13% methyl acetate heated to 1500 K, evidence for carbon monoxide and carbon dioxide	88
4.6	Photoionization mass spectrum of 0.06% methyl butanoate in helium heated to 1600 K in the micro-reactor.	90
4.7	Photoionization mass spectrum at 10.487 eV (118.2 nm) of 0.07% propene heated in helium up to 1500 K.	91
4.8	Matrix infrared spectrum of 0.13% methyl butanoate heated in argon to 1000 K and 1600 K. An authentic sample of methanol is shown in blue.	92
4.9	Matrix infrared spectrum of 0.13% methyl butanoate heated in argon to 1100 K and 1600 K.	93
4.10	Matrix infrared spectrum of 0.13% methyl butanoate heated in argon to 1000 K, 1200 K and 1600 K. Evidence for acetylene HCCH.	94

4.11	Matrix infrared spectrum of 0.13% methyl butanoate heated in argon to 1300 K and 1600 K. Evidence for propene $\text{CH}_3-\text{CH}=\text{CH}_2$	96
4.12	Matrix infrared spectrum of 0.13% methyl butanoate heated in argon to 1000 K, 1300 K and 1600 K.	97
4.13	Matrix infrared spectrum of 0.13% methyl butanoate heated in argon to 1000 K and 1600 K. An authentic sample of ketene $\text{CH}_2=\text{C}=\text{O}$ is shown in blue for reference. . .	98
4.14	Matrix infrared spectrum of 0.13% methyl butanoate heated in argon to 1000 K and 1600 K.	99
5.1	The experimental geometry for X-ray studies of Kr fluorescent tags in the microreactor	106
5.2	The experimental geometry for X-ray studies of Kr fluorescent tags in the microreactor	108
5.3	Example of fluorescence signal from 15 keV X-rays, used to penetrate the SiC walls and ionize Kr inside the tube.	109
5.4	Radiograph of the SiC tube	111
5.5	Absorption raster scans of SiC tube #1 300 ad 1090 K	111
5.6	Krypton fluorescence images captured simultaneously with the absorption images . .	112
5.7	Kr density as a function of reactor length	113
5.8	Composite image of Kr fluorescence and X-ray absorption data	114
5.9	Composite image of Kr fluorescence and X-ray absorption data	114

List of Tables

1.1	Summary of biofuel pyrolysis experimental conditions	5
2.1	Thermochemistry of cyclohexanone and related species	15
2.2	Calculated heats of formation of methyl vinyl ketone and <i>s-trans</i> -1-enol from isodesmic reactions	19
2.3	Calculated thermal correction energies and heats of formation of methyl vinyl ketone at 298 K	19
2.4	Cyclohexanone ionization energies of important organics	23
2.5	Summary of detected products from pyrolysis of cyclohexanone at 1200 K	35
2.6	Supporting information on atomization energy and heat of formation calculations for cyclohexanone	39
3.1	Glycolaldehyde thermochemistry and ionization energy of important organics	57
3.2	Vibrational frequencies and assignments for glycolaldehyde	63
3.3	Supporting information for electronic structure calculations of glycolaldehyde	69
3.4	Supporting information for rotation-vibration corrections for electronic structure calculations of glycolaldehyde	70
3.5	Supporting information for the fitted geometries for electronic structure calculations of glycolaldehyde	71
4.1	Methyl esters experimental, calculated, and estimated thermochemistry part I	77
4.2	Methyl esters experimental, calculated, and estimated thermochemistry part II	78
4.3	Methyl esters mass and ionization energies of important organics	83
4.4	Summary of observed methyl acetate pyrolysis products	95

4.5	Summary of observed methyl butanoate pyrolysis products	100
5.1	X-ray fluorescence experimental conditions	107

Chapter 1

Introduction to Biofuel Pyrolysis

1.1 The Study of Biofuels

The main focus of this thesis is to determine exactly how biofuels decompose under intense heat. Biofuels are fuels derived from living organisms, usually plant-like matter, that consume CO₂ during growth. Biomass based fuels form a closed, carbon neutral cycle, in which excess CO₂ from combustion is recycled through the growth of renewable biomass. The exact environmental consequences of massive anthropogenic CO₂ emissions are currently uncertain. We do know, however, that CO₂ is a strong infrared absorber. This means that when sunlight hits CO₂ its temperature quickly rises, as opposed to N₂ which composes over 70% of our atmosphere and is infrared inactive.

Solar and hydrogen powered vehicles are carbon neutral solutions capable of replacing fossil fuel powered vehicles, however affordable consumer options are still being developed. In the interim, the search continues for liquid renewable fuels that can replace fossil fuels in their existing infrastructure. This replacement needs to be capable of being produced in extremely large quantities. Transportation accounts for about one quarter of the total energy used according to the Department of Energy. Domestic airline fuel consumption was 4×10^{10} liters in 2015 alone. Biomass is the only renewable source of carbon-based fuel that is capable of meeting such a demand. In this thesis, I have studied the thermal decomposition of three potential biofuels, as well as many stable products of their decomposition. Cyclohexanone, described in Chapter 2, is a second generation biofuel derived from ligno-cellulosic biomass, or woody crops and agricultural waste [118]. Glycolaldehyde, described in Chapter 3, is a carbohydrate (C*H₂O)_n, one of the most abundant biomass materials on earth [117].

In Chapter 4, I discuss the decomposition of esters, a class of compounds that have potential as biodiesel and can be derived from the membranes of biological species such as micro-algae.

The mechanisms I have derived for the decomposition of these potential biofuels are far from the entire story. I focus on the decomposition initiation processes that happen within the first 25-150 microseconds of pyrolysis (thermal degradation in the absence of oxygen). In a standard diesel engine, chemistry is initiated by compression ignition - a piston compresses air creating a huge temperature and pressure spike, at which time fuel is injected and ignites. This ignition releases a cascade of highly reactive species called radicals, or chemical species possessing unpaired electrons. Also present in the engine will be short lived products that are thermally unstable, called metastables, which will rapidly decompose to radicals or more stable species. Radicals initiate the remaining chemistry, reacting with the starting material, oxygen, each other, and other intermediates. The final products are exhausted from of the engine within a few milliseconds, and the process immediately. The amount of heat released during that process, and therefore the engine efficiency, is highly dependent upon the chemical reactions that take place during that short time period.

If we are to develop efficient, low emission combustion devices, then a quantitative description of these chemical processes is essential. Computational modelers are currently working to replicate experimental observations of fuel decomposition. This requires taking into account hundreds of reactive intermediates and thousands of potential reaction combinations, a majority of which have not been characterized experimentally. My goal is to identify every species of decomposition, whether it be a stable, metastable, or radical intermediate, one biofuel at a time. Mixtures of biofuels with oxygen (or each other) is the next step, however it is currently too complex to study without understanding the simpler, primary reaction mechanisms. The silicon carbide micro-reactor, described in detail in the next section, has been carefully designed to isolate and identify highly reactive species produced in the first 25 - 150 μ seconds of fuel decomposition.

1.2 Pyrolysis Experiments

1.2.1 The Micro-Reactor

The experiments included in this thesis come in three main forms, Table 1.1 summarizes the experimental configurations. Fuels are diluted in a buffer gas, such as He, Ne, Ar or Kr, diluted to

less than 0.1% by pressure. Decomposition takes place when the gas mixture is passed through the micro-reactor, the relative size of which can be pictured in Figure 1.1. The micro-reactor is a tube composed of silicon carbide, and is about 2 to 3 cm long. This material can be resistively heated to temperatures of up to 1800 K; the heated portion (between electrodes) is roughly 1 to 1.5 cm long (red portion in Fig 1.1). The resistance of the tube can be adjusted for heating with SiC sand blasting (to raise the resistance) and with pencil lead (graphite, to lower the resistance).

At the Advanced Light Source (ALS) at Lawrence Berkeley's National Laboratory (LBNL), the gas mixture is continuously supplied to a 0.6 mm i.d. SiC tube by mass flow controllers held at 280 sccm (standard cubic centimeters min^{-1}) due to the nature of the ionization source. At the University of Colorado, experiments are conducted with a 1 mm i.d. SiC tube and pulsed flow at 10 Hz. Figure 1.2 shows the SiC tube inside the general pulsed valve assembly. The external wall temperature of the reactor is monitored using a Type C thermocouple, which is spot-welded to tantalum foil and attached to the tube exterior between electrodes with 0.005 inch tantalum wire. The accuracy of the thermocouple is 1% from 270 to 2300 K (Omega Engineering). Copper wire supplies current to two molybdenum electrodes, clamped to the exterior of the tube in two locations by carbon discs, see Fig. 1.2. Heater and thermocouple electrical feeds are pictured in Fig. 1.2 exiting a ceramic heat shield, which encloses the micro-reactor to minimize radiative heat losses. This SiC tube, heat shield, thermocouple, and heater assembly is placed on a copper heat sink and mounted to a Parker General Valve. Care must be taken to keep the valve operating under temperatures of 400 K. A type K thermocouple is attached to the exterior of the pulsed valve to monitor temperature, and a water cooling sleeve is placed in contact with the copper heat sink. A heater can also be placed on the valve to prevent condensation of materials with low vapor pressures.

Typical residence times of target molecules within the reactor are 25-150 microseconds. [61] At the reactor exit, the gas mixture supersonically expands (faster than the speed of sound) into a vacuum chamber held at about 1×10^{-6} Torr. This expansion rapidly cools the rotational and vibrational temperatures of the pyrolysis products, and effectively quenches chemistry by eliminating further molecular collisions. The following sections describe the primary diagnostics used to identify the products exiting the reactor, photoionization mass spectrometry (PIMS) and matrix isolation infrared (IR) spectroscopy.

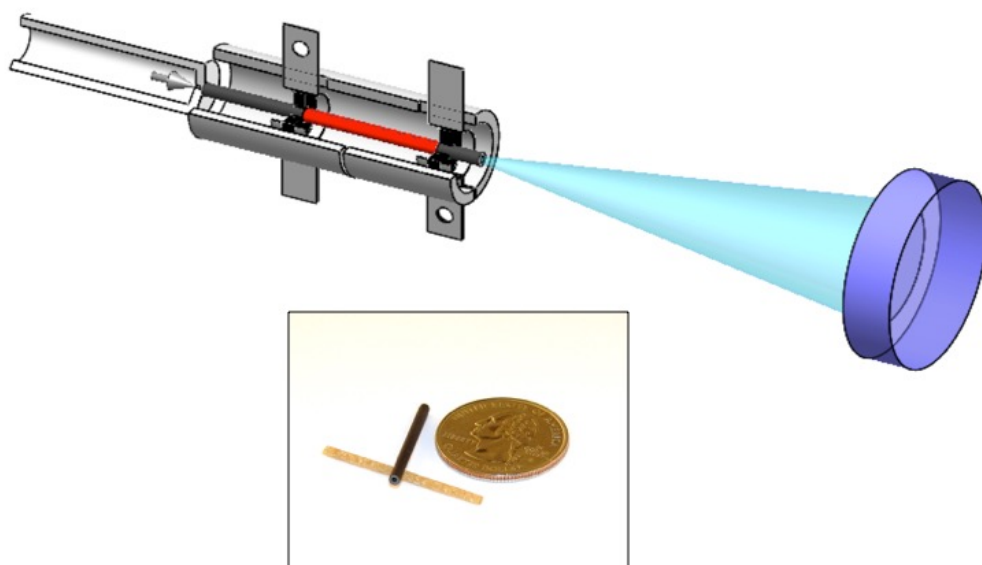


Figure 1.1: Top: Reactor setup with pulsed valve pictured upstream, and expansion onto cold window pictured downstream. The SiC tube is clamped by two molybdenum electrodes attached to the tube with carbon disks, the heated region is shown in red. Bottom: The SiC micro-reactor compared to a quarter and a piece of linguini.

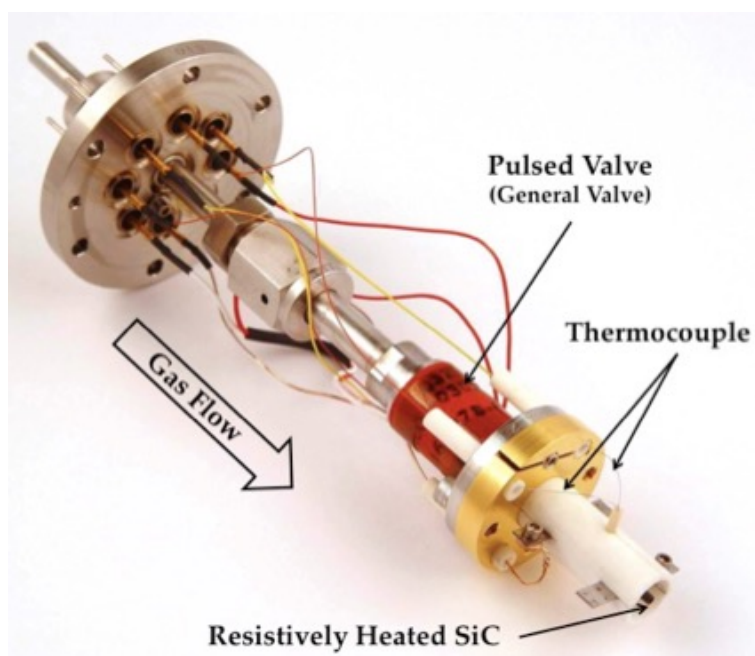


Figure 1.2: The silicon carbide micro-reactor enclosed in a ceramic heat shield and mounted to a pulsed valve assembly.

1.2.2 Photoionization Mass Spectrometry

Photoionization mass spectrometry experiments are carried out in two forms, one at the University of Colorado and the other at the Chemical Dynamics Beamline at Berkeley’s ALS (see Table 1.1). In both experiments, roughly 1 cm from the exit of the reactor, the molecular cloud of products is skimmed through a 2 mm aperture, creating a slivered molecular beam that flies straight towards the ionization region, see Figure 1.3. In Colorado, the ionization source is the 9th harmonic of a Nd:YAG laser, 118.2 nm or 10.487 eV, which fires in tandem with the pulsed valve assembly at 10 Hz. The Nd:YAG laser emits photons at 1064 nm. This light is directed through a doubling crystal which products 532 nm light, or the second harmonic of 1064 nm ($1/1064 \text{ nm} + 1/1064 \text{ nm} = 1/532 \text{ nm}$). The third harmonic is generated with a tripling crystal ($1/1064 \text{ nm} + 1/532 \text{ nm} = 1/355 \text{ nm}$) and the resulting 355 nm exits the laser head. This beam is directed and focused with a fused silica plano-convex lens into a tripling cell, which contains roughly 150 Torr of a 10:1 Ar/Xe mixture. As the beam passes through this gas mixture, the 9th harmonic (of the original 1064 nm Nd:YAG output) forms a beam of 118.2 nm light, equivalent to 10.487 eV photon energy, which is capable of ionizing most organic species. The 118.2 nm light is focused into the ionization region using a biconvex MgF₂ lens, but it is important to note that 355 nm light is still very present as the conversion efficiency to 118.2 nm is very low (less than 10%). There it encounters the skimmed molecular beam, and the resulting cations are extracted using dual-stage ion optics in a Jordan reflectron time-of-flight mass spectrometer [152]. Time of flight is translated into mass *via* simple calibration using mixtures of known masses. PIMS spectra are a composite of 1000 averaged scans, with a minimum mass resolution $m/\Delta m$ of 400. Experiments at the ALS employ

experiment	flow	^a reactor	light source	inlet P	^b outlet P
PIMS at LBNL ^c	Cont. (He)	0.6 x 15	VUV 500 MHz	100 - 300	2×10^{-4}
PIMS in CO	Pulsed (He)	1 x 15	118.2 nm, 10 Hz	1500	2×10^{-6}
FTIR in CO	Pulsed (Ar)	1 x 10	None	600 - 800	2×10^{-6}

Table 1.1: Summary of Biofuel Pyrolysis Experimental Conditions

^aHeated dimensions, inner diameter x length reported in mm.

^bPressures are reported in Torr.

^cAdvanced Light Source Beamline 9.0.2 at LBNL

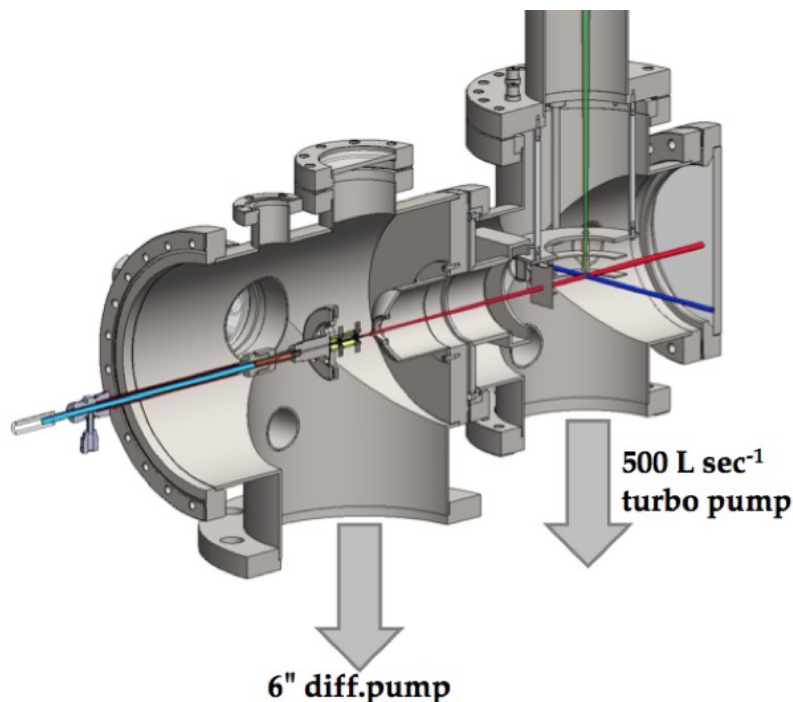


Figure 1.3: Photoionization mass spectrometry experimental configuration. The source chamber houses the SiC reactor, which supplies molecular beam (in red) to the ionization region (red, green, and blue intersection). The blue indicates the laser beam, which ionizes the organics. The resulting cations are accelerated up the drift tube (green) and collected by time of flight and mass to charge ratio.

a different ionization source, a 500 MHz tunable synchrotron. The quasi-continuous (500 MHz) radiation can be tuned between 7.4 to 19 eV, allowing for additional qualitative results such as the ability to characterize organic species by their ionization energy onsets. Gas flow to the reactor is held at a continuous volumetric flow rate of 260 sccm (standard $\text{cm}^3 \text{min}^{-1}$) using an MKS P4B (0 - 200 sccm N_2) mass flow controller. Continuous flow and the high repetition rate increase the PIMS signals by more than two orders of magnitude compared with the pulsed micro-reactor in Colorado. Typical photon fluxes are roughly 1×10^{13} photons per second [154]. The start time for the ion packet in the TOF spectrometer is provided by pulsing the repeller plate of the ion optics. Photoionization efficiency curves are normalized by dividing the ion count by the photocurrent at each photon energy.

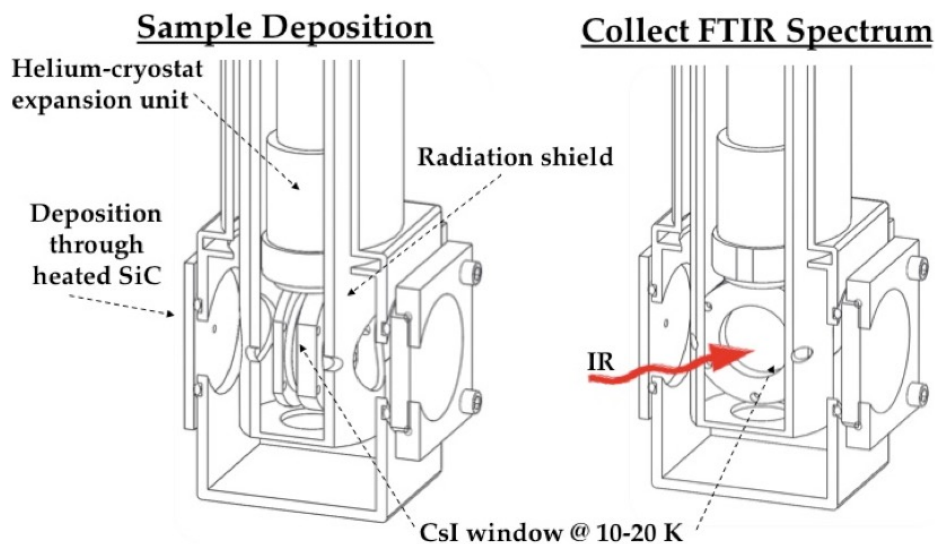


Figure 1.4: Matrix isolation infrared spectroscopy experimental setup.

1.2.3 Matrix Isolation Infrared Spectroscopy

To collect IR spectra of the initial reactive products of thermal decomposition, the technique of matrix isolation is used. Typical buffer gases in these experiments are Ar or Ne; lighter inert gases such as He cannot be frozen. Gas exiting the micro-reactor is directed toward a cold CsI window placed about 3 cm from the reactor exit, see Figure 1.4. The CsI window is held at 20 K by a dual-stage He cryostat (HC-2 APD Cryogenics). The diluted products of decomposition deposit in a lattice of frozen argon onto the CsI window. The window can then be placed in the path of an infrared absorption spectrometer for data collection. Deposition is typically 1 Torr/min, and data are typically collected on 100-300 Torr of sample. Deposition is kept at a low rate so as not to impart too much thermal energy on the window from products exiting the hot micro-reactor. Infrared absorption spectra are collected with a commercial FTIR (Nicolet 6700) fixed with an MCT-A detector ($4000 - 650 \text{ cm}^{-1}$). All IR spectra are averaged over 500 scans with 0.25 cm^{-1} resolution. Something to note in all of the experiments included in this thesis is that the operating conditions of each experimental setup described in Table 1.1 will be slightly different. Simulations [61] of the fluid dynamics in the heated microreactors reveal that they are nonlinear devices. The chemistry varies exponentially with the temperature (which is rising) and quadratically with pressure (which is falling). Recent experimental results confirm calculated temperatures inside the reactor [6]. In Chapter 5, I describe an experiment in which we attempt to measure the pressure within the reactor,

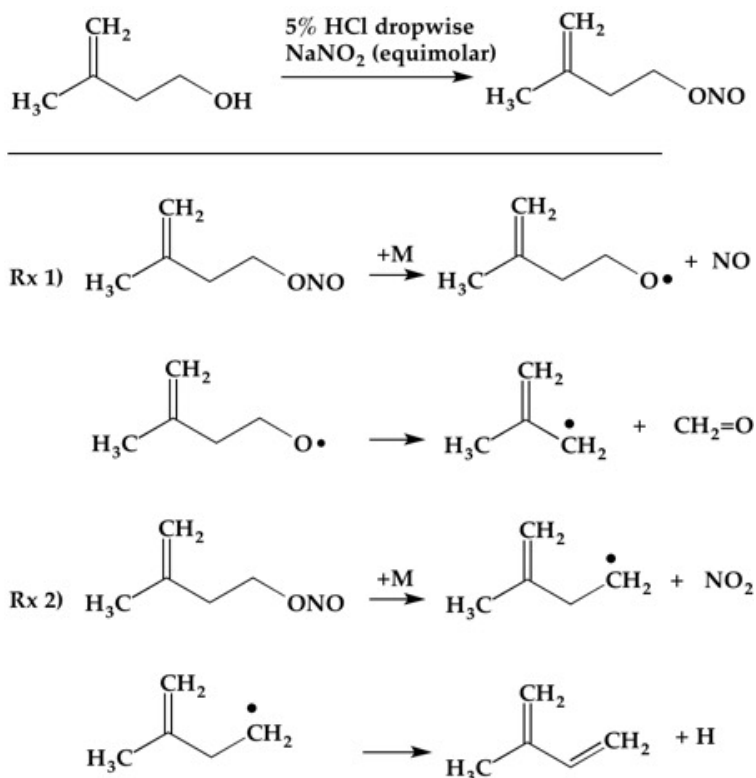
however the most recent results are solely qualitative. The location and volume of this 'sweet spot', or position of maximum temperature and pressure in the tube, will differ depending on which buffer gas is being used. Argon reaches notably lower temperatures than helium during the short residence times experienced in the reactor, and SiC wall temperatures must typically be 200 K higher for argon matrix experiments to see similar results to the helium run PIMS experiments. [61] The combination of PIMS and IR molecular diagnostics still proves to be a powerful tool in the detection of all of the pyrolysis products: atoms, organic radicals, and metastables.

1.3 Additional Projects

1.3.1 Methyl Allyl Radical Generation

As a graduate student, I worked on a number of projects that were not my own. My role in these projects will be described in the remainder of this chapter. In my fourth year of graduate school, I had the opportunity to work with Rob Tranter from Argonne National Labs (ANL) on the generation of methyl allyl radicals. Rob was interested in studying the rate of recombination and dissociation of 2-methyl allyl radicals, $(\text{CH}_2\text{C}(\text{CH}_3)\text{CH}_2)$. [147]. This species is an example of a resonantly stabilized radical, and it is therefore expected to live a lengthy lifetime in its natural environment in a combustion engine. A diaphragmless shock tube was used to study $\text{CH}_2\text{C}(\text{CH}_3)\text{CH}_2$ decomposition at temperatures of 700 - 1350 K (ignition temperatures) and pressures of 60 - 260 Torr. A laser schlieren densitometry profile was measured to track the reaction inside the shock tube. Rate coefficients for the dissociation of two distinct $\text{CH}_2\text{C}(\text{CH}_3)\text{CH}_2$ precursors, recombination of $\text{CH}_2\text{C}(\text{CH}_3)\text{CH}_2$, and dissociation of $\text{CH}_2\text{C}(\text{CH}_3)\text{CH}_2$ were obtained using high level *a priori* calculations. My contribution to this work was designing a compound that would readily decompose to $\text{CH}_2\text{C}(\text{CH}_3)\text{CH}_2$ at low temperatures, and refining the synthesis of it.

Nitrites have commonly been used to create weak bonds that easily decompose into desired reactive species. To create the $\text{CH}_2\text{C}(\text{CH}_3)\text{CH}_2$ radical, the synthesis of 3-methylbut-3-enyl nitrite and decomposition pathways are shown in Scheme 1.1. The synthesis was adapted from the synthesis of methyl nitrite, a gaseous species [84], and work I had done on the synthesis of 2-phenoxyethyl nitrite. A mixture of 3-methyl-3-butene-1-ol (37 mmol) and excess NaNO_2 (74 mmol) was held in an ice bath and stirred vigorously. 20 mL of 9.25% HCl was added dropwise to the mixture slowly, over



Scheme 1.1: Synthesis of 3-methylbut-3-enyl nitrite, and 2 possible decomposition pathways.

the course of 5 minutes. During addition of the acid, the solution refluxed gently, and after a few minutes, brown gas formed in the headspace above the solution (NO_2). After the addition of HCl, the solution continued to mix for 15 additional minutes and then allowed to settle into an organic and aqueous layer. The blue-colored organic layer was collected and washed twice with saturated NaCl solution and then dried over Na_2SO_4 . Successful synthesis and product identification was completed by Dr. John Randazzo *via* IR and H-NMR to confirm the presence of 3-methylbut-3-enyl nitrite.

It was concluded that both precursors used in the experiment gave the same results for rate coefficient determination in the shock tube. The decomposition of 3-methylbut-3-enyl nitrite had the potential to go 2 different ways, see Scheme 1.1. Reaction 1 would begin with elimination of NO by cleavage of the weak O-NO bond. The resulting $\text{CH}_2=\text{C}(\text{CH}_3)\text{CH}_2\text{CH}_2\text{O}\cdot$ radical then readily eliminates formaldehyde ($\text{CH}_2=\text{O}$) leaving behind the desired product, 2-methyl allyl radical. Alternatively, the C-ONO bond is also weak and could cleave to eliminate NO_2 , see Reaction 2. This radical will likely eliminate a hydrogen atom to produce 2-methyl-1,3-butadiene

($\text{CH}_2=\text{CHC}(\text{CH}_3)\text{CH}_2$). Given that similar results were obtained using an alternative precursor, 2,5-dimethyl-1,5-hexadiene, Reaction 1 and therefore production of $\text{CH}_2\text{C}(\text{CH}_3)\text{CH}_2$ is believed to dominate in the decomposition of 3-methylbut-3-enyl nitrite [147].

1.3.2 Synchrotron Studies

I had the opportunity to study with Rob Tranter and X-ray beamline director Alan Kastengren at Argonne's Advanced Photon Source (APS). The efforts of this study were focused on determining a pressure within the tiny micro-reactor. [148] Standard pressure measurement techniques are impossible, and insertion of anything into the tube (1 mm I.D.) will disrupt gas flow and change the gas phase dynamics dramatically. Reaction rates can be described by the well known Arrhenius expression ($\text{rate} = A e^{(-E_a/k_B T)}$), which demonstrates that speed of reactions depend upon the quadratic of the pressure (the 'A' factor) and the square of the temperature. Consequently, changing these variables even slightly will have drastic effects on product distribution. The results I present about decomposition pathways of molecular species are even more useful when a temperature and pressure can be reported. I helped build an experiment that utilized X-ray synchrotron radiation to penetrate the walls of the SiC tube and ionize a tracer gas, krypton, which was diluted in a helium buffer gas. Resulting Kr^+ ions are very unstable, and can release energy in the form of fluorescent photons that exit through the reactor walls to be collected by a detector. Using a known amount of Kr in He, and normalizing the Kr based on fluorescent signal, in principle a known amount of Kr atoms can be traced back to the inside of the tube. This experiment was the first *in situ* measurement of fluid dynamics in an opaque body, and is discussed in great detail in Chapter 5.

I also had a few opportunities to travel out to the Advanced Light Source (ALS) at Lawrence Berkeley National Laboratory (LBNL). Here I was able to conduct PIMS experiments with a tunable vacuum ultra-violet (VUV) synchrotron light source. This replaced the lab ionization source of fixed 10.487 eV at a repetition rate of 10 Hz with energy tunability and a very rapid repetition rate (500 MHz). In addition to identifying thermal decomposition products by mass, with tunable radiation it is possible to scan and identify a mass species based on its characteristic ionization energy (energy of electron loss) for further validation. Projects conducted at LBNL are carried out in groups of two or three. While there I contributed to Grant Buckingham's studies over the thermal decomposition of benzyl and tropyli radicals, both of which are very important species in combustion. [21, 22]

The remaining chapters of this thesis describe projects in which I played a primary role, however many of these projects were drastically enhanced with the help of collaborators. In Chapter 2, pyrolysis studies of cyclohexanone were supported with coupled cluster electronic structure calculations that provided the heats of formation and energetics of different reaction pathways [118]. These calculations were provided by Thanh Nguyen (University of Texas), Josh Baraban (University of Colorado), and John Stanton (University of Texas). In Chapter 3, Josh Baraban and Michael McCarthy (Harvard-Smithsonian Center for Astrophysics) calculated the heat of formation (necessary to describe reaction energetics) and ionization energy (to support experimental findings) of glycolaldehyde [117]. Another major contributor to this project was Kathleen Morgan (Xavier University), who measured the heat of formation of glycolaldehyde experimentally. Both of these projects were completed with data from the ALS at Berkeley. Running experiments at Beamline 9.0.2 was made possible with the help and support of Musahid Ahmed, Tyler P. Troy, and Oleg Kostko, each from the University of California at Berkeley.

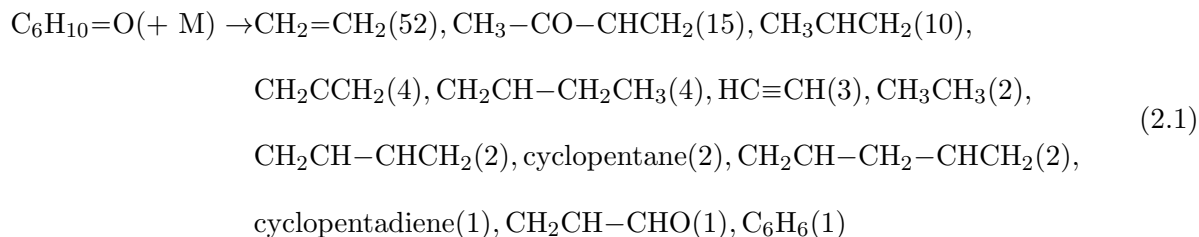
Chapter 2

Cyclohexanone

2.1 Introduction

Cyclohexanone, $C_6H_{10}=O$, is one of the many compounds under consideration as a second-generation biofuel. [18] We have studied the thermal degradation of cyclohexanone, paying attention to the first 150 μ seconds of chemistry in the absence of oxygen, and have identified multiple pyrolysis pathways. So far, it has been shown that a diesel engine produces less soot when blends of cyclohexanone with synthetic Fischer-Tropsch fuels are used. [73] Additionally, the sooting and chemiluminescence behaviors of bioderived fuels were studied in an optically accessible diesel engine, from which it was determined that cyclic additives such as cyclohexanone are more efficient in soot abatement than other oxygenated fuels. [18] The mechanisms by which cyclohexanone contributed to such results are poorly understood.

There have only been two experimental [38, 133] and one modeling [175] study on the pyrolysis or oxidation of cyclohexanone. The first study, back in 1970, [38] pyrolyzed cyclohexanone at 1300 K in ceramic tubes at pressures of 60 mTorr. The equation below shows the mole percent yield for each of the products detected from the pyrolysis of cyclohexanone.



Ethylene, methyl vinyl ketone (MVK), and propene are the three most abundant species under these conditions.

A jet-stirred reactor study has been reported on the kinetics of oxidation of cyclohexanone [133]. Samples of cyclohexanone (1000 -1500 ppm) in oxygen/nitrogen gas mixtures at 10 atm were heated to temperatures of 530 -1220 K. After a fixed residence time of 0.7 s, the resulting products were sampled and identified by both infrared (IR) and gas chromatographic analysis. Unlike the previous pyrolysis experiments, [38] MVK was never found to be an important product in these oxidation experiments, even under the richest fuel conditions.

2.2 Plausible Decomposition Pathways

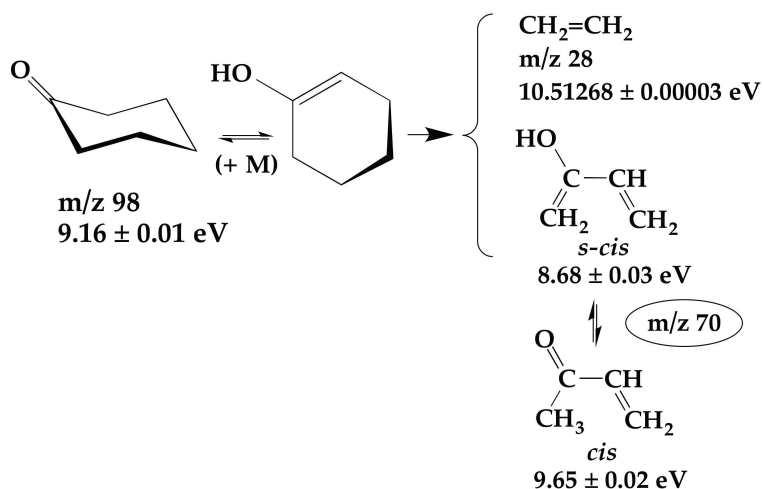
Two potential decomposition pathways for cyclohexanone are shown in Scheme 2.1, and thermodynamic quantities pertinent to the decomposition of cyclohexanone are summarized in Table 2.1. Enols such as C_6H_9OH and $CH_2=C(OH)-CH=CH_2$ in the retro Diels-Alder reaction are typically about 10 kcal mol^{-1} less stable than their corresponding ketones, cyclohexanone and MVK. Common conjectures [36, 136, 172, 175, 176] for the barriers of the gas-phase keto/enol tautomerizations ($>CH-CO- \rightarrow >CH=C(OH)$) are about 65 kcal mol^{-1} .

One could anticipate [38] that the pyrolysis of cyclohexanone might begin with the isomerization to the enol, C_6H_9OH , followed by a retro-Diels-Alder fragmentation. Alternatively, simple cleavage of C-C bonds within $C_6H_{10}=O$ could result in the formation of three different sets of diradicals. The initial diradical products will be unstable; the fate of these radical species is explored in Scheme 2.2.

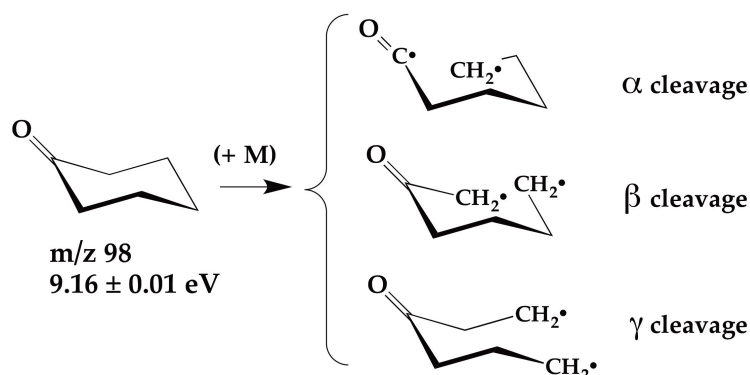
To estimate the thermochemistry for the cracking of C_6H_9-OH , consider a similar alkene, cyclohexene. Cyclohexene has been observed [72] to fragment via retro Diels-Alder reaction: the $\Delta_{rxn}H_{298}$ (cyclohexene $\rightarrow CH_2=CH_2 + CH_2=CH-CH=CH_2$) is $40.0 \pm 0.3 \text{ kcal mol}^{-1}$ and the activation energy E_a is 62 kcal mol^{-1} (see entry 11 in Table 2.1). Consequently the threshold for cyclohexanone pyrolysis to ethylene and $CH_2=C(OH)-CH=CH_2$ is estimated to be roughly 75 kcal mol^{-1} , a relatively low energy barrier. It's also expected that the resulting $CH_2=C(OH)-CH=CH_2$ will subsequently isomerize to methyl vinyl ketone (MVK), $CH_3CO-CH=CH_2$.

The energy to fragment C-C bonds within the ring, see the bottom of Scheme 2.1 are difficult to assess due to the highly unstable nature of the resulting diradicals. Based on known energetics

Isomerization: retro-Diels-Alder Fragmentation



Cyclohexanone Fragmentation to Radicals



Scheme 2.1: Two possible pathways for the thermal decomposition of cyclohexanone.

of model compounds listed in Table 2.1, CH_3CHO , CH_3COCH_3 , $\text{CH}_3\text{COCH}_2\text{CH}_3$, we can estimate the bond energetics of three distinct C-C sites within cyclohexanone. The bond energies of the α C-H bonds of cyclohexanone are expected to be about 94 kcal mol^{-1} (entry 1 in Table 2.1), while the three C-C bonds of the ring (α, β, γ) are likely to be lower in energy, around 84 kcal mol^{-1} (entries 2 - 6 in Table 2.1). Applying these estimates to the pathways in Scheme 2.1, we anticipate cyclohexanone will initially isomerize and decompose to $\text{CH}_2=\text{CH}_2$ and $\text{CH}_2=\text{C}(\text{OH})\text{CH}=\text{CH}_2$. At slightly higher reactor temperatures, fragmentation of the cyclohexanone ring to diradicals should ensue.

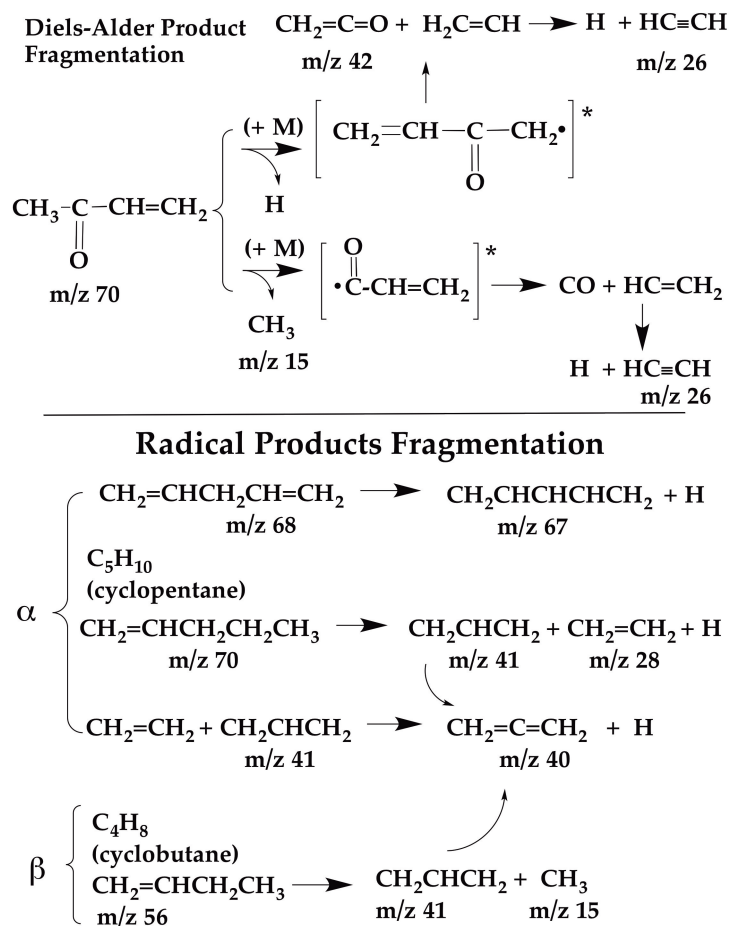
The likely fates of the radicals at the bottom of Scheme 2.1 are explored in Scheme 2.2. Fragmentation of the cyclohexanone α C-C bond produces the unstable diradical, $[\cdot\text{CH}_2\text{CH}_2\text{CH}_2\text{CH}_2\text{CH}_2\text{CO}\cdot]$.

reaction	kcal mol ⁻¹	refs.
1 DH ₂₉₈ (CH ₃ COCH ₂ -H)	96 ± 2	7, 124
2 DH ₂₉₈ (CH ₃ CO-CH ₃)	84.5 ± 0.5	14, 114
3 DH ₂₉₈ (CH ₃ COCH ₂ -CH ₃)	84 ± 2	14, 114
4 DH ₂₉₈ (CH ₃ CO-CH ₂ CH ₃)	83.6 ± 0.6	14, 114
5 DH ₂₉₈ (CH ₃ -CH ₂ CH ₃)	89.1 ± 0.4	14, 114
6 DH ₂₉₈ (CH ₃ CH ₂ -CH ₂ CH ₃)	88.0 ± 0.6	14, 114
7 DH ₂₉₈ (CH ₂ CH-CH ₂ CH ₃)	100.0 ± 0.8	14, 114
8 DH ₂₉₈ (CH ₂ CHCH ₂ -CH ₃)	76.4 ± 0.5	14, 114
9 DH ₂₉₈ (CH ₂ CHCH ₂ -CHCH ₂)	87.3 ± 0.8	14, 114
10 Δ _{rxn} H ₂₉₈ (CH ₂ CHCH ₂ → H + CH ₂ =C=CH ₂)	56.2 ± 0.5	14, 114
11 Δ _{rxn} H ₂₉₈ (cyclohexene → CH ₂ =CH-CH=CH ₂ + CH ₂ =CH ₂)	40.0 ± 0.3	114
12 Δ _{rxn} H ₂₉₈ (<i>s-cis</i> -CH ₂ =C(OH)-CH=CH ₂ → <i>s-cis</i> -CH ₃ -CO-CH=CH ₂)	-12 ± 1	this work
13 Δ _{rxn} H ₂₉₈ (cyclohexanone → CH ₂ =C(OH)-CH=CH ₂ + CH ₂ =CH ₂)	53 ± 1	this work, 114
14 Δ _{rxn} H ₂₉₈ (cyclohexanone → CH ₃ COCH=CH ₂ + CH ₂ =CH ₂)	41 ± 1	this work, 114
15 Δ _{rxn} H ₂₉₈ (<i>cis</i> -CH ₃ COCH=CH ₂ → CH ₃ CO + CH=CH ₂)	95 ± 1	this work, 14

Table 2.1: Thermochemistry of Cyclohexanone and Related Species

This species can either decompose to CH₂=C=O and the [\cdot CH₂CH₂CH₂CH₂·] diradical, or shed carbon monoxide to produce the pentamethylene diradical, [\cdot CH₂CH₂CH₂CH₂CH₂·]. The pentamethylene diradical can proceed to react in several ways. It can lose two H atoms via β -scission to produce CH₂=CHCH₂CH=CH₂ or ring close to produce cyclopentane. Pentamethylene could also internally disproportionate to CH₂=CHCH₂CH₂CH₃ or extrude ethylene to form the trimethylene diradical [\cdot CH₂CH₂CH₂·]. At the high temperatures of the micro-reactor, trimethylene diradical is expected to lose an H atom to produce the allyl radical, CH₂CHCH₂. Cleavage of either the α or β C-C bonds followed by the loss of CH₂=C=O in Scheme 2.2 leads of the formation of the tetramethylene diradical, [\cdot CH₂CH₂CH₂CH₂·]. By analogy to the pentamethylene diradical, the tetramethylene diradical could decompose in four ways. The tetramethylene diradical could

α and β -fragmentation are not stable and are also not expected to survive in the hot micro-reactor. Decomposition of 1,4-pentadiene could produce $\text{CH}_2=\text{CH}-\text{CH}=\text{CH}_2$ or CH_2CHCH_2 and vinyl radical. Cyclopentane and 1-pentene are expected to fragment to the allyl (CH_2CHCH_2) and ethyl (CH_2CH_3) radicals and ultimately to ethylene. Similarly, cyclobutane and 1-butene could crack apart to allyl and methyl radicals. At higher temperatures, the allyl radical is likely to further decompose by loss of an H atom to form allene, $\text{CH}_2=\text{C}=\text{CH}_2$.



Scheme 2.3: Further decomposition of primary products from cyclohexanone pyrolysis.

2.4 Results

2.4.1 Theoretical Thermochemistry

The heats of formation of many of the species in Schemes 2.1 - 2.3 are available in Table 2.1. Surprisingly, the heat of formation of $\text{CH}_3\text{CO}-\text{CH}=\text{CH}_2$ has not been measured; this is a very important compound in atmospheric chemistry and combustion processes. The heats of formation of MVK and its enol isomer have been calculated by Thanh Nguyen, Josh Baraban, and John Stanton using a medium accuracy extrapolated *ab initio* thermochemistry protocol, which is a modification of the HEAT method [17, 63, 143]. The modified HEAT procedure is intended for medium-sized molecular systems, and achieves a thermochemical accuracy of about $0.5 \text{ kcal mol}^{-1}$ (see Table 2.6 in the Supplemental Information of this chapter) [106]. Further tests for a set of molecules used in the HEAT protocol are in progress in order to validate the performance of this procedure, and will be reported in due course. In this work, heats of formation of MVK and its enol are computed using isodesmic reactions that are expected to give better results than those derived simply from total atomization energies, owing to cancellation of systematic errors. Heats of formation at 0 K (Table 2.2) are found to be: $\Delta_f H_0(\text{cis-CH}_3\text{COCH}=\text{CH}_2) = 22.5 \pm 0.5 \text{ kcal mol}^{-1}$ and $\Delta_f H_0(\text{s-cis-1-CH}_2=\text{C}(\text{OH})\text{CH}=\text{CH}_2) = -9.8 \pm 0.5 \text{ kcal mol}^{-1}$. Note that four distinct enol conformers were characterized, see Scheme 2.1 for structure. With the thermochemical values at 0 K in hand, heats of formation at the standard conditions (298 K and 1 atm) are then computed using [92] Equation 2.2:

$$\Delta_f H_{298}(M) = \Delta_f H_0(M) + (H_{298} - H_0)(M) - \sum N A_i (H_{298} - H_0) A_i \quad (2.2)$$

Here M denotes either MVK or enol, A_i represents an H, C, or O atom, and NA_i is the number of A_i atoms in the molecule. $H_{298} - H_0$ is the thermal correction to the enthalpy, computed using the partition functions for vibrations, rotations, and translations in the anharmonic oscillator (in the VPT2 approximation [95]) and rigid-rotor approximation. [105] The heats of formation at 0 K and 298 K are $\Delta_f H_0(M)$ and $\Delta_f H_{298}(M)$. Table 2.3 shows the heat of formation obtained at 298 K to be $-26.1 \pm 0.5 \text{ kcal mol}^{-1}$ for cis-MVK and $-13.7 \pm 0.5 \text{ kcal mol}^{-1}$ for its enol form, *s-cis-1-CH*₂=C(OH)CH=CH₂. In addition, the effects of two hindered internal rotations (HIR) in

cis-MVK are also investigated. HIR affect zero-point vibrational energies and thermal corrections, and therefore can influence thermochemistry. The effects of two HIRs in cis-MVK are moderate; they shift heats of formation by less than 0.1 kcal mol⁻¹ (see Table 2.3). It should be mentioned that when the hindered internal rotors are involved, heats of formation of MVK include contributions of both cis- and trans-conformers of MVK because the potential surface for hindered internal rotors contains both conformers.

working reactions	$\Delta_{rx}H_0$	Δ_fH_0
<i>trans</i> -MVK + H ₂ → CH ₃ CHO + C ₂ H ₄	-0.13	-22.29
<i>trans</i> -MVK + CH ₄ → CH ₃ CHO + C ₃ H ₆	4.68	-21.82
<i>trans</i> -MVK + CH ₄ → CH ₃ C(O)CH ₃ + C ₂ H ₄	9.52	-22.18
<i>trans</i> -MVK + C ₂ H ₆ → CH ₃ C(O)CH ₃ + C ₃ H ₆	-0.96	-21.96
<i>s-trans</i> -1-enol + CH ₄ → CH ₂ =CH(OH) + C ₃ H ₆	9.76	-12.26
<i>s-trans</i> -1-enol + CH ₄ → CH ₃ OH + CH ₂ =CH-CH=CH ₂	13.15	-12.37
average Δ_fH of <i>trans</i> -MVK, <i>trans</i> -CH ₃ -CO-CH=CH ₂		-22.30 ± 0.24
average Δ_fH of <i>cis</i> -MVK, <i>cis</i> -CH ₃ -CO-CH=CH ₂		-22.43 ± 0.24
average Δ_fH of <i>s-trans</i> -1-enol, <i>trans</i> -CH ₂ =C(OH)-CH=CH ₂		-12.32 ± 0.24

Table 2.2: Calculated Heat of Formation (kcal mol⁻¹) of Methyl Vinyl Ketone and the *s-trans*-1-Enol from Isodesmic Reactions

species	Δ_fH_0	$H_{298} - H_0$	Δ_fH_{298}
<i>cis</i> -MVK	-22.4 ± 0.5	4.363	-26.2 ± 0.5
	-22.5 ± 0.5	4.553	-26.1 ± 0.5
<i>trans</i> -MVK	-22.3 ± 0.5	4.382	-25.8 ± 0.5
<i>s-trans</i> -1-enol	-9.8 ± 0.5	4.135	-16.3 ± 0.5
<i>s-cis</i> -1-enol	-9.8 ± 0.5	4.145	-13.7 ± 0.5
H	51.633	1.01	52.103
C	170.025	0.25	171.336
O	58.997	1.037	59.567

Table 2.3: Calculated Thermal Correction Energies (kcal mol⁻¹) and Heats of Formation (kcal mol⁻¹) of MVK at 298 K. In the case of *cis*-MVK, two hindered internal rotors are assumed to be separable from the remaining vibrations, and each one is treated as a separated ID-hindered internal rotor.

2.4.2 Photoionization

Three experiments have been conducted on the pyrolysis of cyclohexanone: photoionization mass spectrometry (PIMS) at 10.487 eV in a pulsed reactor, PIMS with tunable VUV light in a continuous flow reactor, and matrix isolation infrared spectroscopy using a pulsed reactor. All three methods are described in Chapter 1 of this thesis. For the PIMS experiments both at CU and LBNL, mixtures were 0.008 to 0.06% cyclohexanone in helium. A list of characteristic ionization energies for relevant compounds to this study can be found on Table 2.4. Photoionization mass spectroscopy is a convenient method to track the decomposition channels presented in Schemes 2.1 - 2.3. However, use of a fixed frequency VUV light source in PIMS (10.487 eV, 10Hz light at the University of Colorado) can lead to problems with ion fragmentation.

The ionization energy (IE) of cyclohexanone [30, 83] is 9.2 eV (see Table 2.4), and preliminary PIMS spectra taken in Colorado employ a 118.2 nm laser (10.487 eV); see Fig. 2.1. Ionization is 1.3 eV above the threshold for cyclohexanone and consequently, the [cyclohexanone]⁺ radical-cation is chemically activated and may fragment, a term labeled dissociative ionization.

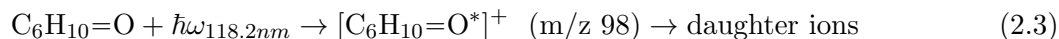


Figure 2.1 shows a normal mass spectrum at 300 K with only the parent species (m/z 98) present. No dissociative ionization is evident. Pyrolysis of cyclohexanone in the pulsed reactor starts at 1000 K as shown by the presence of MVK, m/z 70, and $\text{CH}_2=\text{C}=\text{O}$, m/z 42. Other prominent peaks are m/z 55, m/z 69, and m/z 80. We believe that these and other ions result from fragmentation of a mixture of the cyclohexanone radical cation, $[\text{C}_6\text{H}_{10}=\text{O}]^+$ and the enol cation, $[\text{C}_6\text{H}_9\text{OH}]^+$. A more detailed discussion of dissociative ionization is deferred until the end of the paper following the detection of the neutral enols, $\text{C}_6\text{H}_9\text{OH}$ and $\text{CH}_2=\text{C}(\text{OH})\text{CH}=\text{CH}_2$. Dissociative ionization can be avoided using tunable synchrotron radiation, and in these studies this is provided by Lawrence Berkeley National Lab's (LBNL) Beamline 9.0.2.

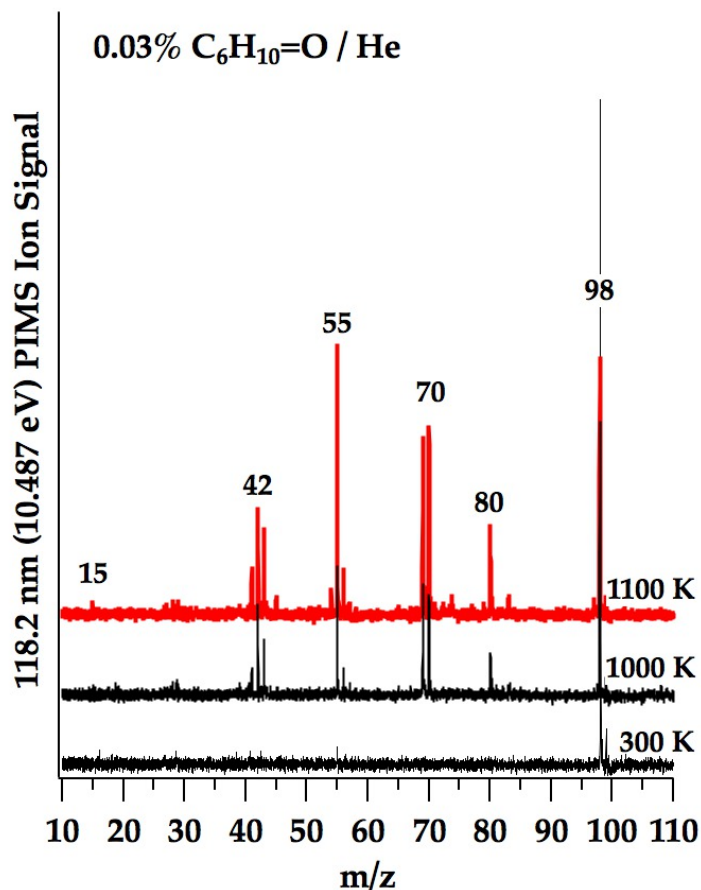


Figure 2.1: Photoionization mass spectrum from pulsed 118.2 nm PIMS. Mixture is 0.03% cyclohexanone in He heated up to 1100 K in a pulsed micro-reactor.

2.4.3 Product Identification with Tunable VUV Radiation

With synchrotron VUV radiation, photoionization mass spectrometry was used to observe the decomposition of dilute samples of cyclohexanone in He (0.03%) at 1200 K. To confirm the retro-Diels-Alder mechanism (Scheme 2.1), the characteristic enols of decomposition must be identified. Figure 2.2 is a PIMS spectrum taken under continuous flow conditions at the ALS; the radiation is tuned to 9.0 eV. The enol of MVK, $\text{CH}_2=\text{C}(\text{OH})-\text{CH}=\text{CH}_2$ (m/z 70), has a measured ionization energy of 8.7 eV (Table 2.4). Similarly, Table 2.4 shows the $\text{IE}(\text{CH}_2=\text{CHOH})$ to be 1 eV below the $\text{IE}(\text{CH}_3\text{CHO})$. One might therefore expect that the enol of cyclohexanone ($\text{C}_6\text{H}_9\text{OH}$, m/z 98) would ionize roughly 1 eV lower than the parent ketone, or around 8.2 eV (Table 2.4). Photoionization efficiency curves (PIE) of the ionization thresholds further confirm the identity of both enols at m/z 98 and m/z 70 by providing characteristic appearance energies. The top insets in Fig. 2.2 show

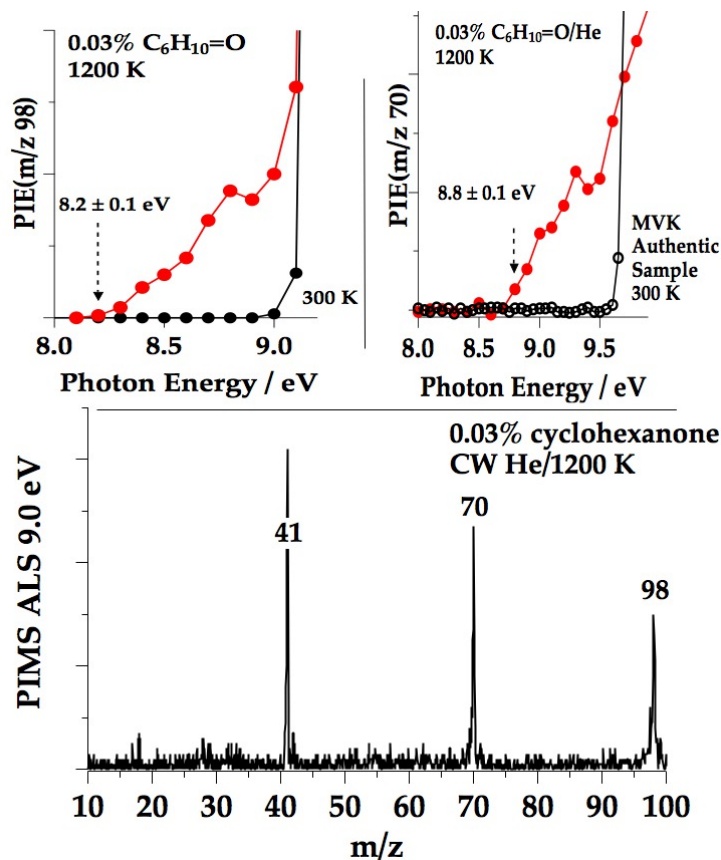


Figure 2.2: Products Arising from the Radical/Radical Disproportionation of the Three Sets of Radical Pairs Produced by Fragmentation of the Cyclohexanone Ring

the PIE of m/z 98 and the appearance energy of 8.2 ± 0.1 eV is observed in the expected region. The PIE of m/z 70 at the top of Fig. 2.2 displays an appearance energy of 8.8 ± 0.1 eV that is characteristic of $\text{CH}_2=\text{C}(\text{OH})\text{CH}=\text{CH}_2$ (see Table 2.1). The two features in Fig. 2.2 at m/z 98 and m/z 70 cannot be the ions $\text{C}_6\text{H}_{10}=\text{O}^+$ nor $\text{CH}_3\text{COCH}=\text{CH}_2^+$ because 9.0 eV is significantly below their ionization thresholds. The m/z 98 and m/z 70 features are therefore assigned to the enols, $\text{C}_6\text{H}_9\text{OH}^+$ and $\text{CH}_2=\text{C}(\text{OH})-\text{CH}=\text{CH}_2^+$. The other product of the retro-Diels-Alder reaction is ethylene. At 1200 K, a PIE of m/z 28 finds an appearance energy that is characteristic of $\text{CH}_2=\text{CH}_2$ at 10.5 eV (see Supplemental Figure 2.12). All of the retro-Diels-Alder products in Scheme 2.1 have been identified when cyclohexanone is heated to 1200 K.

Evidence for the ring cleavage channels begins with an intense feature in Figure 2.2 at m/z 41, a signature of the allyl radical, CH_2CHCH_2 . Allyl radicals originate from the (α and β) channels described in Schemes 2.2 and 2.3. Figure 2.3 is a PIMS of cyclohexanone at 1200 K with the

m/z	species	name	IE / eV	refs.
1	H	H atom	13.59844 ± 0.00001	98
15	CH ₃	methyl radical	9.8380 ± 0.0004	15
26	HC≡CH	acetylene	11.40081 ± 0.00001	119
28	CO	carbon monoxide	14.0136 ± 0.0005	44
28	CH ₂ =CH ₂	ethylene	10.51268 ± 0.00003	166
39	HCCCH ₂	propargyl radical	8.6982 ± 0.0005	54
40	CH ₂ =C=CH ₂	allene	9.688 ± 0.002	173
40	CH ₃ C≡CH	methyl acetylene	10.3674 ± 0.0001	168
41	CH ₂ CHCH ₂	allyl radical	8.13146 ± 0.00025	170
42	CH ₂ =C=O	ketene	9.6191 ± 0.0004	107
42	CH ₂ =CH-CH ₃	propene	9.7435 ± 0.0005	24
43	CH ₃ CO	acetyl radical	6.95 ± 0.02	174
44	CH ₃ CHO	acetaldehyde	10.2295 ± 0.0007	74
44	CH ₂ =CH-OH	ethenol	9.33 ± 0.05	142
54	CH ₂ =CH-CH=CH ₂	1,3-butadiene	9.082 ± 0.004	85
56	(CH ₂) ₄	cyclobutane	9.6 ± 0.1	12
56	CH ₂ =CHCH ₂ CH ₃	1-butene	9.63 ± 0.02	12
56	<i>trans</i> -CH ₃ CH=CHCH ₃	<i>trans</i> -2-butene	9.1259 ± 0.0005	24
68	CH ₂ =CHCH=CHCH ₃	1,3-pentadiene	8.61 ± 0.02	12
68	CH ₂ =CHCH ₂ CH=CH ₂	1,4-pentadiene	9.62 ± 0.02	12
70	CH ₃ CO-CH=CH ₂	methyl vinyl ketone	9.65 ± 0.05	88
70	CH ₂ =C(OH)CH=CH ₂	2-hydroxybutadiene	8.68 ± 0.03	151
70	CH ₂ =CHCH ₂ CH ₂ CH ₃	1-pentene	9.52 ± 0.02	12
70	C ₅ H ₁₀	cyclopentane	10.3 ± 0.1	12
98	C ₆ H ₁₀ =O	cyclohexanone	9.16 ± 0.01	30
98	C ₆ H ₉ -OH	cyclohexen-ol	8.2 ± 0.1	this work

Table 2.4: Ionization Energies of Important Organics

synchrotron tuned to 9.7 eV. A new feature at m/z 42 is now apparent and is assigned to be ketene, CH₂=C=O. Fig. 2.4 shows the result of 10.1 eV PIMS of cyclohexanone heated to 1200 K. Several new features appear at m/z 15, 40, 43, 54, 55, and 56. The inset at the top of Fig. 2.4 shows the PIE scans for m/z 41 (CH₂CHCH₂) and m/z 42 (CH₂=C=O); the thresholds for both

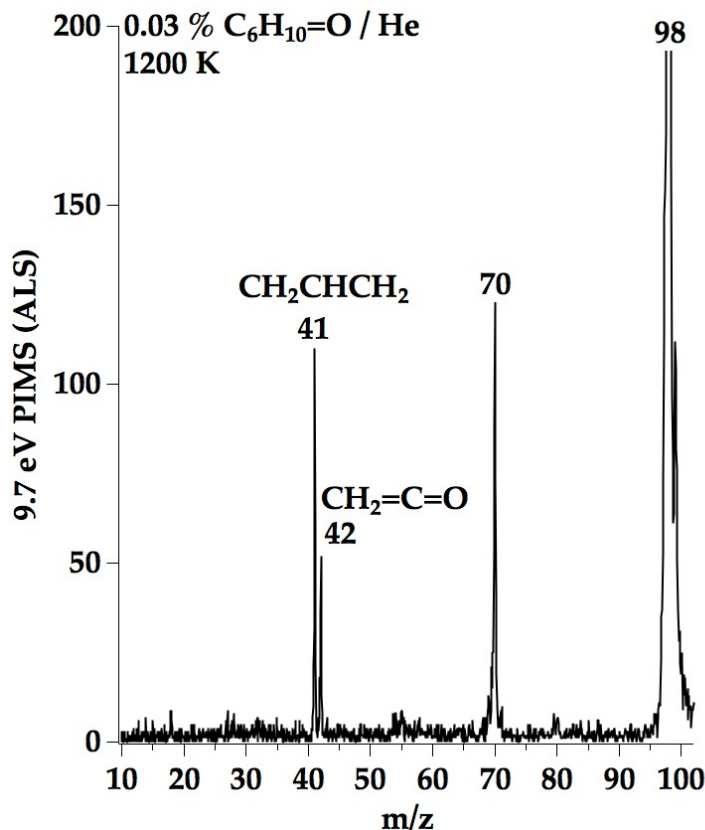


Figure 2.3: Photoionization mass spectrum at 9.7 eV of cyclohexanone at 1200 K in a continuous flow micro-reactor.

of these ions demonstrate the presence of allyl radical and ketene as products (see Table 2.4). (The presence of both allyl radical and ketene are further confirmed by IR spectra, *vide infra*). The ion at m/z 15 arises from the CH_3 radical. While methyl is not present in Schemes 2.1 and 2.2, it is a predicted product of the pyrolysis of MVK; see Scheme 2.3. This scheme predicts thermal cracking of $\text{CH}_3\text{CO}-\text{CH}=\text{CH}_2$ to $\text{CH}_2=\text{C}=\text{O}$ and $\text{HC}\equiv\text{CH}$ in addition to methyl radical.

Since PIMS confirms the formation of $\text{CH}_2=\text{C}(\text{OH})-\text{CH}=\text{CH}_2$ from cyclohexanone heated to 1200 K, the fate of both MVK and its enol must be discussed. Fig. 2.5 is a 10.0 eV PIMS scan of the products arising from an authentic sample of $\text{CH}_3\text{COCH}=\text{CH}_2$. The $\text{IE}(\text{MVK})$ is 9.65 ± 0.05 eV (see Table 2.4); at 300 K, there is no dissociative ionization and only ions at m/z 70 are detected. Heating MVK to 1200 K produces faint signals at m/z 15, 18, and 55. As the temperature increases to 1500 K, ions at 15, 27, 42, and 55 are clearly present. Fig. 2.6 shows scans of the $\text{PIE}(m/z$ 70) resulting from heating MVK to 1100 K and 1200 K. The threshold for $\text{PIE}(m/z$ 70) at 1200 K

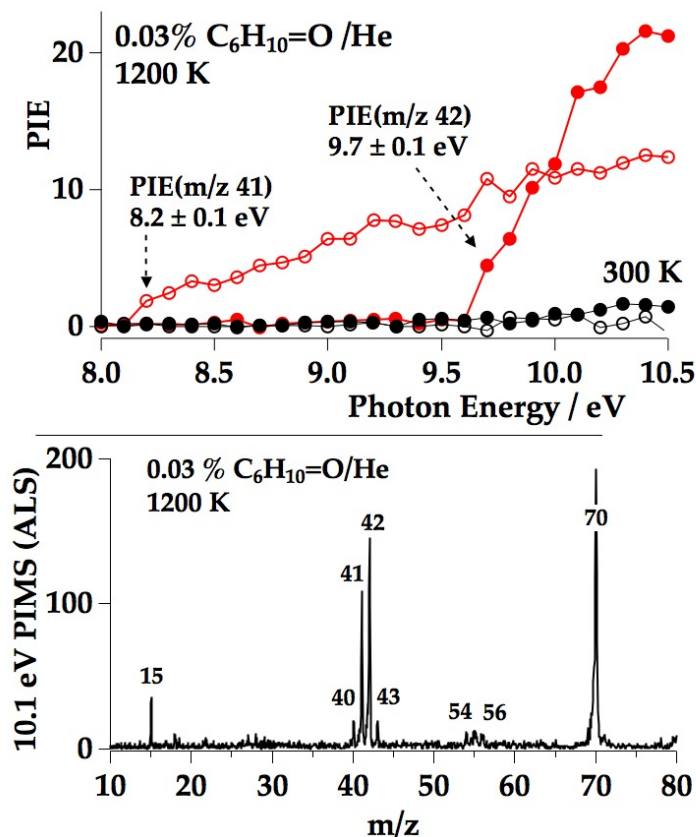


Figure 2.4: Photoionization mass spectra at 10.1 eV of cyclohexanone at 1200 K in a continuous flow micro-reactor. The inset at the top shows the $\text{PIE}(m/z 41)$ and $\text{PIE}(m/z 42)$; the thresholds for both of these ions confirm the presence of CH_2CHCH_2 and $\text{CH}_2=\text{C}=\text{O}$ (see Table 2.4).

is consistent with the presence of the enol, $\text{CH}_2=\text{C}(\text{OH})-\text{CH}=\text{CH}_2$. Fig. 2.7 shows scans of the photoionization efficiency curves for m/z 15, 26, and 42. The thermal cracking of an authentic sample of MVK at 1200 K would appear to confirm the chemistry in Scheme 2.3. The $\text{PIE}(m/z 15)$, $\text{PIE}(m/z 26)$, and $\text{PIE}(m/z 42)$ traces all show the proper appearance energies for CH_3 , $\text{HC}\equiv\text{CH}$, and $\text{CH}_2=\text{C}=\text{O}$. The species at m/z 27 (CHCH_2^+) and 55 (CH_2CHCO^+) are due to dissociative ionization from the MVK enol while m/z 18 is background H_2O ionized by the higher synchrotron harmonics.

In the remainder of this subsection, having confirmed the presence of all possible channels shown in Schemes 1-3, the rest of the predicted products and observed PIMS peaks are discussed. Other possible products in Fig. 2.4 resulting from Scheme 2 are cyclopentane (m/z 70), 1,4-pentadiene (m/z 68), cyclobutane (m/z 56), 1-butene (m/z 56), and 1,3-butadiene (m/z 54). Cyclopentane will be masked because m/z 70 also belongs to the enol $\text{CH}_2=\text{CH}-\text{C}(\text{OH})-\text{CH}=\text{CH}_2$ which ionizes

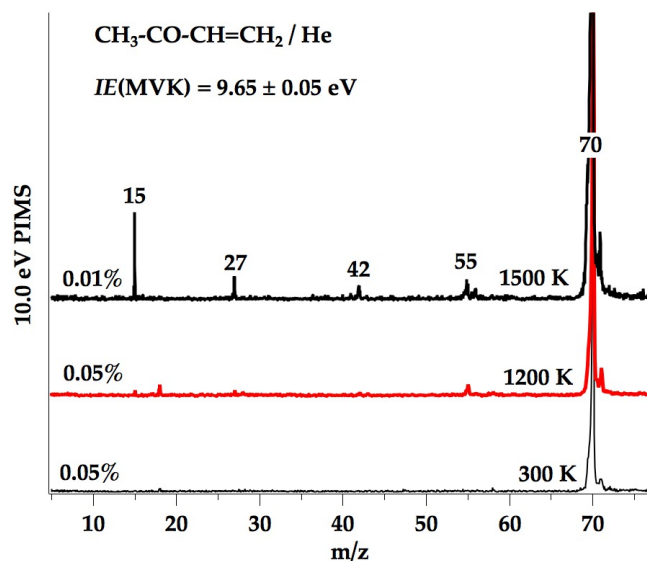


Figure 2.5: Photoionization mass spectra at 10.0 eV of an authentic sample of $\text{CH}_3\text{COCH=CH}_2$ (MVK) at room temperature, 1200 K, and 1300 K in a continuous flow SiC micro-reactor.

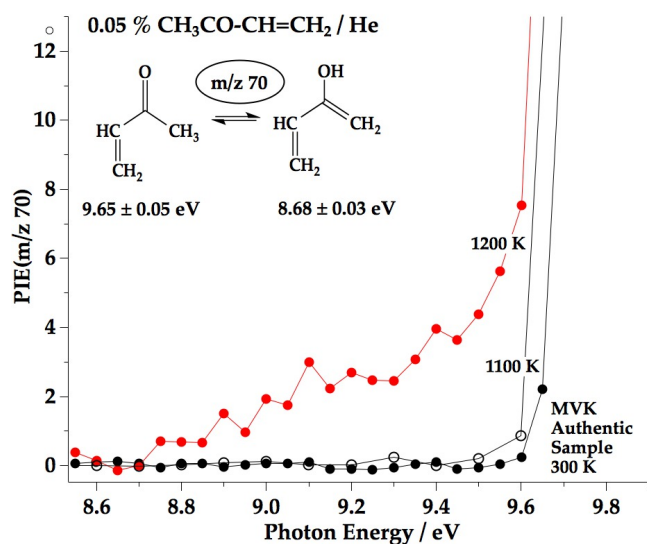


Figure 2.6: Photoionization efficiency curves for m/z 70 from an authentic sample of $\text{CH}_3\text{COCH=CH}_2$ (MVK) at room temperature, 1100 K, and 1200 K in a continuous SiC micro-reactor.

at 8.7 eV (see Table 2.4). The feature at m/z 56 in Fig. 2.4 could be due to either cyclobutane or 1-butene; however the $\text{PIE}(m/z$ 56) is inconclusive. The presence of 1,3-butadiene (m/z 54) is confirmed by the $\text{PIE}(m/z$ 54) scan with the proper appearance energy of $9.2 \pm 0.2 \text{ eV}$ (Fig. 2.13). Other small features in Fig. 2.4 are assigned to $\text{CH}_2\text{=C=CH}_2$ (m/z 40) and acetyl (m/z 43).

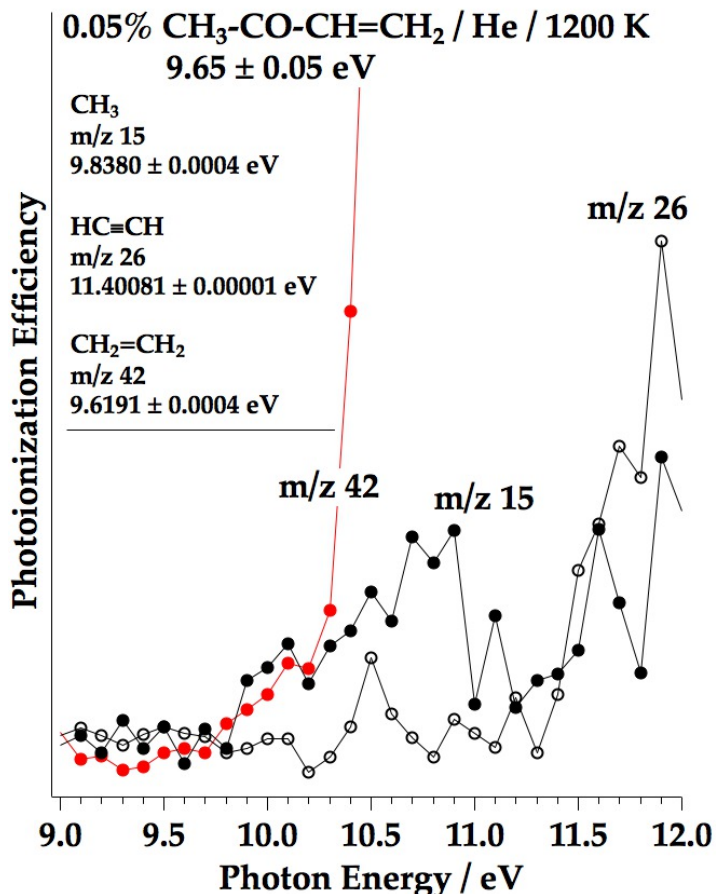


Figure 2.7: Photoionization efficiency scans at m/z 15, m/z 26, and m/z 42 from a dilute (0.05 %) sample CH₃COCH=CH₂ (MVK)/He at 1200 K in a continuous flow SiC micro-reactor.

Scheme 2.2 predicts the formation of allene from pyrolysis of allyl radical; the CH₃CO⁺ ion is the product of dissociative ionization of the enol of MVK.

Retro-Diels-Alder fragmentation (Scheme 2.1) and all of the radical channels in Scheme 2.2 predict the formation of ethylene. The bottom panel of Fig. 2.8 is a 10.7 eV PIMS scan of the cyclohexanone pyrolysis products in a 1200 K continuous flow micro-reactor. The small feature at m/z 43 is CH₃CO⁺ while that at m/z 27 is HCCH₂⁺ and both arise from MVK dissociative ionization (Scheme 2.7). There is also a small feature at m/z 18 that is H₂O⁺ resulting from ionization of background water by synchrotron higher harmonics. The top panel of Fig. 2.8 is an 11.8 eV PIMS scan. In addition to the intense ethylene peak (m/z 28), a new feature is observed at m/z 26 which is attributed to HC≡CH. Additional evidence for this assignment is a PIE with the appropriate appearance energy of 11.4 ± 0.1 eV (see Fig. 2.12). PIMS of heated cyclohexanone

with 11.8 eV is accompanied with extensive dissociative ionization that is the source of the intense CH_3CO^+ feature at m/z 43. The feature at m/z 39 is HCCCH_2^+ and this is probably from dissociative ionization as well. The likely pathways for the formation of these daughter ions are shown in the Schemes 2.6 and 2.7 in the supplementary material.

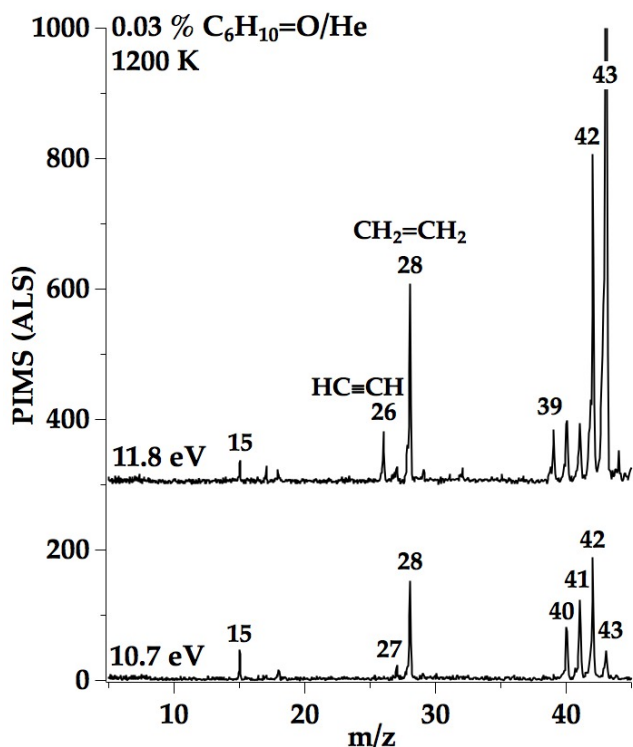


Figure 2.8: Photoionization mass spectrum (10.7 and 11.8 eV) of cyclohexanone heated to 1200 K in a continuous flow micro-reactor.

2.4.4 Matrix Infrared Absorption Spectroscopy

To confirm the pathways derived by PIMS, matrix IR spectroscopy is used. Fig. 2.9 is the argon matrix IR spectrum that results when 0.25% cyclohexanone is heated in Ar to 1300 K. Both the retro Diels-Alder-Reaction and diradical cleavage pathways are open at 1300 K, as evidenced by MVK and ethylene, as well as the allyl radical, respectively. The intense $\nu_7(\text{CH}_2=\text{CH}_2)$ is detected; the characteristic C=O stretch of MVK, $\nu_6(\text{CH}_3\text{C}=\text{OCHCH}_2)$, as well as $\nu_{23}(\text{MVK})$ are also shown. As in the 9.0 eV PIMS Figure 2.2, IR signals from the allyl radical appear in tandem with the retro Diels-Alder products, signifying that all channels presented in Scheme 2.1 are active under

the same reaction conditions. Fig. 2.10 confirms the production of acetylene, ketene, and allene: $\nu_3(\text{HC}\equiv\text{CH})$, $\nu_2(\text{CH}_2=\text{C}=\text{O})$, and $\nu_6(\text{CH}_2=\text{C}=\text{CH}_2)$ are all observed. Acetylene arises from the further decomposition of MVK (Scheme 2.3). The ν_6 band for allene in Fig. 2.8 is the $\text{C}=\text{C}=\text{C}$ asymmetric stretch and is characteristic of cumulated double bonds. [134] The IR spectra confirms the PIMS assignment of $\text{CH}_2=\text{C}=\text{CH}_2$ (m/z 40) in Fig. 2.4.

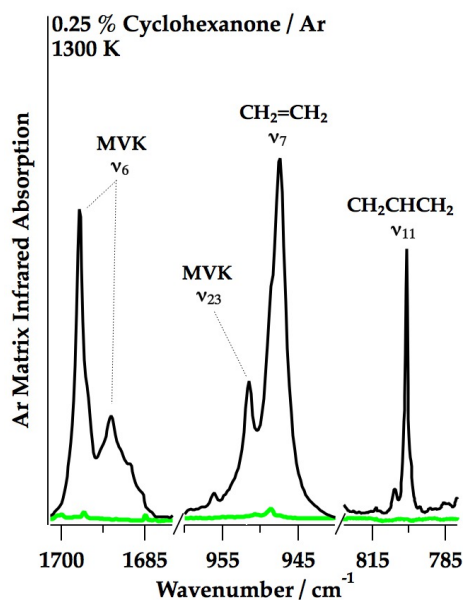
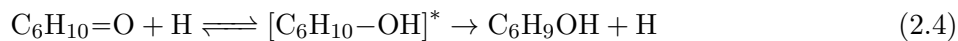


Figure 2.9: Infrared spectrum of cyclohexanone (0.025%) at 1300 K in a pulsed flow micro-reactor. Features for ethylene, [134] $\nu_7(\text{CH}_2=\text{CH}_2)$, methyl vinyl ketone, [77] $\nu_6(\text{MVK})$, and allyl radical, [103] $\nu_{11}(\text{CH}_2\text{CHCH}_2)$, are assigned. Green trace is Ar background heated to 1300 K.

2.4.5 H-Atom Catalysis

As mentioned earlier, the experiments (Fig. 2.2) provide strong evidence for the production of the enols of cyclohexanone and MVK. These products, however, could also be a result of H atom bimolecular chemistry. The formation of CH_2CHCH_2 radicals in Scheme 2.2 is accompanied by production of H atoms, which are highly reactive. If the cyclohexanone samples undergoing pyrolysis are not dilute enough, there is the possibility that H atoms could catalyze the keto/enol isomerization:



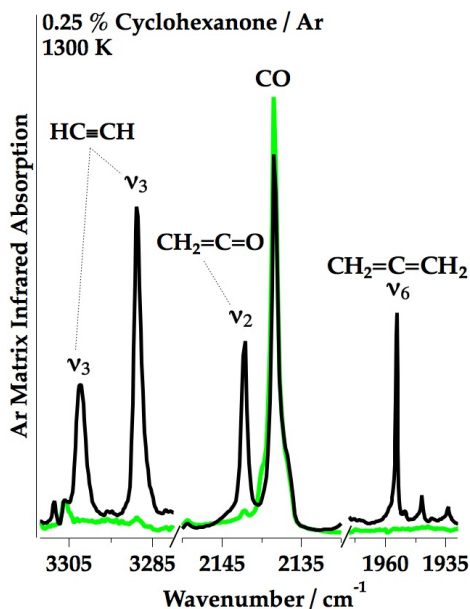
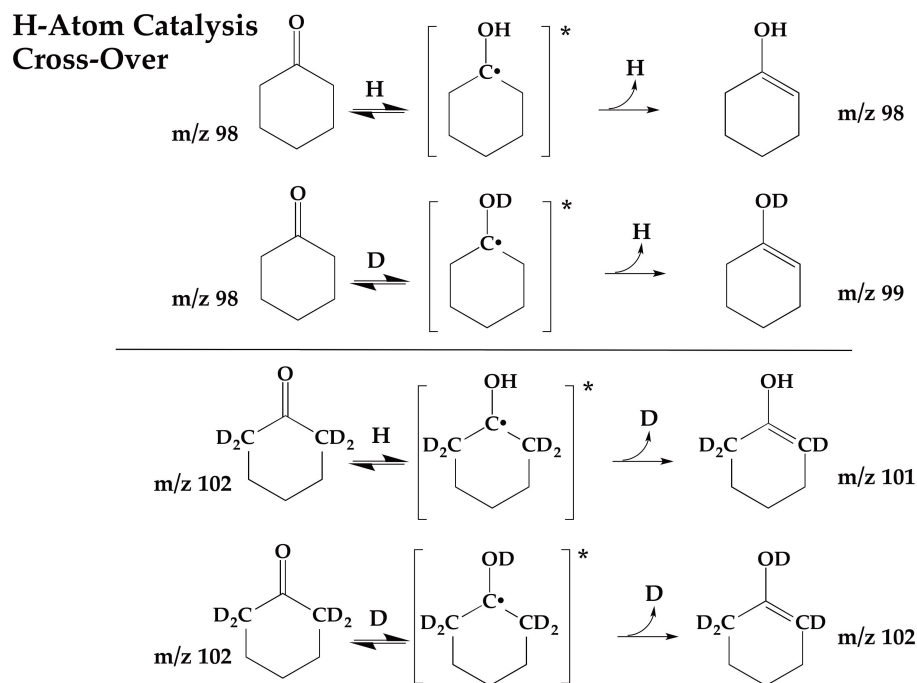


Figure 2.10: Argon matrix IR spectrum of cyclohexanone at 1300 K in a pulsed flow micro-reactor. Bands for acetylene, [134] $\nu_3(\text{HCCH})$, ketene, [97] $\nu_2(\text{CH}_2=\text{C}=\text{O})$, and allene, [134] $\nu_6(\text{CH}_2=\text{C}=\text{CH}_2)$, are assigned. The green trace is Ar background heated to 1300 K.

The pyrolysis of a 50:50 mixture of cyclohexanone- d_0 and cyclohexanone- d_4 however, would reveal the presence of hydrogen atom catalysis as described by Eq. 2.4. This cross-over experiment is outlined in Scheme 2.4. H-atom catalysis in 50:50 mixture of cyclohexanone- d_0 (m/z 98) and cyclohexanone- d_4 (m/z 102) would lead to a mixture of isotopomers at m/z (98, 99, 101, 102). Figure 2.11 shows the experimental result of the thermal cracking of a dilute mixture (0.06 % in helium) of a 50:50 mixture of cyclohexanone- d_0 and cyclohexanone- d_4 . In this experiment, the cyclohexanone pyrolysis is carried out in a pulsed SiC micro-reactor (see entry 2 on Table 1.1). The PIMS scan at 300 K and 10.487 eV shows only peaks at m/z 98 and m/z 102. Heating to 1200 K, where keto/enol isomerization is thought to occur, does not produce any signals at m/z 99 or m/z 101. Consequently there is no evidence produced for H-atom catalysis in the decomposition of cyclohexanone in our reactor at concentrations below 0.06% and it therefore seems that secondary chemistry of this kind is not occurring under the reaction conditions used in our experiments.



Scheme 2.4: Predicted cyclohexanone d_0 and d_4 H/D atom chemistry with H catalysis.

2.4.6 Discussion

Decomposition of cyclohexanone begins around 1200 K in the micro-reactor. All of the PIMS, PIE, and IR spectra lead to the conclusion that cyclohexanone thermally fragments by the multiple pathways, all of which are depicted in Schemes 2.1 - 2.3. Care has been taken to use dilute cyclohexanone samples to avoid bimolecular chemistry, see details in the previous section. The results of cyclohexanone pyrolysis are summarized in Table 2.5. Many of the predicted products from Schemes 2.1 - 2.3 have been detected by at least two complementary measurements.

Thermochemical estimates discussed previously and a set of G3B3 calculations [175] suggest the lowest pathway for cyclohexanone pyrolysis to be the keto/enol isomerization, followed by the retro-Diels-Alder fragmentation, see Scheme 2.1. At higher energies (roughly 0.5 eV) the radical channel pathways of Scheme 2.2 are predicted to appear; however, the experimental observations do not reveal distinct onsets of these two pathways. Both the PIMS spectra in Figures 2.2 and 2.5 and the IR spectrum (Figures 2.7 and 2.8) clearly reveal the presence of allyl radical and ketene (predicted from Scheme 2.2) as well as enols, C_6H_9OH and $CH_2=C(OH)-CH=CH_2$ (predicted by Scheme 2.1), at 1200 K. The PIMS and IR spectra are consistent with simultaneous opening of the

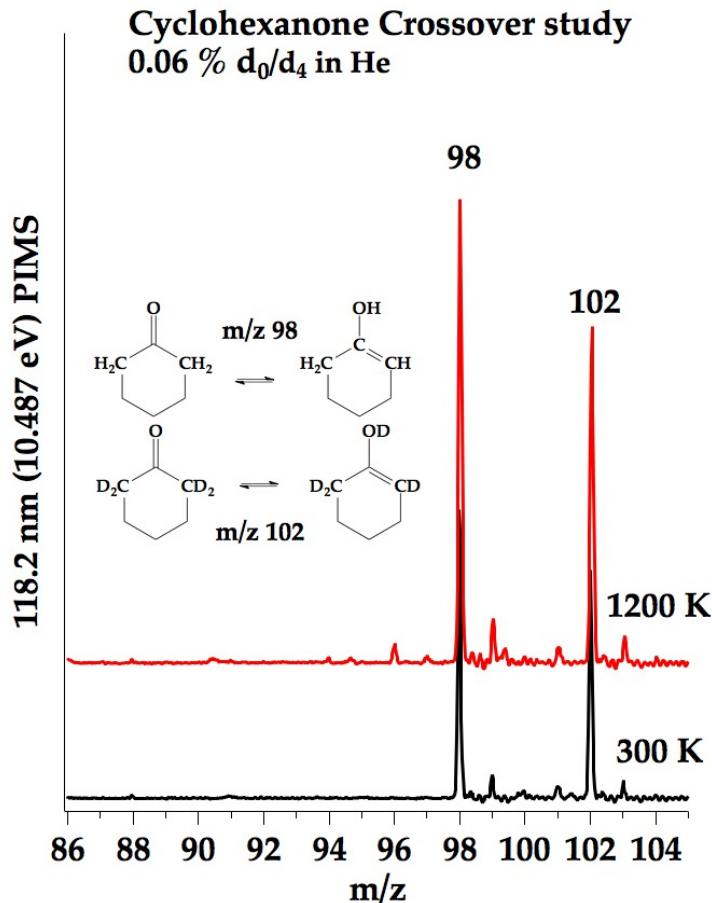


Figure 2.11: Photoionization mass spectrum of cyclohexanone d_0/d_4 crossover experiment at 118.2 nm (10.487 eV) in a pulsed micro-reactor. The feature at m/z 99 is the ^{13}C isotope peak of $\text{C}_6\text{H}_{10}=\text{O}$ and m/z 101 is a contamination of cyclohexanone d_4 sample.

pathways in Schemes 2.1 and 2.2.

At 1200 K, it is evident that some of primary cyclohexanone pyrolysis products continue to decompose. The PIE scan in Figure 2.7 confirms that MVK decomposes to produce small amounts of CH_3 , $\text{CH}_2=\text{C}=\text{O}$, and $\text{HC}\equiv\text{CH}$. The 118.2 nm PIMS of 1-butene heated in a pulsed He reactor (Figure S3 in the Supporting Information) shows extensive decomposition to methyl and allyl radicals around 1200 K; however, authentic samples of $\text{CH}=\text{CH}-\text{CH}=\text{CH}$ and cyclopentane are stable at 1200 K.

Problems of dissociative ionization can be better understood now. The essential factor driving the fragmentation of the radical cations $[\text{cyclohexanone}]^+$ and $[\text{methyl vinyl ketone}]^+$ is the isomerization of the ketones to the enols. Because the ionization energies of the enols, $\text{C}_6\text{H}_9\text{OH}$ and

$\text{CH}_2=\text{C}(\text{OH})-\text{CH}=\text{CH}_2$, are 1 eV below that of the ketones (see Table 2.4), photoionization by 118.2 nm photons leads to the highly chemically activated ions, $[\text{C}_6\text{H}_9\text{OH}^*]$ and $[\text{CH}_2=\text{C}(\text{OH})-\text{CH}=\text{CH}_2^*]$. Photoionization of cyclohexanone with 118.2 nm (10.487 eV) light is 1.3 eV above threshold and Figure 2.1 displays no dissociative ionization. Heating $\text{C}_6\text{H}_{10}=\text{O}$ to 1200 K triggers isomerization to the enol, $\text{C}_6\text{H}_9\text{OH}$. Photoionization by 118.2 nm photons is 2.3 eV above the $\text{C}_6\text{H}_9\text{OH}$ ionization threshold and dissociative ionization ensues. The fragmentation of $\text{CH}_3\text{COCH}=\text{CH}_2$ in Figure 2.5 can be explained the same way. At 300 K there is no dissociation of $\text{CH}_3\text{COCH}=\text{CH}_2^+$. Heating the sample to 1200 K isomerization MVK to $\text{CH}_2=\text{C}(\text{OH})-\text{CH}=\text{CH}_2$ and lowers the ionization energy by 1 eV. Photoionization with 10 eV light is 0.4 eV above the $IE(\text{MVK})$ but is 1.4 eV over the ionization threshold of $\text{CH}_2=\text{C}(\text{OH})-\text{CH}=\text{CH}_2$.

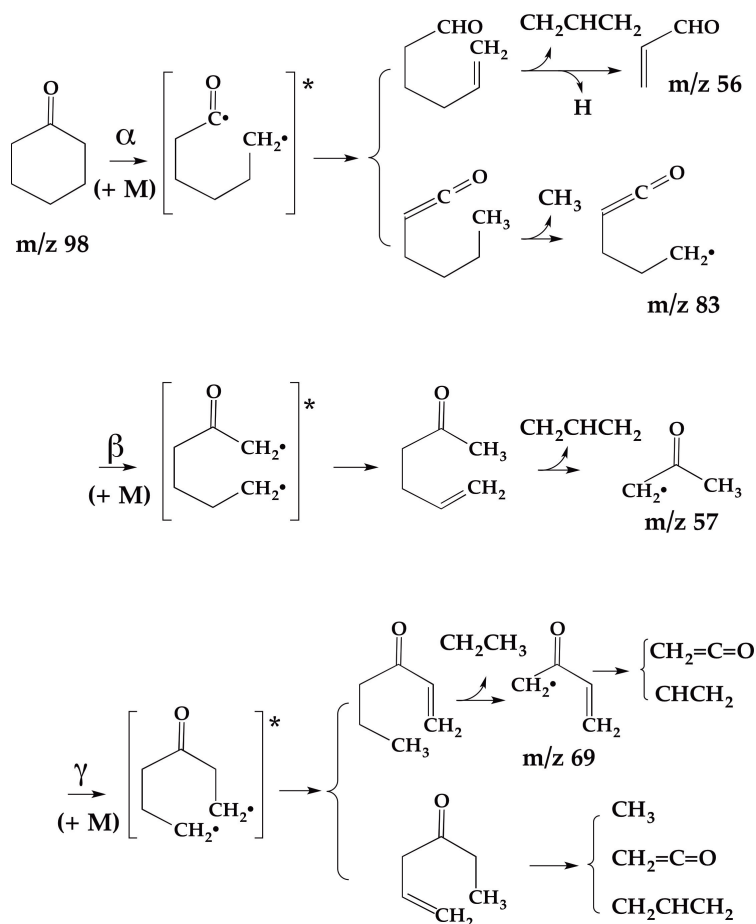
Examination of the 118.2 nm cyclohexanone PIMS in Figure 2.1 shows the 300 K scan to be normal and only the parent ion [30, 83] of cyclohexanone, m/z 98, and the ^{13}C -isotopomer (m/z 99) are observed. Appreciable cyclohexanone fragmentation is first observed upon heating to 1000 K when the enol, $\text{C}_6\text{H}_9\text{OH}$, is beginning to form. Both radical cations, $(\text{C}_6\text{H}_9\text{OH})^+$ and $(\text{CH}_2=\text{C}(\text{OH})-\text{CH}=\text{CH}_2)^+$, would be expected to undergo a McLafferty rearrangement [90, 91] and produce the chemically activated ketones, $[\text{C}_6\text{H}_{10}=\text{O}^*]^+$ and $[\text{CH}_3-\text{CO}-\text{CH}=\text{CH}_2^*]^+$. Possible pathways for dissociative ionization are shown in the Schemes 2.6 (cyclohexanone) and 2.7 (MVK), which are included in the Supporting Information of this chapter.

There is one final complication that might affect the pyrolysis of cyclohexanone. The decomposition pathways in Scheme 2.2 show the three sets of diradicals (α , β , or γ) promptly extruding carbon monoxide or ketene. We should consider the consequences that would ensue if these radical pairs persisted long enough to react with each other. Recent shock tube studied [71] of the pyrolysis of cyclohexane reveal that around 1200 - 1300 K, *c*- C_6H_{12} isomerizes to $\text{CH}_2=\text{CH}-\text{CH}_2\text{CH}_2\text{CH}_2\text{CH}_3$. The six-membered ring ruptures a C-C bond and produces the diradical, $[\cdot\text{CH}_2\text{CH}_2\text{CH}_2\text{CH}_2\text{CH}_2\text{CH}_2\cdot]$, which persists long enough for an internal radical to abstract a hydrogen atom and produce the alkene, 1-hexene.

If any of the (α , β , or γ) diradicals in Scheme 2.2 live long enough to react with themselves, the chemistry in Scheme 2.5 results. The α radical pair could disproportionate to the aldehyde, $\text{CH}_2=\text{CH}-(\text{CH}_2)_3-\text{CHO}$, which is expected to decompose to the allyl radical (CH_2CHCH_2) and acrolein ($\text{CH}_2=\text{CH}-\text{CHO}$). Alternatively, the ketene ($\text{CH}_3\text{CH}_2\text{CH}_2\text{CH}_2\text{CH}=\text{C}=\text{O}$) could form and

decompose to methyl radical (m/z 15) and the $\text{CH}_2\text{CH}_2\text{CH}_2\text{CH}=\text{C}=\text{O}$ radical, m/z 83. Disproportionation of the β radical pair yields the ketone, $\text{CH}_3\text{CO}-\text{CH}_2\text{CH}_2\text{CH}=\text{CH}_2$. Loss of allyl radical produces the CH_2COCH_3 , which is expected to fragment to CH_3 and $\text{CH}_2=\text{C}=\text{O}$. Dis-

Diradical Disproportionation



Scheme 2.5: Diradical Disproportionation Pathways for Cyclohexanone

proportionation of the γ radical pair leads to the isomeric alkene, $\text{CH}_3\text{CH}_2\text{CH}_2\text{COCH}=\text{CH}_2$ and $\text{CH}_2=\text{CHCH}_2\text{COCH}_2\text{CH}_2$. Both molecules are expected to dissociate to a mixture of (CH_2CO , CHCH_2) and (CH_2CHCH_2 , CH_2CO , CH_3). There are few unique products arising from the radical/radical disproportionations of the (α , β , or γ) radical pairs. Weak signals from m/z 83 are present in Figure 2.1 at 1000 K that could be attributed to the $\text{CH}_2\text{CH}_2\text{CH}_2\text{CH}=\text{C}=\text{O}$ radical. It will be difficult to identify much of the chemistry in Scheme 2.5.

The results of cyclohexanone pyrolysis in a micro-reactor provide insight regarding the previous

pyrolysis study [38]. It is important to remember that these two experiments have significant differences between them. The 1970 study carried out pyrolysis at 1300 K in a ceramic tube at low pressures (60 mTorr) with exposure times of approximately 10 ms. The decomposition products were collected and analyzed by electron impact mass spectroscopy and gas chromatography with a flame ionization detector; consequently, the identification of metastables and radical products is very difficult or simply impossible. Under these conditions, the products of thermally cracking cyclohexanone were reported as listed in Eq. 2.1 [38].

The results from this study are largely comparable with the 1970 results. The microreactor studies summaries in Table 2.5 include both ethylene and MVK, the two most important products from the ceramic flow reactor [38]. The origin of propene in Eq. 2.1 can plausibly be attributed to quenching of the CH_2CHCH_2 radicals. The radical channel in Scheme 2.2 is the pathway for formation of $\text{CH}_2=\text{C}=\text{CH}_2$, $\text{CH}_2=\text{CHCH}_2\text{CH}_3$, $\text{CH}_2=\text{CH}-\text{CH}=\text{CH}_2$, cyclopentane, and $\text{CH}_2=\text{CH}-\text{CH}_2\text{CH}=\text{CH}_2$. Recombination of CH_3 radicals will produce the ethane in Eq. 2.1 and acetylene arises from the thermal cracking of MVK. The cyclohexanone pyrolysis results in

m/z	species	name	PIMS	PIE	IR
15	CH_3	methyl radical	Figure 2.4	Figure 2.5	
26	$\text{HC}\equiv\text{CH}$	acetylene	Figure 2.6	Figure 2.12	Figure 2.8
28	$\text{CH}_2=\text{CH}_2$	ethylene	Figure 2.6	Figure 2.12	Figure 2.7
40	$\text{CH}_2=\text{C}=\text{CH}_2$	allene	Figure 2.4		Figure 2.8
41	CH_2CHCH_2	allyl radical	Figure 2.2	Figure 2.4	Figure 2.7
42	$\text{CH}_2=\text{C}=\text{O}$	ketene	Figure 2.3	Figure 2.4	Figure 2.8
54	$\text{CH}_2=\text{CH}-\text{CH}=\text{CH}_2$	1,3-butadiene	Figure 2.4	Figure 2.13	
56	$\text{CH}_2=\text{CHCH}_2\text{CH}_3$	1-butene	Figure 2.4		
56	C_4H_8	cyclobutane			
68	$\text{CH}_2=\text{CHCH}_2\text{CH}=\text{CH}_2$	1,4-pentadiene			
70	$\text{CH}_2=\text{CHCH}_2\text{CH}_2\text{CH}_3$	1-pentene			
70	C_5H_{10}	cyclopentane			
70	$\text{CH}_3\text{CO}-\text{CH}=\text{CH}_2$	methyl vinyl ketone	Figure 2.1	Figure 2.4	Figure 2.8
70	$\text{CH}_2=\text{C}(\text{OH})-\text{CH}=\text{CH}_2$	1,3-butadiene-2-ol	Figure 2.2	Figure 2.4	
98	$\text{C}_6\text{H}_9\text{OH}$	cyclohexene-1-ol	Figure 2.2	Figure 2.3	

Table 2.5: Detected Products from 1200 K Pyrolysis of Cyclohexanone

Table 2.5 are more difficult to compare to the recent $\text{C}_6\text{H}_{10}=\text{O}$ oxidation study of the jet-stirred reactor [133]. The conditions of the jet-stirred reactor (pressures of 10 atm, temperatures of 500 - 1200 K, and exposure times of 0.7 s) are significantly different from the microreactor studies here. The jet-stirred reactor examined the products of oxidation, while the present study is only that of

anaerobic pyrolysis.

Some of the products from cyclohexanone pyrolysis in the micro-reactor in Table 2.5 agree with the predictions from the recent computational study [175]. This investigation examined the unimolecular thermal decomposition of cyclohexanone by the means of DFT electronic structure calculations and master equation simulations. Figure 2.2 in ref [175] explored several different pathways for cyclohexanone decomposition and predicted the keto/enol isomerization to cyclohexen-1-ol, followed by retro-Diels-Alder fragmentation.

This study of the pyrolysis of cyclohexanone demonstrates the simplifying power of tunable synchrotron radiation as a VUV photoionization source. As the sample cyclohexanone is heated by the micro-reactor, isomerization of the ketone begins. The fixed frequency 118.2 nm PIMS spectrum in Figure 2.1 is cluttered with many ions that result from dissociative ionization of the target cyclohexanone, Eq. 2.3. The daughter ions from $[\text{C}_6\text{H}_9\text{OH}]^+$ fragmentation obscure many of the pyrolysis products. The problems with dissociative ionization could be circumvented by extensive use of matrix IR spectroscopy, and the effectiveness of a tunable VUV source offered by a synchrotron is evident from Figures 2.2 - 2.6. With these tools I've been able to show that both isomerization followed by retro-Diels-Alder reaction occurs with cyclohexanone upon heating. Under the given micro-reactor conditions, allyl radical signifies that available radical channels are also opened simultaneously.

2.5 Supporting Information

A Brief Summary of the Modified HEAT - 345 Q Thermochemistry Calculation

1. Molecular geometries are optimized with all active electrons (AE)-CCSD(T)/cc-pVQZ level of theory.
2. ZPEs are computed using second-order vibrational perturbation theory (VPT2). FC-CCSD(T)/ANO1 harmonic and FC-CCSD(T)/ANO0 anharmonic force fields are used.
3. SCF-HF energies are calculated using the correlation-consistent basis sets cc-pVXZ (with X = 3(T), 4(Q), and 5). These three energies are then extrapolated to the complete basis set limit in order to obtain the SCF-HF energy.

$$E_{\text{HF}}^X = E_{\text{HF}}^{\infty} + a * \exp(-bX)$$

4. CCSD(T) correlation energies are calculated using the basis sets cc-pVXZ (with X = 4 (Q) and 5). The frozen-core (FC) CCSD(T) correlation energy extrapolated to the complete basis set limit is then obtained.

$$\Delta E_{\text{CCSD(T)}}^X = \Delta E_{\text{CCSD(T)}}^{\infty} + aX^{-3}$$

5. Core-valence correction energies are calculated as the difference in energy between (all electron) AE-CCSD(T)/cc-pCVTZ and FC-CCSD(T)/cc-pVTZ levels of theory.

$$\Delta E_{\text{core}} = \Delta E_{\text{cc-pCVTZ}} - \Delta E_{\text{cc-pVTZ}}$$

6. Triple excitation effects that are not included in the CCSD(T) treatment of correlation are estimated as the difference in energy between FCCSDT/cc-pVTZ and FC-CCSD(T)/cc-pVTZ levels of theory.

$$\Delta E_{T-(T)} = \Delta E_{CCSDT} - \Delta E_{CCSD(T)}$$

7. Non-iterative quadruple excitation corrections are obtained as a difference in energy between FC-CCSDT(Q)/cc-pVDZ and FC-CCSDT/cc-pVDZ levels of theory.

$$\Delta E_{(Q) - T} = \Delta E_{CCSDT(Q)} - \Delta E_{CCSDT}$$

8. The diagonal Born-Oppenheimer correction (DBOC) is calculated using SCF-HF/aug-cc-pVTZ level of theory. RHF and ROHF methods are used for closed- and open-shell systems, respectively.

9. Spin-orbit corrections are taken from experiment whenever they are available. (No molecules studied in this work are in degenerate electronic states, and so none exhibit a first-order SO effect, but this factor is mentioned here for completeness.)

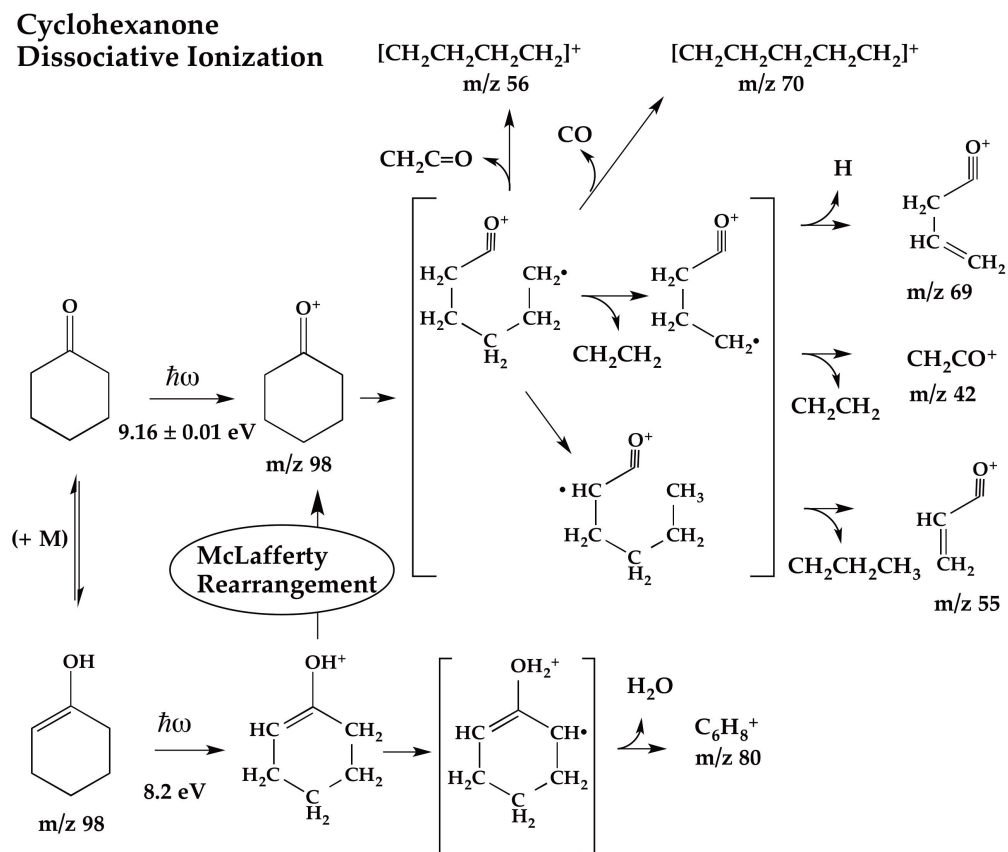
10. Scalar relativistic effects including one- and two-electron Darwin, and mass-velocity terms are calculated using MP2/aug-cc-pCVTZ level of theory. The total energy by the modified-HEAT method can be expressed as:

$$E_{\text{mHEAT}} = E_{HF}^{\infty} + \Delta E_{\text{Core}} + \Delta E_{T - (T)} + \Delta E_{(Q) - T} + \Delta E_{\text{rel}} + \Delta E_{\text{ZPE}} + \Delta E_{\text{DBOC}} \\ + \Delta E_{\text{SO}}$$

Species	TAE	$\Delta_f H_0$	ATcT
H ₂	103.34	-0.07	0.000
CH ₃	392.39	-15.84	-15.91 ± 0.01
C ₂ H ₄	531.99	14.59	14.60 ± 0.04
C ₂ H ₆	666.16	-16.31	-16.28 ± 0.04
C ₃ H ₆	811.40	8.48	7.45 ± 0.08
CH ₃ CHO	642.82	-37.24	-37.02 ± 0.08
CH ₃ C(O)CH ₃	927.07	-48.20	-47.65 ± 0.09
CH ₃ OH	481.38	-45.83	-45.37 ± 0.04
CH ₂ =CH-CH=CH ₂	959.65	30.25	29.8 ± 0.1
CH ₂ =CH(OH)	633.02	-27.44	-26.9 ± 0.2
<i>cis</i> -MVK	1071.7	-22.81	
<i>trans</i> -MVK	1071.34	-22.45	
Enol	1061.78	-12.88	
H			51.63
C			170.02
O			59.00

Table 2.6: Calculated total atomization energies (TAE, kcal mol⁻¹) and heats of formation (kcal mol⁻¹) at 0 K for various species using a modified HEAT-345-Q) method. ATcT values at 0 K are included for comparison

2.6 Supplemental Figures and Schemes



Scheme 2.6: Dissociative ionization of cyclohexanone

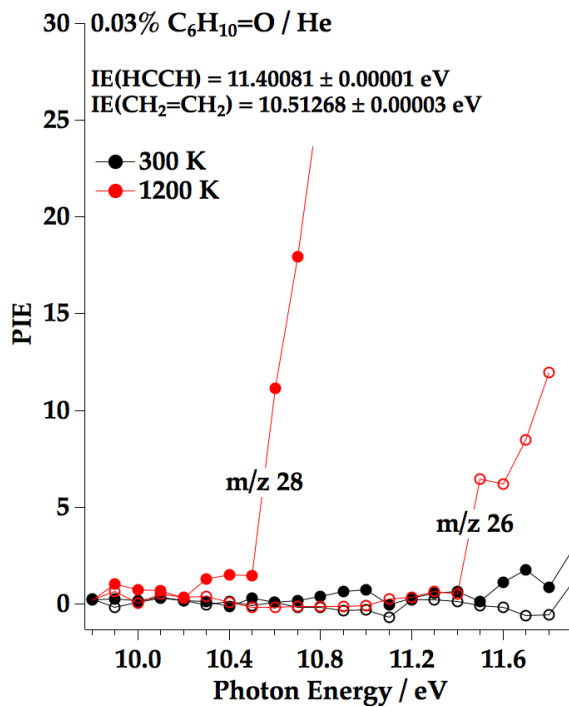


Figure 2.12: Photoionization efficiency curve for m/z 26 and m/z 28 from cyclohexanone in He at 1200 K in a continuous flow micro-reactor.

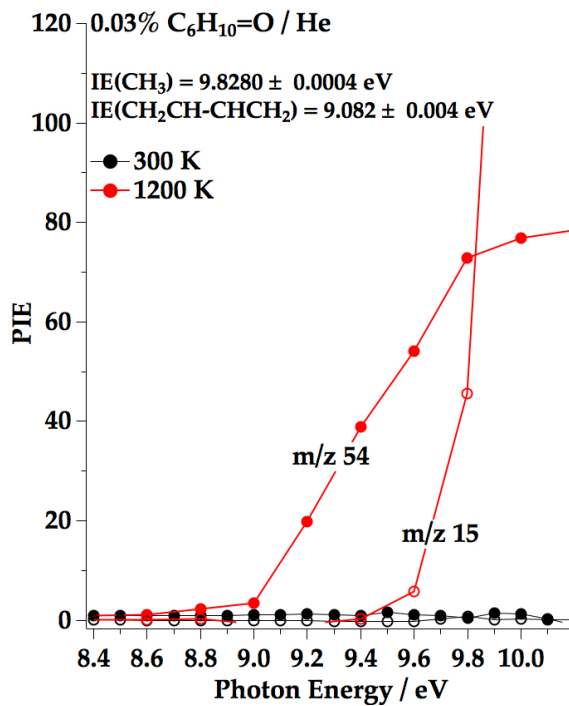


Figure 2.13: Photoionization efficiency curve for m/z 15 and m/z 54 from cyclohexanone in He at 1200 K in a continuous flow micro-reactor.

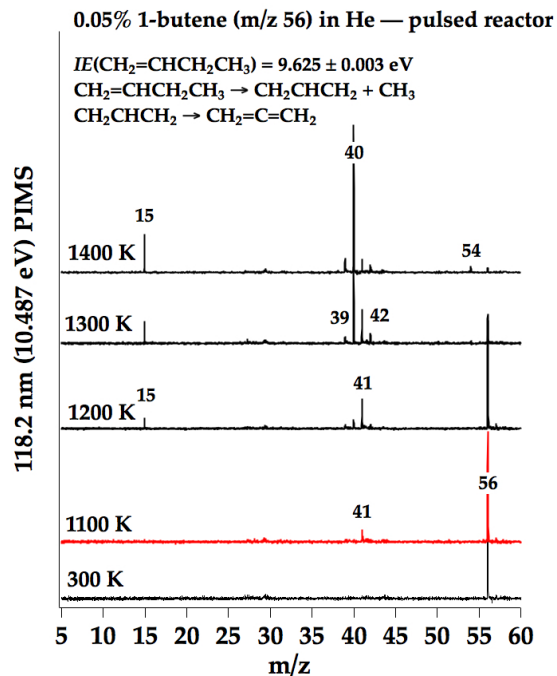


Figure 2.14: Photoionization mass spectrum temperature study of 0.05% 1-butene in He at 10.487 eV (see entry 2 Table 1.1)

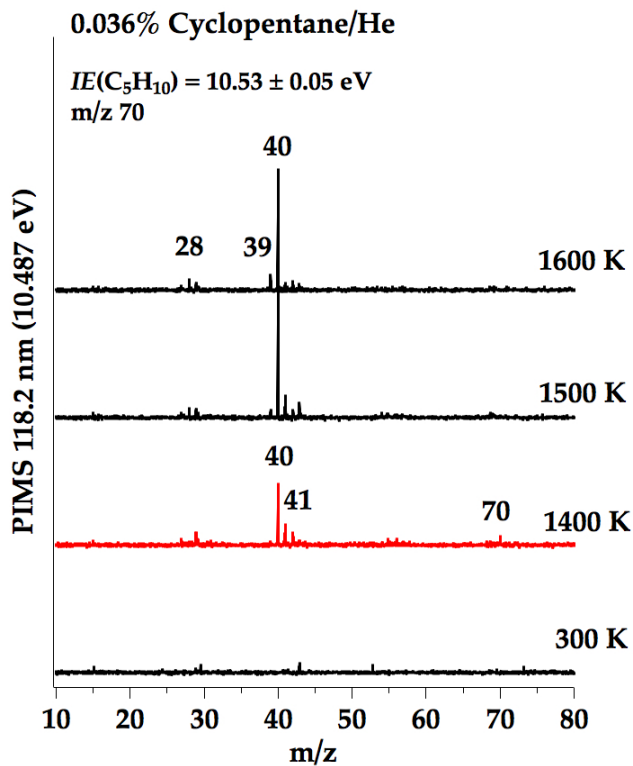
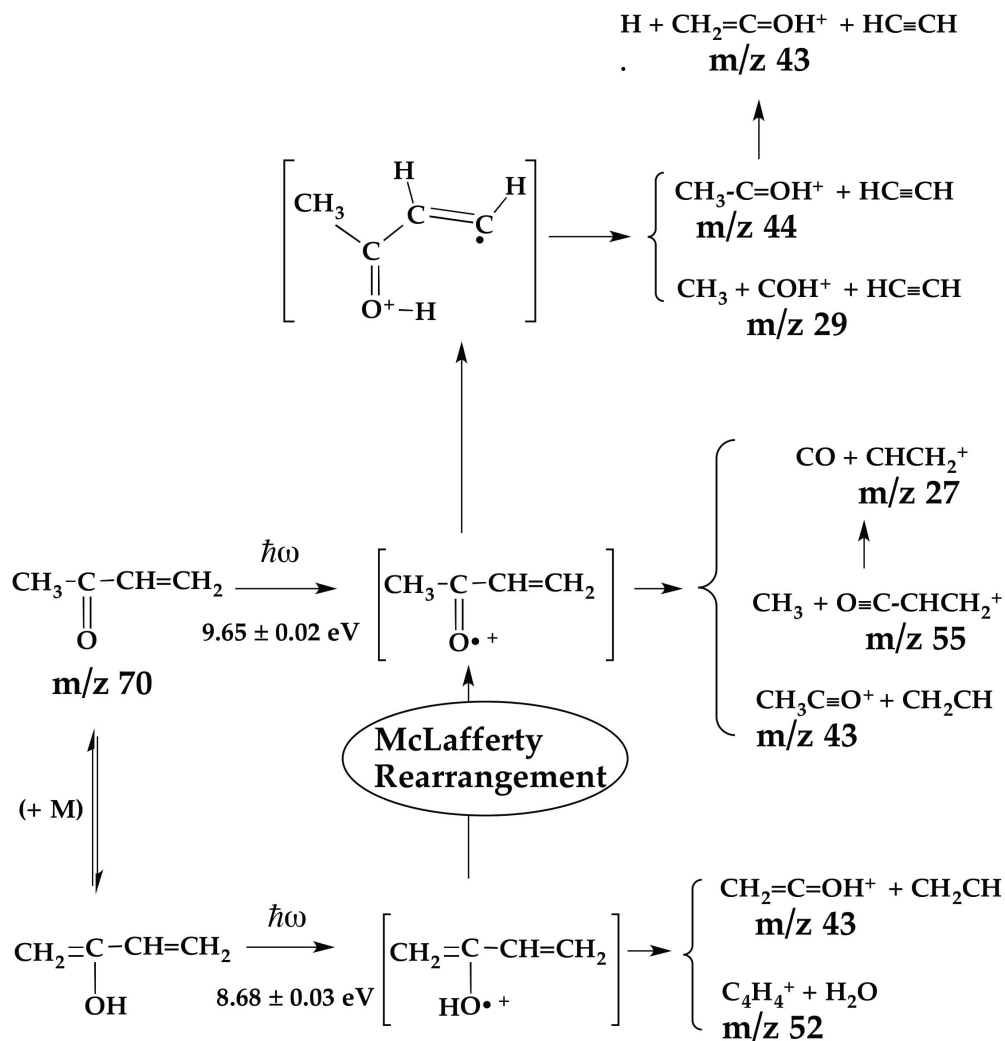


Figure 2.15: Photoionization mass spectrum temperature study of 0.036% cyclopentane in He at 10.487 eV (see entry 2 Table 1.1).

MVK Dissociative Ionization



Scheme 2.7: Dissociative ionization of methyl vinyl ketone.

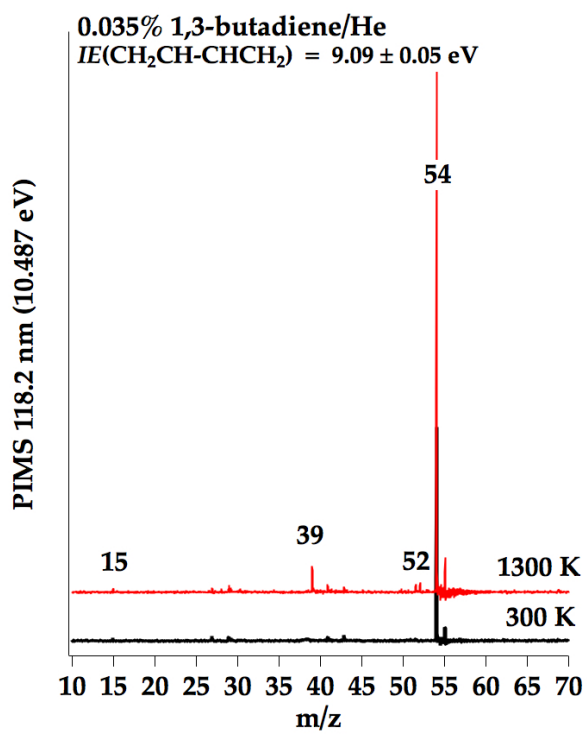


Figure 2.16: Photoionization mass spectrum of 0.035% 1,3-butadiene in He (see entry 2 Table 1.1).

Chapter 3

Glycolaldehyde

3.1 Introduction

The most common components of biomass are carbohydrates and lignins. In fact, carbohydrates are one of the most abundant classes of organic compounds on the planet. [139] To explore the pyrolysis mechanisms of carbohydrates, I have studied the flash pyrolysis of glycolaldehyde, the simplest carbohydrate. A sugar is defined as a carbohydrate $(C \cdot H_2O)_n$ with a minimum of a three carbon backbone (triose). D-glyceraldehyde, $CHO-CHOH-CH_2OH$, is the simplest sugar; its Fischer projection is shown in Figure 3.1. Even this structure is complicated and not well studied experimentally. The gas-phase heat of formation, bond energies, precise molecular structure, and ionization energy are not currently known. Glycolaldehyde, although not quite a sugar, is the only possible diose (two carbon backbone). This simple carbohydrate must be understood before the thermal decomposition of larger, proper sugars can be understood. Figure 3.1 relates glycolaldehyde to glyceraldehyde. I have also described the thermal decomposition of glyoxal in this chapter, a decomposition product of glycolaldehyde and of stand alone importance in atmospheric chemistry.

3.2 Pyrolysis Experiments

Chapter 1 describes the reactors used for this study in great detail, however a few modifications needed to be made due to the high melting and boiling points of glycolaldehyde. Glycolaldehyde is obtained as a solid dimer (see Figure 3.2) and glyoxal as the trimer dihydrate, both are from Sigma

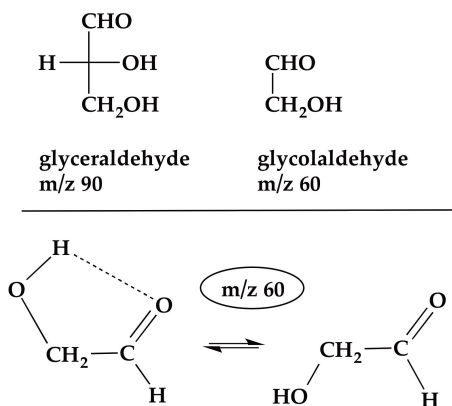


Figure 3.1: Chemical structures of glyceraldehyde and glycolaldehyde.

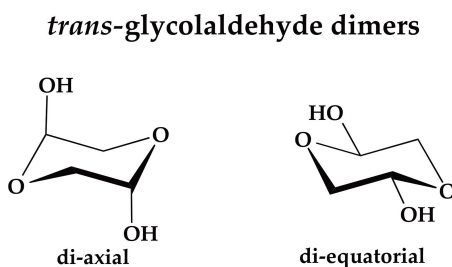


Figure 3.2: Structures of the *trans*-glycolaldehyde dimers.

Aldrich. Samples with low vapor pressures do not easily go into the gas phase, so must be introduced to the reactor by passing the carrier gas through a temperature-controlled vessel containing a few milligrams of reagent. Photoionization mass spectrometry rapidly provides signal, allowing for the sample probe temperature to be finely tuned (Love Controls Series 16A) to achieve a sufficient signal while simultaneously maintaining the low concentrations needed to establish unimolecular reaction conditions. Glycolaldehyde monomer was first observed at sample probe temperatures of about 80°C, and no evidence for the gas-phase dimer was found. Glyoxal was first observed from the trimer dihydrate solid at sample probe temperatures of 120 °C.

3.3 Heat of Formation of Glycolaldehyde

3.3.1 Calorimetry

Materials. Anhydrous ethylene glycol (>99.5%) was used as purchased and was handled under argon. Solid glycolaldehyde dimer was recrystallized from boiling anhydrous methanol, under argon. The solution was cooled to room temperature and then crystallized over several weeks at 4 °C. The residual methanol was removed under vacuum, and the solid was stored in a desiccator.

The pre-weighed glass ampules for calorimetry runs [35] were first evacuated, heated to drive off moisture, then refilled with argon. Ethylene glycol was added by oven-dried, argon-flushed pipet, and the liquid was degassed before flame sealing under vacuum. The solid glycolaldehyde dimer was added to the ampule in an argon-filled glovebag and then sealed under vacuum. A microgram balance was used to obtain the sample mass to the nearest 0.000001 g, reproducible to ± 0.000005 g.

Reaction Calorimetry. The custom reaction calorimetry system has been described previously [87, 99, 162] and is a Wads-style submarine solution calorimeter. [141] The argon-filled, airtight reaction vessel, [102] already containing the sealed ampule, was charged with roughly 150 mL of triethylene glycol dimethyl ether, dried using freshly activated alumina, and a solution of lithium triethyl borohydride in tetrahydrofuran [163] (1.0 M, 4.7 mL; 0.0047 mol, 0.5 g of LiEt₃BH).

The temperature is measured using a Hewlett-Packard quartz thermometer accurate to 0.0001 °C, calibrated against a water triple-point cell at 0 °C. For each reaction run, an electrical calibration is also performed. Each reaction was repeated multiple times to obtain the uncertainty in the measurement, which is reported as twice the standard deviation from the mean, as suggested by Rossini. [125]

Differential Scanning Calorimetry. The enthalpy of fusion of glycolaldehyde dimer was obtained using the same recrystallized sample as was used for reaction calorimetry. The TA SDT Q600 DSC/TGA instrument was calibrated using an indium standard. The samples, in crimped aluminum pans, were heated from room temperature to 125 °C at a rate of 1 °C/min, with a flow rate of 50 mL/min. The sample mass was also recorded during the experiment and was shown to be constant.

3.3.2 Experimental Heat of Formation of Glycolaldehyde

The gas-phase heat of formation of glycolaldehyde, $\Delta_f H_{298}(\text{CHO}-\text{CH}_2\text{OH})$, was determined experimentally using a combination of thermochemical methods. To start, the condensed-phase heat of formation was obtained by reaction calorimetry. Combustion calorimetry has been used for carbohydrates in the past but with mixed results. For example, three combustion studies [2] on solid glycerinaldehyde give combustion enthalpies over an unacceptably large range: - 336.9, - 346.1, and - 348.9 kcal mol⁻¹, and this technique was not used in this study.

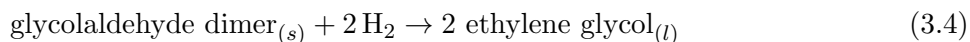
The condensed-phase structure of glycolaldehyde is complicated [94]. The solid form of glycolaldehyde is a dimer that can adopt two distinct conformations (Figure 3.2). Careful recrystallization can generate each structure separately [75]. The X-ray crystal structure of the diaxial conformation has recently been reported [96]. The solid dimer is thought to be stable indefinitely at room temperature [75]. The melting point of the dimer is 80 - 90 °C, depending on the structure, and a viscous liquid persists for days at room temperature, which eventually solidifies. The liquid is composed of monomers, dimers, and potentially other structures such as oligomers [75, 94] whose composition at room temperature presumably changes with time as crystallization occurs. As such, the stable and well defined, solid dimeric form of glycolaldehyde was used for the reaction calorimetry experiments.

The heat of reduction (ΔH_{redn}) of pure, solid glycolaldehyde dimer to pure liquid ethylene glycol was obtained through a two-part thermochemical cycle. This reduction methodology has been successfully used to determine the gas-phase heat of formation for aldehydes and ketones, [163] esters, [164] lactones and epoxides, [99] with excellent agreement with existing experimental data and high-level calculations [99, 162].

In the first reaction, the enthalpy change is measured for the process in which solid glycolaldehyde dimer is introduced to a solution of lithium triethylborohydride in triethylene glycol dimethyl ether, eventually affording the dianion of ethylene glycol in solution, $\Delta H(2)$. Note that the dimeric form of glycolaldehyde is in equilibrium with the monomer when dissolved in solution [94]. In the second reaction, the enthalpy change is measured for dissolving pure liquid HOCH₂CH₂OH in the same reaction medium, yielding the same solution-phase dianion and hydrogen gas, $\Delta H(3)$. The uncertainty in these measurements is twice the standard deviation from the mean [125].



The enthalpies of reaction are measured to be $\Delta_{rxn}H(1 + 2) = -82.01 \pm 0.34 \text{ kcal mol}^{-1}$ [for eqs 3.1 and 3.2] and $\Delta_{rxn}H(3) = -27.85 \pm 0.08 \text{ kcal mol}^{-1}$. Combining reactions 3.1 - 3.3 gives:



It is important to note that the isolated species that result from each of the two experiments are the same; hence, they cancel. The difference is the heat of reduction of pure solid glycolaldehyde to pure liquid ethylene glycol:

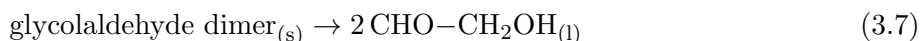
$$\Delta H_{\text{redn}}(4) = \Delta_{rxn}H(1 + 2) - 2\Delta_{rxn}H(3) = -26.32 \pm 0.36 \text{ kcal mol}^{-1} \quad (3.5)$$

It is also true that the heat of reduction of the glycolaldehyde dimer is related to the heats of formation.

$$\begin{aligned} \Delta H_{\text{redn}}(4) &= 2\Delta_f H(\text{HOCH}_2\text{CH}_2\text{OH}, l) - \Delta_f H(\text{glycolaldehyde dimer}, s) \\ &\quad - 2\Delta_f H(\text{H}_2, g) \end{aligned} \quad (3.6)$$

Ethylene glycol has been well-studied, and $\Delta_f H(\text{HO}-\text{CH}_2\text{CH}_2\text{OH}, l)$ has been determined by several research groups. [2]. Using the value [33] of $-108.73 \pm 0.18 \text{ kcal mol}^{-1}$, the heat of formation of solid glycolaldehyde dimer is $-191.14 \pm 0.44 \text{ kcal mol}^{-1}$. The gas-phase heat of formation of glycolaldehyde is then determined by adding the heat of fusion (ΔH_{fus}) and the heat of vaporization (ΔH_{vap}). The ΔH_{fus} of the solid glycolaldehyde dimer was obtained by differential scanning calorimetry. Solid from the same recrystallized sample was used for this experiment as for the reaction calorimetry, so that the ratio of the dimeric conformers was constant. It was important to use a slow heating rate, $1 \text{ }^\circ\text{C/min}$, because the endothermic melting process was followed by a weak

exotherm attributed to the dissociation of liquid dimer to liquid monomer. At this scan rate, the exothermic event was complete before sample evaporation occurred, and the final sample mass was >99.5% of the original mass as determined by thermogravimetric analysis. It is also important to note that there were no solid-solid transitions observed between room temperature and the observed fusion. The standard deviation of the three measurements is 0.2 kcal mol⁻¹. The ΔH_{fus} in (3.7) depends on a calibration constant determined by melting a reference compound, (in this case indium metal), and primarily because of this, the uncertainty of the measurement is increased to 0.4 kcal mol⁻¹, $\Delta H_{\text{fus, uncorrected}}(3.7) = 6.6 \pm 0.4$ kcal mol⁻¹.



A temperature correction to 298.15 K should be applied to this ΔH_{fus} , which is valid at the midpoint of the melting range, approximately 85 °C. The correction was made using the molar heat capacities of the solid and liquid; this correction was especially important to consider in this case because the structures of the solid dimer and liquid monomer are so different.

$$\Delta H_{\text{fus, 298.15}} = \Delta H_{\text{fus, uncorrected}} + (298.15 - T_{\text{mid}})(2C_{pl} - C_{sl}) \quad (3.8)$$

The heat capacities were obtained by group additivity. For the liquid monomer, the Chueh-Swanson values were used, [122] giving 30.62 cal mol⁻¹ K⁻¹. For the solid dimer, the values tabulated by Acree and Chickos were used, [1] giving 33.2 cal mol⁻¹ K⁻¹. The temperature correction is -1.7 ± 0.3 kcal mol⁻¹, so the corrected $\Delta H_{\text{fus, 298.15}}(3.7)$ is 4.9 ± 0.5 kcal mol⁻¹. The heat of formation of two moles of liquid glycolaldehyde is then -186.2 ± 0.7 kcal mol⁻¹, or $\Delta_f H_{\text{liq}}(\text{CHO-CH}_2\text{OH})$ is -93.1 ± 0.4 kcal mol⁻¹.

The ΔH_{vap} of glycolaldehyde can be calculated from vapor pressure versus temperature data available in the literature [115]. The linear data ($r^2 > 0.999$) were fit to the Clausius-Clapeyron equation and provide $\Delta H_{\text{vap}} = 16.9$ kcal mol⁻¹ at 325.9 K. This value can be corrected to 298.15 K using heat capacities, obtained as described above for the liquid phase and using the CBS-APNO calculated value of 15.6 cal mol⁻¹ K⁻¹ for the vapor phase. The corrected ΔH_{vap} is 17.3 ± 1.2 kcal mol⁻¹; the uncertainty here is the same as in the literature data analysis. Together, these data lead to an experimental value for the gas-phase heat of formation for glycolaldehyde,

$\Delta_f H_{298}(\text{CHO}-\text{CH}_2\text{OH})$, of $-75.8 \pm \text{kcal mol}^{-1}$.

The gas-phase ΔH_{redn} of glycolaldehyde to ethylene glycol can also be extracted from the $\Delta_f H_{298}(\text{CHO}-\text{CH}_2\text{OH})$ above and the $\Delta_f H_{\text{liq}}(\text{HOCH}_2\text{CH}_2\text{OH})$. The ΔH_{vap} for ethylene glycol $15.6 \pm 1.0 \text{ kcal mol}^{-1}$ (obtained as described for glycolaldehyde) is added to the $\Delta_f H_{\text{liq}}$ noted above. This gives the gas-phase $\Delta_f H_{298}(\text{HOCH}_2\text{CH}_2\text{OH})$ of $-93.1 \pm 1.0 \text{ kcal mol}^{-1}$ (which is in excellent agreement with Pedley et al. [114]). The resulting $\Delta_{\text{red}} H_{298}(\text{glycolaldehyde})$ is $-17.3 \pm 1.6 \text{ kcal mol}^{-1}$ and compares quite favorably to the $\Delta_{\text{red}} H_{298}(\text{glycolaldehyde})$ value, calculated using CBS-APNO methodology, [109] of $-17.1 \text{ kcal mol}^{-1}$. In the CBS-APNO calculations, three conformations of $\text{HO}-\text{CH}_2\text{OH}$ and 10 conformations of $\text{HOCH}_2\text{CH}_2\text{OH}$ were considered [34] with appropriate multiplicity in an energy-weighted average. The correction to ethylene glycol due to the higher-energy conformations amounts to $0.2 \text{ kcal mol}^{-1}$ (See the Supporting Information at the end of this chapter for further details).

There have been earlier attempts [20, 43] to use electronic structure calculations to predict the gas-phase heat of formation of glycolaldehyde. A G2 calculation reported $\Delta_f H_{298}(\text{CHO}-\text{CH}_2\text{OH})$ to be $-77.6 \pm 1.2 \text{ kcal mol}^{-1}$, while the G3/DFT prediction was $-75.6 \pm 0.8 \text{ kcal mol}^{-1}$. *Ab initio* calculation of the gas-phase heat of formation of glycolaldehyde were performed. The modified HEAT protocol [106] (described above) found $\Delta_f H_0(\text{CHO}-\text{CH}_2\text{OH}) = -73.1 \pm 0.5 \text{ kcal mol}^{-1}$ and $\Delta_f H_{298}(\text{CHO}-\text{CH}_2\text{OH}) = -76.1 \pm 0.5 \text{ kcal mol}^{-1}$. There is good agreement between this completely *ab initio* heat of formation ($-76.1 \pm 0.5 \text{ kcal mol}^{-1}$) and the calorimetrically measured result ($-75.8 \pm \text{kcal mol}^{-1}$).

Although the CBS-APNO method is a composite method and is 'slightly empirical', we also used this procedure to estimate the heat of formation of glycolaldehyde. Using the CBS-APNO methodology, [51, 109] the reduction to ethylene glycol was calculated.



The $\Delta_f H_{298}$ (3.9) was calculated to be $-17.1 \text{ kcal mol}^{-1}$. Since the experimentally determined [33] $\Delta_f H_{298}(\text{HOCH}_2\text{CH}_2\text{OH})$ is $-93.1 \pm 1.0 \text{ kcal mol}^{-1}$, the $\Delta_f H_{298}(\text{glycolaldehyde})$ calculated by the CBS-APNO method is $-76 \pm 1 \text{ kcal mol}^{-1}$.

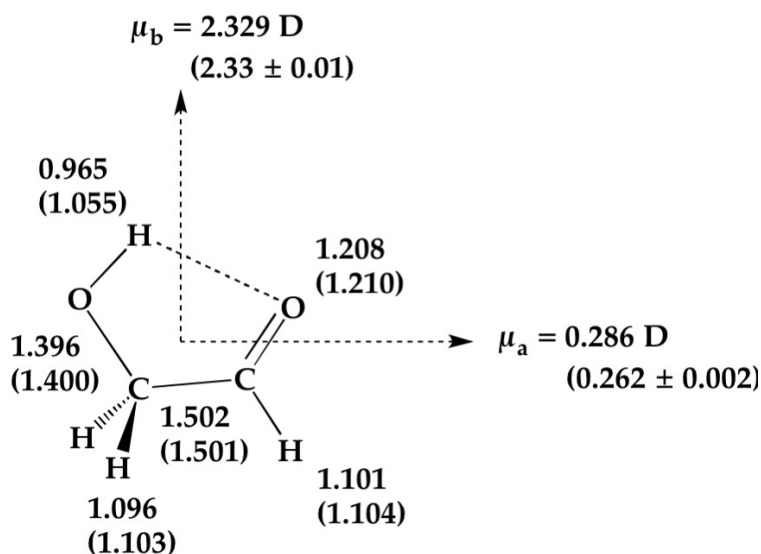
3.3.3 Electronic Structure Calculations

The heat of formation ($\Delta_f H_{298}$) of glycolaldehyde was calculated using a modified HEAT method. [106] The core correlation contribution used here was [AE-CCSD(T)/cc-pCVQZ-FC-CCSD(T)/cc-pCVQZ], which reduces the uncertainty in the calculated heat of formation to 0.5 kcal mol⁻¹. Anharmonic zero-point energies (ZPE) were calculated at the (frozen core) FC-CCSD(T)/ANO0 level of theory with ANO1 harmonic frequencies. We also performed a full FC-CCSD(T)/ANO1 anharmonic calculation and optimized an AE-CCSD(T)/cc-pCVQZ geometry in the course of the structure reinvestigation described below. The adiabatic ionization potentials of the two lowest states of the glycolaldehyde cation were calculated at the EOMIP-FC-CCSD/ANO1 level of theory, using ANO0 harmonic ZPEs. All calculations were performed using the CFOUR program system. [138] Calculations were also performed using CBS-APNO methodology, [109] as implemented in Gaussian 09W. [51] Structures were confirmed to be minima on the potential energy surface by verifying that the frequency calculation had no imaginary frequencies. If appropriate, exploration of molecular conformations was first done using lower-level theory in Spartan 08. [66]

3.3.4 Molecular Structure Results

The CCSD(T) calculations predict the ground state of CHO-CH₂OH to be the hydrogen bonded cyclic structure in Figure 3.1. The open-chain conformations are all more than 3 kcal mol⁻¹ higher in energy. The effective structure of glycolaldehyde has been determined previously by microwave spectroscopy [27, 86]. Figure 3.3 shows the results of CCSD(T) electronic structure calculations of the molecular geometry of CHO-CH₂OH; the electric dipole moments are in Debye and the experimental bond lengths (Å) are shown in parentheses. [27, 86] The purely ab initio structure is in good agreement with the microwave structure except for the OH bond length, which differs by approximately 0.1 Å, as noted by Carroll *et. al.* [27]. Given the excellent agreement between our calculations and the measured rotational constants for all isotopes and the dipole moment, we reinvestigated the microwave structure determination using the published data [19, 26, 27, 65] and our calculated vibrational corrections to the rotational constants. We find that the large discrepancy in the OH bond length between the earlier experimental determinations and theory is due to unusual zero-point contributions to the moments of inertia that are inferred from the rotational constants;

Glycolaldehyde
ab initio electronic structure
 AE-CCSD(T)/PCVQZ
 (experimental substitution structure)



Molecular Structure (Å) from:
J. Mol. Spectrosc. 2013, 284, 21-28

Figure 3.3: Molecular structures for 1A glycolaldehyde that result from CCSD(T) electronic structure calculations of the molecular geometry of CHO-CH₂OH. The values in parentheses are reported from earlier analysis of the microwave spectrum. [27]

when these are taken into account the discrepancy is largely (but not yet completely) resolved. It is important to be precise in terminology when discussing molecular structures because several inequivalent types exist. [58] Generally speaking, structures are obtained from microwave data by relating moments of inertia that are inferred from the rotational constants to the atomic positions. The most conceptually straightforward procedure is to obtain data on isotopic species and solve a least-squares problem relating the inferred moments of inertia to a (unique) structure, which yields an effective r_0 structure. Unfortunately, r_0 structures make a number of assumptions- for one, that the geometry of isotopically substituted species are identical after vibrational effects are included- and so the ultimate goal is to determine the isotope-independent 'vibrationless' r_e structure. The earlier experimental glycolaldehyde structures employed the substitution method, [32] where every atom is individually isotopically substituted to determine its position using the Kraitchman

equations, [76, 78] which permits- again, subject to approximations- their Cartesian coordinates in the principal axis system to be obtained. As discussed by Costain [32] the resulting r_s structure generally benefits from cancellation of zero-point vibrational effects and produces structures closer to r_e than the r_0 method, because usually $r_s \cong \frac{1}{2}(r_e + r_0)$.

However, the degree of agreement between r_s , r_e , and r_0 can vary, and the OH bond of glycolaldehyde appears to be a case where it does so significantly. The controlling factors in that relationship involve the ratios of the sum of the zero-point rotation-vibration corrections for each of the 18 fundamental modes ($\frac{1}{2}\Sigma\alpha$) and of the rotational constants between pairs of isotopes in the substitution method. [32, 58] These ratios are all contained within a range of about 15% for the single isotopic substitutions, except for the OH \rightarrow OD substitution where the zero-point rotation-vibration correction to the A rotational constant ($\frac{1}{2}\Sigma\alpha^A$) falls more than five times outside the usual variation. This extreme deviation appears to be caused primarily by α_1^A , the rotation-vibration correction associated with ν_1 , the OH stretch.

With the benefit of the *ab initio* vibrational corrections, we determine a semiexperimental restructure by correcting the experimental rotational constants for zero-point vibration and performing a least-squares optimization of the 12 structural parameters. The OH bond length we obtain is $0.9528 \pm 0.0005 \text{ \AA}$, which while clearly in closer agreement with theory than the r_s value, still seems too short by roughly 0.01 \AA . We also fit an r_0 structure where $R_{\text{OH}} = 1.041 \pm 0.006 \text{ \AA}$, in accordance with the previous r_s structures. We therefore conclude that zero-point vibrational effects are responsible for the previously noted discrepancy between theory and experiment (see the Supporting Information for details at the end of this chapter). Nevertheless, the unusual magnitude of the $r_0 - r_e$ shift and the short r_e OH bond length remain a curiosity, and further investigation is warranted.

3.4 Ionization Energy of Glycolaldehyde

The ionization energy of glycolaldehyde was previously measured by threshold electron impact ionization to be $\text{IE}(\text{CHO}-\text{CH}_2\text{OH}) \geq 10.2 \pm 0.1 \text{ eV}$ [120]. Tunable VUV radiation was used to confirm this value during the study of glycolaldehyde. Figure 3.4 shows the photoionization efficiency curve, $\text{PIE}(m/z \text{ 60})$, that results when glycolaldehyde ($\text{CHO}-\text{CH}_2\text{OH}$) in He is heated to 400 K.

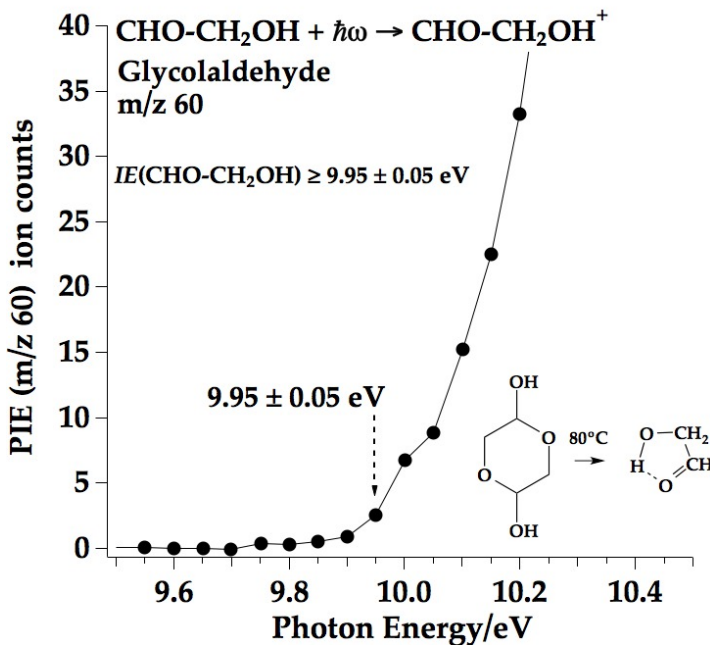
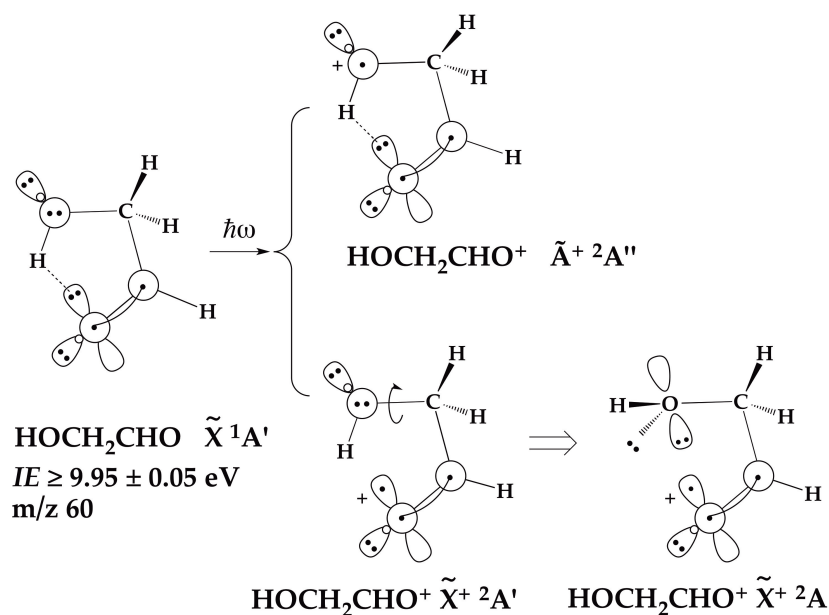


Figure 3.4: Photoionization efficiency scan for the parent ion m/z 60 resulting from heating glycolaldehyde in a continuous-flow He micro-reactor.

The appearance energy for CHO-CH₂OH⁺ (m/z 60) fixes a lower bound on the ionization energy of IE(CHO-CH₂OH) ≥ 9.95 ± 0.05 eV, a slightly lower value than electron impact results [120]. This is a lower value due to the fact that there may be some vibrational and rotational energy still in the molecule upon ionization, effectively lowering the ionization energy ever so slightly. The electronic states of the CHO-CH₂OH⁺ ion can be understood with generalized valence bond (GVB) diagrams [57], pictured on Scheme 3.1. Ionization at the carbonyl group produces a ²A' ion that relaxes to the nonplanar $\tilde{\chi}^+$ ²A⁺ cation. Photoionization of the carbohydrate produces the \tilde{A}^+ ²A⁺ excited state; this is expected to be roughly 0.5 eV above the ground state. The *ab initio* calculated ionization gives IE(CHO-CH₂OH) = 10.0 ± 0.2 eV and is consistent with the experimental spectrum in Figure 3.4. The ground state of the CHO-CH₂OH⁺ is found to be the nonsymmetric $\tilde{\chi}^+$ ²A state. The excited state, \tilde{A}^+ ²A" (CHO-CH₂OH⁺), is calculated to be 0.2 eV higher than the $\tilde{\chi}^+$ state.



Scheme 3.1: Generalized Valence Bond Diagrams for the Ground and Excited States of the $\text{CHO}-\text{CH}_2\text{OH}^+$ Cation

3.5 Results of Glycolaldehyde and Glyoxal Pyrolysis

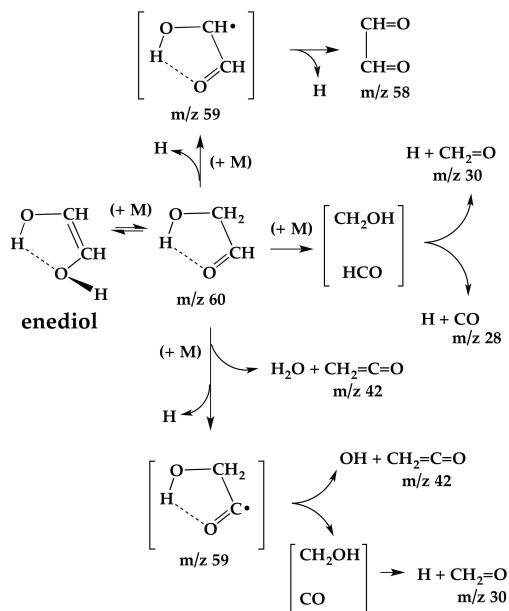
Pyrolysis pathways can be estimated by use of the known [14] heats of formation of the radicals and the measured $\Delta_f H_{298}(\text{CHO}-\text{CH}_2\text{OH})$. Table 3.1 is a gathering of most of the relevant energetics for thermal fragmentation of glycolaldehyde and glyoxal. Scheme 3.2 shows the likely thermal decomposition pathways of glycolaldehyde. Cleavage of the C-C bond requires 82 kcal mol^{-1} , and results in the very unstable radicals HCO and CH_2OH . These radicals will quickly decompose to H atom and CO, as well as H atom and $\text{CH}_2=\text{O}$, respectively. A fair estimate for cleavage of the $\text{HOCH}_2\text{CO}-\text{H}$ is 88 kcal mol^{-1} ; this leads to formation of the acyl radical, $\text{HOCH}_2\text{CO}\cdot$, and H atoms [14]. Rapid decomposition of the acyl radical yields (OH and $\text{CH}_2=\text{C}=\text{O}$) or (CO and CH_2OH). Finally, loss of the methylene C-H of glycolaldehyde generates H atom and the HOCHCHO radical. Thermal cracking of the HOCHCHO radical makes H atoms and glyoxal, $\text{HCO}-\text{CHO}$. This will proceed to cleave to two CHO radicals, ultimately forming CO and H atoms. It is also possible that glycolaldehyde could isomerize to the enediol ($\text{HOCH}=\text{CHOH}$), or that it goes through concerted reaction mechanisms, such as loss of water to form ketene. The unimolecular fragmentation pathways in Scheme 3.2 all produce H atoms. It is known [155] that hydrogen atoms

experimental thermochemistry, kcal mol ⁻¹				refs.
(1)	$\Delta H_{298}(\text{CH}_3-\text{CH}_3)$	90.2	± 0.1	14, 114
(2)	$\Delta H_{298}(\text{CH}_3-\text{CHO})$	83.8	± 0.2	14, 114
(3)	$\Delta H_{298}(\text{CH}_3-\text{CH}_2\text{OH})$	87.2	± 0.2	14, 114
(4)	$\Delta H_{298}(\text{trans-HCO-CHO})$	70.8	± 0.3	14, 48, 64, 114
(5)	$\Delta H_{298}(\text{CHO-CH}_2\text{OH})$	82	± 1	this work
(6)	$\Delta H_{298}(\text{H-CH}_2\text{CH}_3)$	101.1	± 0.4	14, 114
(7)	$\Delta H_{298}(\text{H-CH}_2\text{CHO})$	96.1	± 0.2	14, 114
(8)	$\Delta H_{298}(\text{CH}_3\text{CO-H})$	89.3	± 0.4	14, 114
(9)	$\Delta H_{298}(\text{H-CH}_2\text{CHO})$	94	± 2	14, 114
(10)	$\Delta H_{298}(\text{CH}_3-\text{CO})$	11.1	± 0.4	14, 114
(11)	$\Delta H_{298}(\text{H-CO})$	15.6	± 0.1	14, 114
(12)	$\Delta H_{298}(\text{CH}_2\text{O-H})$	30.2	± 0.2	14, 114

m/z	species	ionization energy		refs.
1	H	13.59844	± 0.00001	98
17	OH	13.01698	± 0.00025	165
28	CO	14.0136	± 0.0005	44
30	CH ₂ =O	10.8850	± 0.0002	130
32	O ₂	12.0696	± 0.0002	146
42	CH ₂ =C=O	9.6191	± 0.0004	107
44	CH ₂ =CHOH	≥ 9.33	± 0.05	142
44	CH ₃ CHO	10.2295	± 0.0007	74
58	HCO-CHO	10.2	± 0.1	23
60	CHO-CH ₂ OH	≥ 9.95	± 0.05	this work

Table 3.1: Thermochemistry and Ionization Energy of Important Organics

Glycolaldehyde: Unimolecular Decomposition



Scheme 3.2: Unimolecular Decomposition of Glycolaldehyde

are very reactive in these hot microreactors. Scheme 3.3 shows the likely products that result from H atom chemistry with glycolaldehyde. The H atoms could add to the carbonyl C atom to produce the HOCH₂CH₂O radical. This alkoxy radical is expected to rapidly fragment to CH₂OH and CH₂=O. Alternatively, H atoms could add to the carbonyl O atom and generate the HOCH₂CHOH radical. Loss of OH leads to the enol, CH₂=CHOH. Isomerization of the enol produces CH₃CHO, which fragments [154, 156] in the hot microreactor. As stated in Chapter 1, fuel samples are kept purposefully dilute in order to avoid such reactions as those listed in Scheme 3.3. It has been shown that fuel mixtures of approximately 0.1% or less can lead to the suppression of the most expedient bimolecular chemistry- H atoms reactions. In the case of glycolaldehyde, control over this dilution is difficult due to the high boiling point and dimeric form of the species at room temperature. It was possible, however, to turn the sample temperature up slowly until sufficient, but not too much, signal was observed.

Figure 3.5 shows the 118.2 nm (10.487 eV) PIMS that results when glycolaldehyde is heated to 1400 K. The bottom scan is from a sample of the glycolaldehyde dimer heated to 80 °C. The inset at the top reveals that there are no signals from the (dimer glycolaldehyde)⁺ at *m/z* 120, which implies that this species does not survive in the beam. The spectrum shows an intense peak at

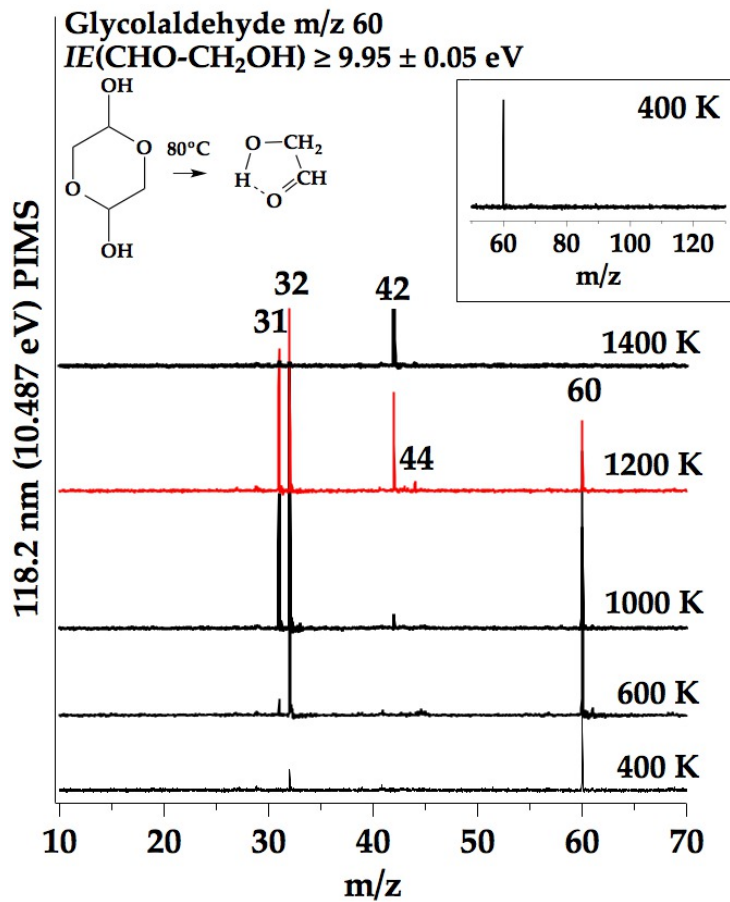
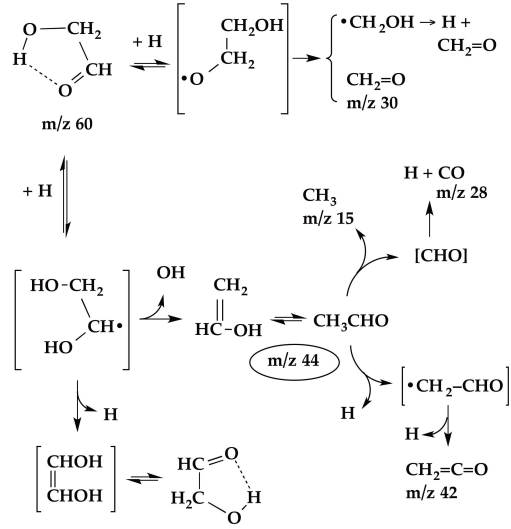


Figure 3.5: 118.2 nm VUV PIMS scans resulting from heating glycolaldehyde in a pulsed He micro-reactor.

H Atom/Glycolaldehyde Chemistry



Scheme 3.3: Potential H Atom Chemistry

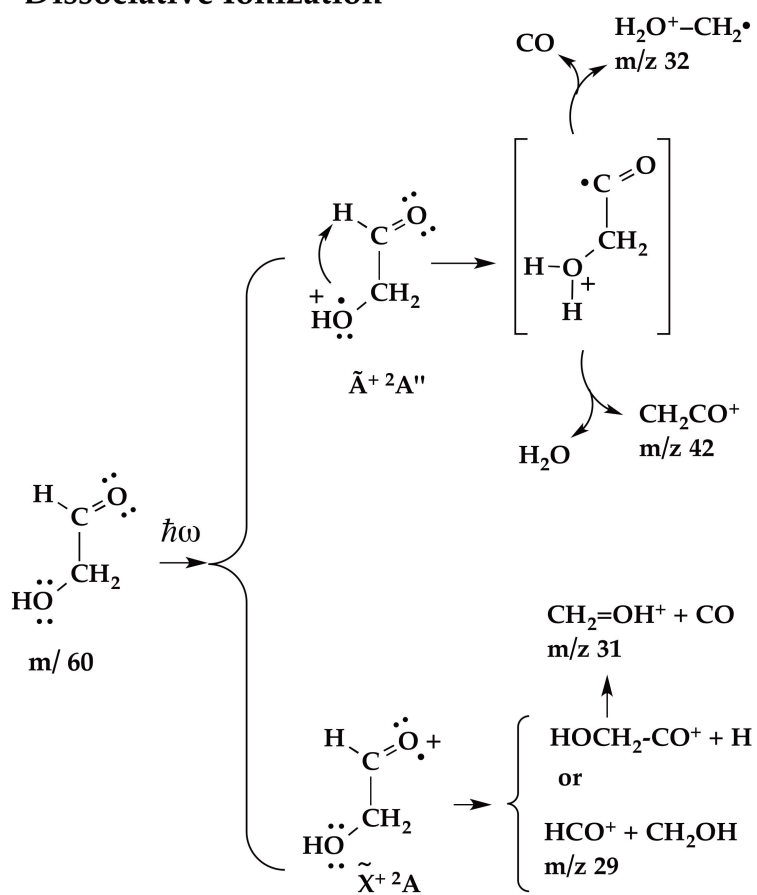
m/z 60 that is assigned to $\text{CHO}-\text{CH}_2\text{OH}^+$; this is consistent with the ionization threshold of 9.95 ± 0.05 in Figure 3.4. The presence of the feature at m/z 32 demonstrates that $\text{CHO}-\text{CH}_2\text{OH}$ is subject to dissociative ionization.



Scheme 3.4 suggests dissociation pathways for the glycolaldehyde cation. The ground $\tilde{\chi}^+ \text{}^2\text{A}$ state of the $\text{CHO}-\text{CH}_2\text{OH}^+$ cation is subject to β -scission that could produce one of the stable ions HCO^+ (m/z 29) or $\text{CH}_2=\text{OH}^+$ (m/z 31). Ionization of the alcohol produces the excited state $\tilde{\text{A}}^+ \text{}^2\text{A}''$, which could internally abstract at the acyl group and generate the metastable $[\text{H}_2\text{O}-\text{CH}_2-\text{CO}\cdot]^+$ distonic ion. Loss of water leads to the ketene radical-cation, CH_2CO^+ (m/z 42), or loss of CO generates the $[\text{H}_2\text{O}-\text{CH}_2\cdot]^+$ (m/z 32) distonic cation. It is worth noting that in an earlier photoionization study, [132] dissociative ionization of glycolaldehyde with loss of CO to produce m/z 32 was observed. Due to the fact that splitting between the $\tilde{\chi}^+ \text{}^2\text{A}$ and $\tilde{\text{A}}^+ \text{}^2\text{A}''$ states of the $\text{CHO}-\text{CH}_2\text{OH}^+$ is about 240 meV, the 118.2 nm (10.487 eV) ionizing laser will produce both low-lying states of the $\text{CHO}-\text{CH}_2\text{OH}^+$ cation. On the basis of these energetics and Scheme 3.4, we assign the dissociative ion m/z 32 in Figure 3.5 to be the $[\text{H}_2\text{O}-\text{CH}_2\cdot]^+$ distonic cation. As the micro-reactor is heated to

Glycolaldehyde

Dissociative Ionization



Scheme 3.4: Dissociative Ionization Pathways

600 K a peak at m/z 31 appears (Figure 3.5). A possible explanation could be isomerization of CHO-CH₂OH to the enediol, HOCH=CHOH. Ionization energies of enols are roughly 1 eV below the keto tautomer, so IE(HOCH=CHOH) is likely approximately 9 eV [118]. Photoionization of the enediol produces the [HOCH=CHOH]⁺ cation, which is subject to rearrangement [90] to the $\tilde{\chi}^+$ ²A [CHO-CH₂OH]⁺ ion that is chemically activated by about 1.5 eV. In Figure 3.5 we assign the feature at m/z 31 to the CH₂=OH⁺ ion. As the reactor is heated to 1000 K, a peak at m/z 42 is observed and is assigned to CH₂CO⁺. This could be due to dissociative ionization of the enediol or ketene as a thermal product. At 1200 K, m/z 42 becomes much more intense.

It is difficult to say if there is any H atom chemistry as described in Scheme 3.3. Addition of H atoms to O atoms could lead to production of OH radicals and the enol, CH₂=CHOH. There are weak signals at m/z 44 when CHO-CH₂OH is heated to 1200 K. These signals probably arise from small amounts of CH₂=CHOH but are unlikely to originate from CH₃CHO. Acetaldehyde is known [154,156] to thermally dissociate to CH₃ and HCO radicals, but no methyl radicals (m/z 15) are ever detected. Any hydroxyl radicals that result from the H atom chemistry in Scheme 3.3 would form water by reaction with parent glycolaldehyde. [137]

One way to avoid the confusing PIMS signals that result from dissociative ionization is to use IR spectroscopy as a diagnostic of the pyrolysis products. The IR spectrum of CHO-CH₂OH has been studied in the gas phase [94] and in matrices. [28]CCSD(T)/VPT2 calculations were performed for the fundamental vibrational modes of glycolaldehyde. Table 3.2 compares the *ab initio* frequencies with the experimental findings [28,94] and the transitions observed in an Ar matrix. Figure 3.6 shows the IR spectrum that results when glycolaldehyde is heated to 1500 K. The presence of formaldehyde is clearly demonstrated [135] by observation of ν_1 (CH₂=O), ν_2 (CH₂=O), and ν_3 (CH₂=O). The six modes of formaldehyde as observed in an Ar matrix are: ν_1 (a₁, CH₂ sym st) = 2798 cm⁻¹, ν_2 (a₁, CO st) = 1742 cm⁻¹, ν_3 (a₁, CH₂ scis) = 1499 cm⁻¹, ν_4 (b₁, CH₂ umbrella) = 1169 cm⁻¹, ν_5 (b₂, CH₂ a-st) = 2864 cm⁻¹, ν_6 (b₂, CH₂ rock) = 1245 cm⁻¹. Glyoxal [135] is identified as a thermal product by observation of ν_{10} (HCO-CHO). Scheme 3.2 has a possible path for glyoxal formation; however, the thermochemistry in Table 3.1 shows $\Delta_f H_{298}$ (HCO-CHO) to be 71 kcal mol⁻¹. Because of the relatively low HCO-CHO bond energy, we expect (Table 3.1) that most glyoxal will dissociate to a pair of HCO radicals, which in turn fragment to H atoms and CO. Additional concerted reactions have been shown to predominate at lower temperatures; [50]

mode	CCSD(T)/ VPT2	A (km/mol)	gas phase [94]	Ar matrix this work ^a	relative intensity	
A'	ν_1	3557	39	3585/3565/3546	3551/3543/3535	10/25/23
	ν_2	2923*	10	2920	2911/2906/2895	2/2/3
	ν_3	2813/2842*	33/11	2835/2810	2853/2846/2835	5/6/2
	ν_4	1751/1692	83/11	1764/1753/1742	1767/1747/1697/ 1695	3/186/18/ 9
	ν_5	1454/1429	7/16	1440/1468	1443/1429/1424	4/5/4
	ν_6	1404*	30	1410	1402	5
	ν_7	1366	14	1376/1359	1366/1365/1361	42/19/5
	ν_8	1284/1272*	11/21	1299/1282/1273/ 1268/1266/1258	1272/1268/1266	6/25/19
	ν_9	1112*	61	1117/1112/1110/ 1097	1131/1112/1110/ 1108	6/12/100/ 45
	ν_{10}	853	43	871/861/859/845	860/858/857/ 856/855	7/18/12/ 68/29
	ν_{11}	745	8	762/752/750/748/ 746/743/738	751/749	7/7
	A''	ν_{12}	280	23		
ν_{13}		2873*	25	2880	2880*	1
ν_{14}		1223*	2	1146	1251/1232/1228	2
ν_{15}		1083	1	1070/1059/1050	1067	6
ν_{16}		709	0			
ν_{17}		340	83			
ν_{18}		200	6			
$2\nu_7$		2715	3	1717/1696	2713/1711	5/3
[ν_{12}, ν_{18}] + [ν_{11}, ν_{16}]			916	999/997/951/935	5/4/3/2	

Table 3.2: Vibrational Frequencies and Assignments for Glycolaldehyde

^aThe VPT2 calculations use CCSD(T)/ANO0 anharmonic constants and CCSD(T)/ANO1 harmonic frequencies. Asterisks mark cases where resonances were treated by diagonalization. Potential combination/overtone bands for unidentified observed peaks have also been reported. All Ar matrix frequencies reported to $\pm 0.3 \text{ cm}^{-1}$

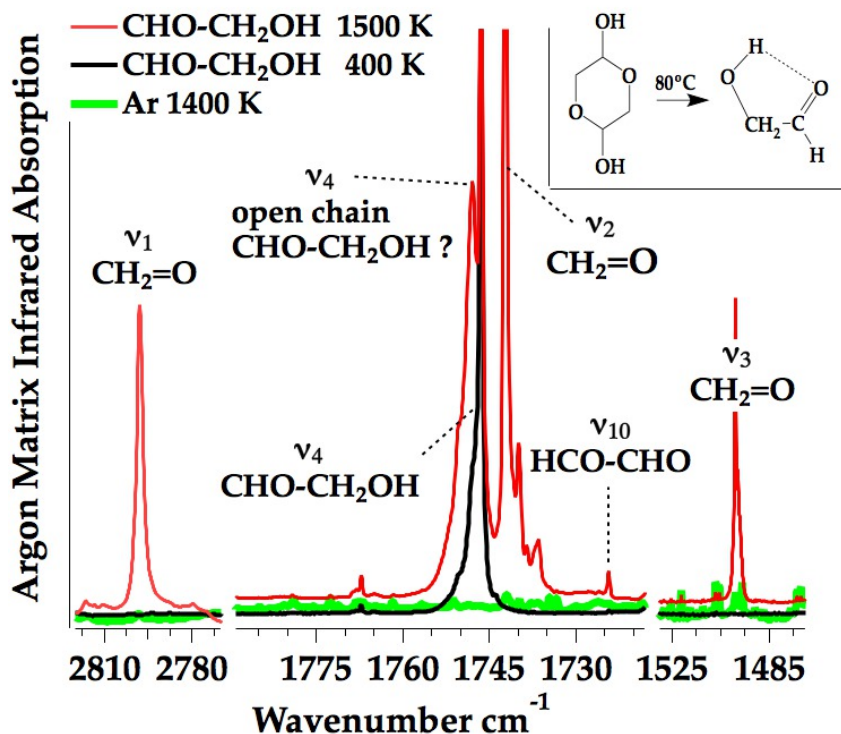


Figure 3.6: Matrix IR spectra that result from heating glycolaldehyde in a pulsed Ar micro-reactor. The black trace is the IR spectrum [135] of CHO-CH₂OH produced by heating glycolaldehyde dimer to 80 °C. The green trace is a background that results from heating Ar to 1500 K in the SiC micro-reactor. Both formaldehyde [135] and glyoxal [42,135] are present.

however, little evidence is seen of this under our conditions at 1500 K in the Fourier transform IR. There is a new >C=O band appearing to the blue of ν_4 (CHO-CH₂OH), which is assigned to an open-chain conformer of glycolaldehyde in Figure 3.1. An additional peak at 1737 cm⁻¹ is observed and attributed to ν_2 of the (CH₂=O, H₂O) dimer. [104]The unassigned peak at 1767 cm⁻¹ observed at 300 and 1500 K is perhaps due to a similar interaction between water and glycolaldehyde. Additionally, Figure 3.7 establishes the presence of ketene [55] as a thermal product with detection of ν_7 (CH₂=C=O), ν_2 (CH₂=C=O), and ν_3 (CH₂=C=O). To confirm the pyrolysis of glyoxal HCO-CHO (+M) \longrightarrow [HCO + HCO] \longrightarrow 2 H + 2 CO, an authentic sample of HCO-CHO was decomposed in a hot SiC reactor (see Figure 3.6). The IE(HCO-CHO) is reported [23] to be 10.2 eV (Table 3.1). Figure 3.8 shows the PIMS of a dilute mixture of glyoxal in He is vaporized in a micro-reactor at 120 °C (400 K), and the parent peak (m/z 58) is the dominant feature in the spectrum. As the reactor is heated to 1200 K, the [HCO-CHO]⁺ m/z 58 signal begins to drop. By

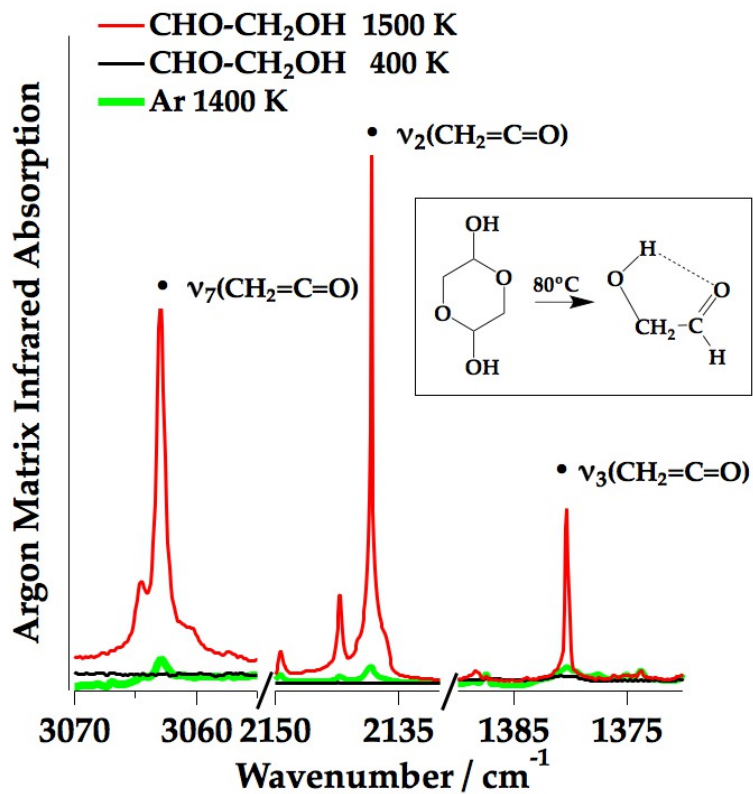


Figure 3.7: Matrix IR spectra that result from heating glycolaldehyde in a pulsed Ar micro-reactor. The black trace is the IR spectrum [135] of CHO-CH₂OH produced by heating glycolaldehyde dimer to 80 °C. The green trace is a background that results from heating Ar to 1500 K in the SiC micro-reactor. Ketene is clearly present. [55]

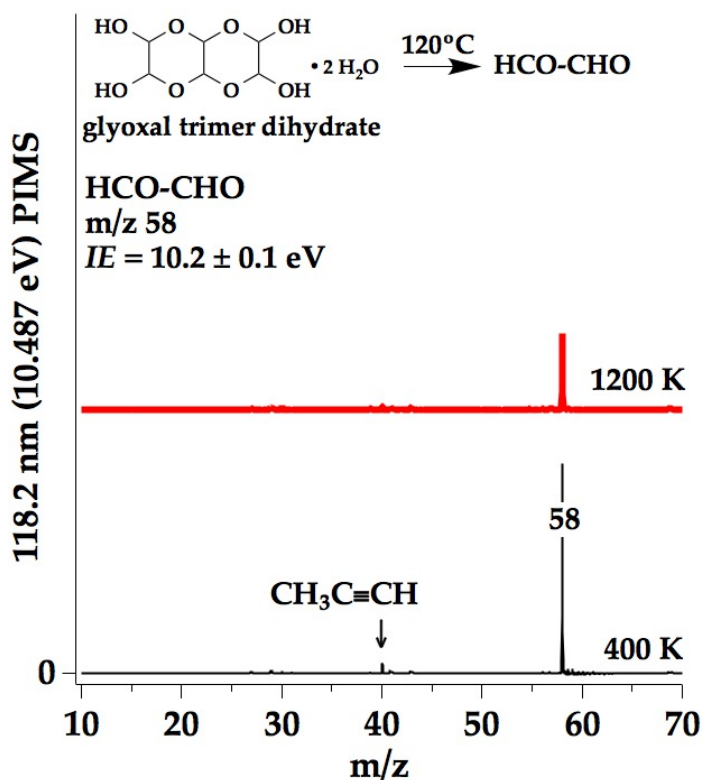


Figure 3.8: 118.2 nm VUV PIMS scans resulting from heating glyoxal in a pulsed He micro-reactor. The band at m/z 40 is a propyne background contamination.

1400 K in He, all signals fade from the 118.2 nm PIMS spectrum, because the pyrolysis products of glyoxal, H, and CO in eq 3.10, cannot be photoionized by 10.487 eV radiation (see Table 3.1). Figure 3.9 shows the IR spectra that result from heating glyoxal in Ar [42,135]. By 1500 K, the HCO-CHO is largely destroyed, and intense signals of CO are observed. Figure 3.9 shows the appearance of clusters of carbon monoxide [81] that result from the pyrolysis of glyoxal. We do not observe any formaldehyde that would arise from the previously observed glyoxal molecular decomposition channels [50].

3.6 Conclusions

Pyrolysis of CHO-CH₂OH in the heated micro-reactor was shown to produce H atoms, formaldehyde, glyoxal, and carbon monoxide. Scheme 3.2 provides the unimolecular chemistry that leads to these results. Formaldehyde was shown to have intense IR absorption signal, consistent with

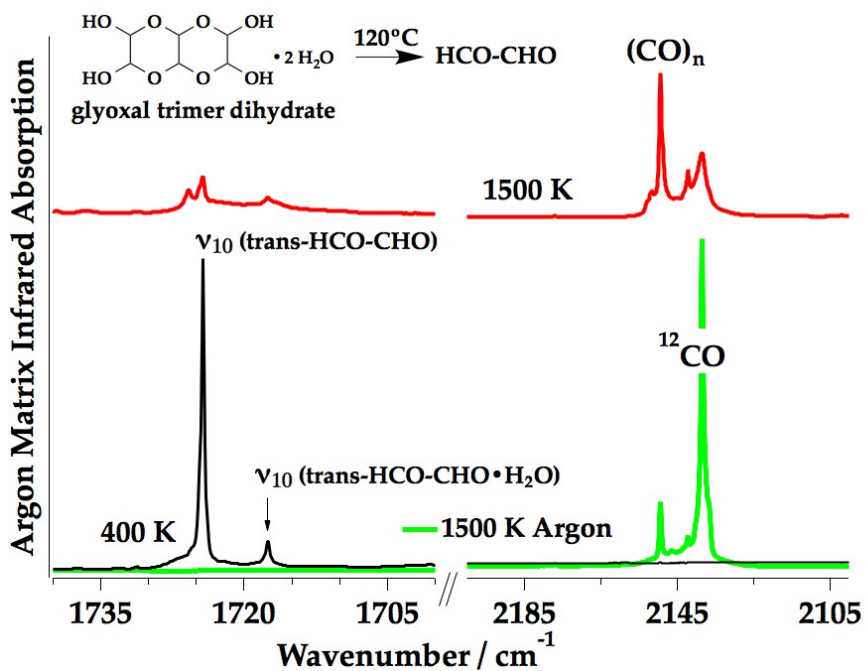


Figure 3.9: Matrix IR spectra that result from heating glyoxal trimer dihydrate in a pulsed Ar micro-reactor. The black trace is the IR spectrum [42, 135] of HCO-CHO produced by heating glyoxal to 120 °C. The intense glyoxal fundamental ν_{10} is detected at 1724 cm⁻¹, and the (water, glyoxal) complex [100] is observed at 1717 cm⁻¹. The green trace is a background that results from heating Ar to 1500 K in the SiC micro-reactor.

cleavage of the CHO–CH₂OH C-C bond to make HCO and CH₂OH. This ultimately results in the products H atoms, CO, and formaldehyde (CH₂=O), see Figure 3.6. Cleavage of the C-H methylene bond in glycolaldehyde leads to the formation of HCO-CHO and H atoms. Lastly, loss of H atom to form ·CO–CH₂OH radicals generated CH₂=O and ketene, CH₂=C=O (Figure 3.7). Pyrolysis of glyoxal independently was shown to decompose to a pair of formyl radicals that fragment to H atom and CO, see Figure 3.9.

The molecular properties of glycolaldehyde are not well established, therefore both the gas-phase heat of formation and ionization threshold for CHO–CH₂OH have been measured and reported here. The $\Delta_f H_{298}(\text{CHO}-\text{CH}_2\text{OH})$ was determined by a combination of calorimetric measurements and *ab initio* electronic structure calculations. Calorimetric studies of the heat of reduction of glycolaldehyde in solution lead to a determination of the heat of formation of solid glycolaldehyde dimer to be -191.1 ± 0.4 kcal mol⁻¹. Measurement of $\Delta H_{(\text{fusion})}$ and $\Delta H_{(\text{vap})}$ results in a value of the gas-phase heat of formation for glycolaldehyde, $\Delta_f H_{298}(\text{CHO}-\text{CH}_2\text{OH})$, as -75.8 ± 1.3 kcal mol⁻¹. Electronic structure calculations predict values for the heat of formation of glycolaldehyde that agree well with the experimental determination. The $\Delta_f H_{298}(\text{glycolaldehyde})$ calculated by the CBS-APNO method is -76 ± 1 kcal mol⁻¹. More precise, fully *ab initio* calculations using the modified HEAT protocol [106] predict $\Delta_f H_0(\text{CHO}-\text{CH}_2\text{OH})$ of -73.1 ± 0.5 kcal mol⁻¹ and $\Delta_f H_{298}(\text{CHO}-\text{CH}_2\text{OH})$ of -76.1 ± 0.5 kcal mol⁻¹. The electronic structure calculations, both CBS-APNO and modified HEAT, of the heat of formation for glycolaldehyde are in excellent agreement with the calorimetrically determined result of -75.8 ± 1.3 kcal mol⁻¹.

Tunable synchrotron radiation was used to place a lower bound on the IE(CHO–CH₂OH), see Figure 3.4. The appearance energy of [CHO–CH₂OH]⁺ gives an ionization threshold of $\geq 9.95 \pm 0.05$ eV, consistent with *ab initio* electronic structure calculations. Coupled cluster calculations provide an ionization of glycolaldehyde of 10.0 ± 0.2 eV, also in agreement with Fig. 3.4. Coupled cluster calculations were also used to analyze the molecular structure of glycolaldehyde and to revise the geometry of this carbohydrate. It was found that equilibrium O-H bond length is considerably shorter than suggested by experimental determinations of the effective r_0 structure on account of unusual zero-point contributions, primarily from the ν_1 OH stretch. These successful efforts to understand the thermal cracking and the molecular properties of both glyoxal and glycolaldehyde are encourages for prospective future work on complex sugars.

3.7 Supporting Information

1. Analysis of the Rotational Spectra of Glycolaldehyde:

Table 3.3: *ab initio* geometry

Table 3.4: *ab initio* rotation-vibration corrections

Table 3.5: Fitted geometries

N.B. Bond lengths in angstroms, angles in degrees, and rotational constants in MHz.

H							
O	1	ROH					
C	2	RCO1	1	A1			
C	3	RCC	2	A2	1	D0	
O	4	RCO2	3	A3	2	D0	
H	4	RCH1	3	A4	2	D180	
H	3	RCH2	2	A5	1	D1	
H	3	RCH2	2	A5	1	M1	

Table 3.3: AE-CCSD(T)/cc-pCVQZ structure

ROH = 0.965391271210242
 RCO1 = 1.395710672083639
 A1 = 105.753645518439939
 RCC = 1.502495632823179
 A2 = 111.706140011703965
 D0 = 0.0000000000000000
 RCO2 = 1.208231709793324
 A3 = 121.678324959015256
 RCH1 = 1.101128822154100
 A4 = 116.807970666716855
 D180 = 180.0000000000000000
 RCH2 = 1.095901092506787
 A5 = 111.242081800699253
 D1 = 120.511546584198925
 M1 = -120.511546584198925

Isotope	Vibrational Correction		
	A	B	C
1,16,12,12,16,1,1,1	44.1062837	117.065605	70.212949
1,18,12,12,16,1,1,1	37.9721156	112.06835	67.5807516
1,16,12,12,18,1,1,1	46.4355946	110.44761	67.2840051
1,16,12,13,16,1,1,1	40.3002581	115.658899	69.0447772
1,16,13,12,16,1,1,1	41.1012071	115.030514	68.5492881
1,16,12,12,16,2,1,1	47.844386	109.963985	64.736091
2,16,12,12,16,1,1,1	70.5600479	106.032532	64.0509815
1,16,12,12,16,1,2,1	46.0516933	112.761627	67.5965934
1,16,12,12,16,2,2,1	47.3267	106.384917	62.4941155

Table 3.4: *ab initio* FC-CCSD(T)/ANO1 rotation-vibration corrections

2. Reaction Calorimetry:

glycolaldehyde dimer (solid) \longrightarrow LiOCH₂CH₂OLI (sol'n)

-81,547.63 cal mol⁻¹

-82,442.11

-81,799.66

-82,364.13

-81,918.43

Parameter	r_e	sigma	r_0	sigma
ROH	0.952800866	0.000478	1.041482542	0.005715
RCO1	1.395726851	0.000168	1.401515053	0.001729
A1	106.6417314	0.032566	103.0005211	0.323204
RCC	1.50047276	0.000455	1.515369575	0.00459
A2	111.6847713	0.011435	112.5189181	0.114378
RCO2	1.208857832	0.000182	1.206968033	0.001808
A3	121.6669118	0.017788	121.2340232	0.179259
RCH1	1.101185371	0.000201	1.097162492	0.001996
A4	116.9073292	0.016353	116.1094319	0.166428
RCH2	1.096382033	0.000117	1.102252899	0.001191
A5	111.0475377	0.018287	110.6662866	0.186303
D1	120.6508306	0.026825	121.1848036	0.265543
M1	-120.6508306	0.026825	-121.1848036	0.265543

r_e : RMS error: 0.01 MHz / Maximum error: 0.22 MHz

r_0 : RMS error: 0.14 MHz / Maximum error: 2.13 MHz

Table 3.5: Fitted geometries

ave: $-82,014 \pm 340$ cal mol⁻¹, molecular weight = 120.10

ethylene glycol(liquid) \longrightarrow LiOCH₂CH₂OLi (sol'n)

-27,842.07

-27,926.37

-27,889.04

-27,732.76

ave: $-27,847.56 \pm 84$ cal mol⁻¹

Differential Scanning Calorimetry

glycolaldehyde, solid dimer \longrightarrow 2 glycolaldehyde, liquid monomer

28.43 kJ mol⁻¹

27.34

27.44

ave: 27.74 ± 0.70 kJ mol⁻¹ = 6.63 ± 0.17 kcal mol⁻¹, molecular weight 120.10

at $T_{\text{mid}} = 85 \pm 3^\circ\text{C} = 358.15 \pm 3 \text{ K}$

$$\begin{aligned}\text{Correction: } \Delta H_{\text{fus}, 298.15} &= \Delta H_{\text{fus}, \text{uncorrected}} + (298.15 - T_{\text{mid}})(2Cp_{(l)} - Cp_{(s)}) \\ &= 6.6 \text{ kcal mol}^{-1} + (298.15 - 358.15)(2 \cdot 30.62 \text{ cal mol}^{-1} \text{ K}^{-1} - 33.2 \text{ cal mol}^{-1} \text{ K}^{-1}) \\ &= 6.6 \text{ kcal mol}^{-1} - 1.7 \text{ kcal mol}^{-1} = 4.9 \text{ kcal mol}^{-1}\end{aligned}$$

$$Cp_{(l)} = 10.7 (\text{OH}) + 7.26 (\text{CH}_2) + 12.66 (\text{CHO}) = 30.62 \text{ cal mol}^{-1} \text{ K}^{-1}$$

$$\begin{aligned}Cp_{(s)} &= 2 \cdot (23.5 (\text{OH}) + 11.7 (\text{CH}) + 24.6 (\text{CH}_2) + 9.7 (\text{O})) = 139.0 \text{ J mol}^{-1} \text{ K}^{-1} \\ &= 33.2 \text{ cal mol}^{-1} \text{ K}^{-1}\end{aligned}$$

Heats of Vaporization using data from [115]

Clausius-Clapeyron analysis ($\ln P(\text{mmHg})$ vs $1/T(\text{K})$) where slope = $-\Delta H_{\text{vap}}/R$ at T_{mid}

$$\text{Correction: } \Delta H_{\text{vap}, 298.15} = \Delta H_{\text{vap}, T_{\text{mid}}} + (298.15 - T_{\text{mid}})(Cp_{(g)} - Cp_{(l)})$$

ethylene glycol: $y = -7433.5x + 22.602$ $r^2 = 0.999$, $T_{\text{mid}} = 346.1 \text{ K}$

$$\Delta H_{\text{vap}, 346.1} = 14.7 \text{ kcal}^{-1}$$

$$\Delta H_{\text{vap}, 298.15} = \Delta H_{\text{vap}, T_{\text{mid}}} + (298.15 - T_{\text{mid}})(Cp_{(g)} - Cp_{(l)})$$

$Cp_{(g)}$: experiment (NIST Webbook) $18.64 \text{ cal mol}^{-1} \text{ K}^{-1}$

$$\text{CBS-APNO calculation: } Cp = Cv + R = 15.67 + 1.987 = 17.7 \text{ cal mol}^{-1} \text{ K}^{-1}$$

$Cp_{(l)}$: experiment (NIST Webbook) $35.8 \text{ cal mol}^{-1} \text{ K}^{-1}$

$$\text{additivity: } 2 \cdot (10.7 (\text{OH}) + 7.26 (\text{CH}_2)) = 35.9 \text{ cal mol}^{-1} \text{ K}^{-1}$$

Using experimental data:

$$\begin{aligned}\Delta H_{\text{vap}, 298.15} &= 14.8 \text{ kcal mol}^{-1} + (298.15 - 346.1)(18.64 - 35.8) \\ &= 14.8 \text{ kcal mol}^{-1} + (-47.95 \text{ K})(-17.16 \text{ cal mol}^{-1} \text{ K}^{-1}) = 15.6 \text{ kcal mol}^{-1}\end{aligned}$$

Using additivity and calculated data:

$$\begin{aligned}\Delta H_{\text{vap}, 298.15} &= 14.8 \text{ kcal mol}^{-1} + (298.15 - 346.1)(17.7 - 35.9) \\ &= 14.8 \text{ kcal mol}^{-1} + (-47.95\text{K})(-18.2 \text{ cal mol}^{-1} \text{ K}^{-1}) = 15.7 \text{ kcal mol}^{-1}\end{aligned}$$

NIST Webbook: average of 13 values: 15.6 kcal mol⁻¹

glycolaldehyde: $y = -8523.5x + 25.246$ $r^2 = 0.9995$, $T_{\text{mid}} = 325.9\text{K}$

$$\Delta H_{\text{vap}, 325.9} 16.9 \text{ kcal mol}^{-1}$$

$$\Delta H_{\text{vap}, 298.15} = \Delta H_{\text{vap}, T_{\text{mid}}} + (298.15 - T_{\text{mid}})(C_{p(g)} - C_{p(l)})$$

$C_{p(g)}$: CBS-APNO calculation: $C_p = C_v + R = 13.6 + 1.987 = 15.6 \text{ cal mol}^{-1} \text{ K}^{-1}$

$C_{p(l)}$: $10.7 \text{ (OH)} + 7.26 \text{ (CH}_2\text{)} + 12.66 \text{ (CHO)} = 30.62 \text{ cal mol}^{-1} \text{ K}^{-1}$

$$\Delta H_{\text{vap}, 298.15} = 16.9 + (298.15 - 325.9\text{K})(15.6 - 30.62 \text{ cal mol}^{-1} \text{ K}^{-1}) = 17.3 \text{ kcal mol}^{-1}$$

Chapter 4

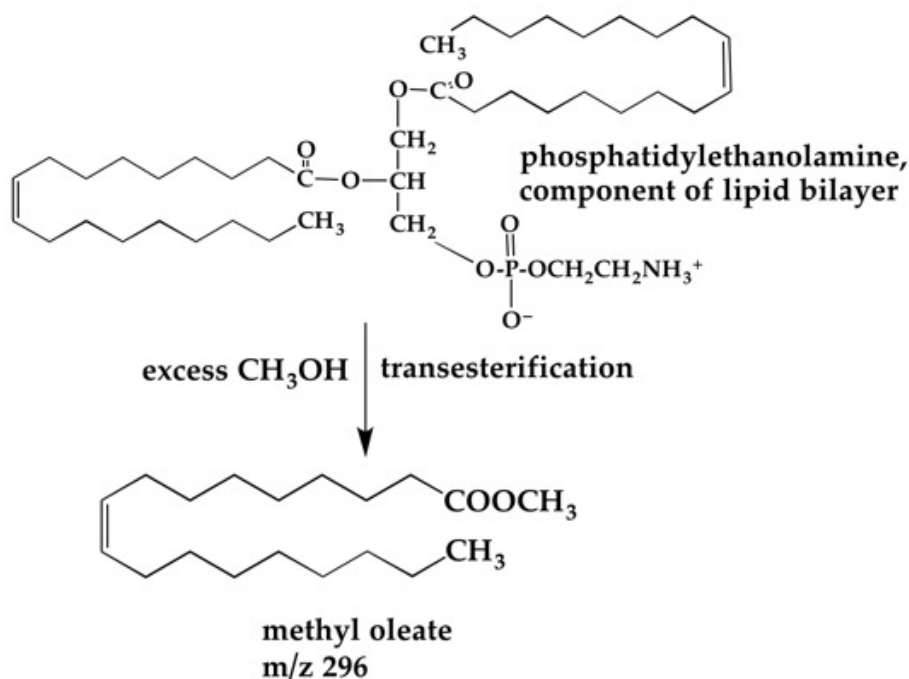
Methyl Esters

4.1 Introduction

This paper is an experimental study of the pyrolysis of two simple methyl esters: methyl acetate and methyl butanoate. Methyl esters are believed to have similar combustion properties to petroleum based fuels [121,160], making them a promising source of biofuels. These biofuels are derived from triglyceride esters of fatty acids found in the membranes of biological species, see Scheme 4.1. Transesterification of these triglycerides with methanol results in the formation of methyl esters of fatty acids, such as such as methyl oleate $\text{CH}_3(\text{CH}_2)_7\text{CH}=\text{CH}(\text{CH}_2)_7\text{COOCH}_3$. Long chain fatty acid esters are complex to study, so many have chosen the simpler compounds methyl acetate ($\text{CH}_3\text{COOCH}_3$) and methyl butanoate ($\text{CH}_3\text{CH}_2\text{CH}_2\text{COOCH}_3$) for scrutiny as surrogate fuels.

An accurate model for the unimolecular decomposition of these fuels is an important first step in the development of mechanisms for larger esters [47,68]. Methyl esters have been studied extensively, with experiments dating back to as early as 1936 [13]. The pyrolysis of methyl acetate has been studied in shock tubes [4,45,116,123,140], in a knudsen reactor [25], and in a flow reactor [167]. There have also been a number of computational studies [3,144,150]. Methyl butanoate has been rigorously studied computationally, as the chain length of methyl butanoate seems to be the proper length to reconcile computational size limits and carbon chain fatty acid characteristics [3,31,41,47,59,60,68,80,82,145]. The pyrolysis of methyl butanoate has been studied experimentally only by shock tube [45,46,112]. In addition to the pyrolysis experiments, there have been many studies of the oxidation of these methyl esters [31,37,40,52,53,79,93,111,113,128,131,158,161,171,177].

Biomembranes a Source of Esters of Fatty Acids



Scheme 4.1: Transesterification of triglycerides in methanol produces long chain fatty acid methyl esters. Oleic acid is shown here, a methyl ester derived from transesterification of phosphatidylethanolamine [101].

In the present study, we focus on the dilute (0.06 - 0.13%), unimolecular thermal decomposition of methyl esters in the heated micro-reactor described below.

4.2 Experimental

For the study of methyl acetate and methyl butanoate, experiments were conducted solely at the University of Colorado. Photoionization mass spectrometry at 10 Hz and 10.487 eV is used in tandem with matrix isolation infrared spectroscopy, see Chapter 1 for experimental details. Mass spectra are averaged over 1000 scans, with a mass resolution $\Delta m/m = 400$. Infrared spectra are averaged over 500 scans with a 0.25 cm^{-1} step size.

4.3 Plausible Decomposition Pathways

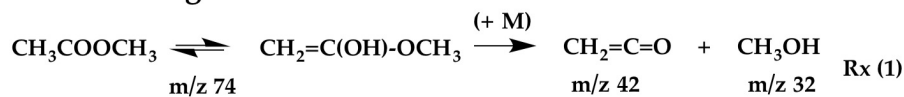
4.3.1 Methyl Acetate

The thermochemistry of ester decomposition is collected in Tables 4.1 and 4.2. Some of these entries are experimental values but most result from electronic structure calculations. This is due to the fact that the $\Delta_f H_{298}(\text{CH}_3\text{CH}_2\text{CH}_2\text{COOCH}_3)$ has not been measured. There is another complication that is peculiar to methyl esters, RCOOCH_3 [45, 56, 68, 89]. Step-wise cleavage to produce the methyl radical or the alkyl radical leads to production of the oxycarbonyl radical, $\text{RCO}_2\cdot$, or the acyl radical, $\cdot\text{COOCH}_3$. Neither of these species are stable molecules. The properties of the formoxy radical have been explored by negative ion chemistry and spectroscopy of the formate anion, $\text{HCO}_2\cdot$, but the $\text{HCO}_2\cdot$ radical decomposes to CO_2 and H atom. If the $\cdot\text{COOCH}_3$ and $\text{RCO}_2\cdot$ radicals are not stable species, the calculations of the bond energies $\text{R}-\text{COOCH}_3$ and $\text{RCOO}-\text{CH}_3$ will be approximate. For methyl acetate, one could imagine fragmentation *via* three different pathways, see Reactions (1) - (3) on Scheme 4.2. It is difficult to calculate the energetics of reactions (1-3). The only thing that is certain is $\Delta_{rxn} H_{298}(\text{CH}_3\text{COOCH}_3 \rightarrow 2 \text{CH}_3 + \text{CO}_2) = 74.9 \pm 0.3 \text{ kcal mol}^{-1}$.

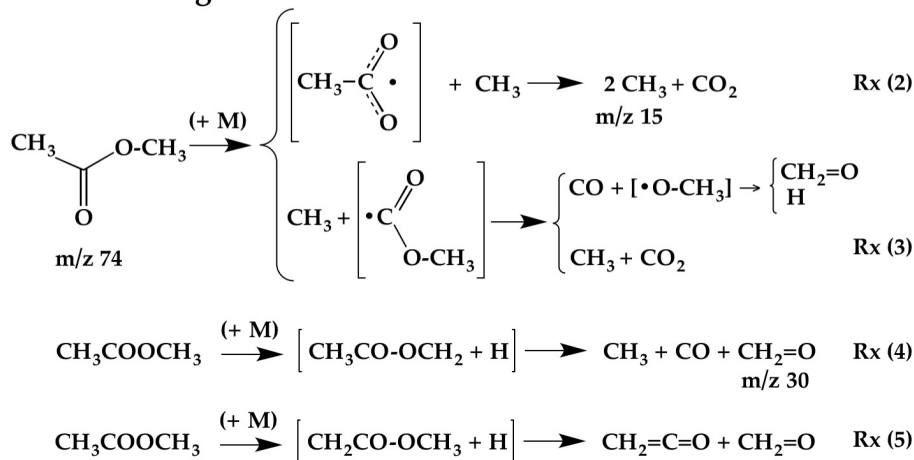
Reaction (4.1) in Scheme 4.2 is a 1,4 Woodward-Hoffman forbidden elimination, however it has the lowest calculated energetic barrier (see Tables 4.1 and 4.2) to produce ketene ($\text{CH}_2=\text{C}=\text{O}$) and methanol (CH_3OH). In Reaction (4.2), cleavage of the weak methoxy $\text{O}-\text{CH}_3$ bond results in loss of methyl radical CH_3 to form the acetoxy radical [$\text{CH}_3\text{CO}_2\cdot$]. The acetoxy radical has two resonantly identical oxygens, and will proceed to fragment into CO_2 and CH_3 . Slightly higher in energy is Reaction (4.3), cleavage of the C-C bond, which produces the $\text{C}(\text{O})\text{OCH}_3$ radical. This radical can continue by either eliminating CO ultimately creating formaldehyde and H atoms, or by fragmentating to CH_3 and CO_2 .

Bond energies well above 90 kcal mol^{-1} do not typically decompose in the reactor [21, 110, 118, 129, 156]. We will consider, however, cleavage of the higher energy C-H bonds the experimental BDEs in methyl acetate and methyl butanoate are currently unknown. Elimination of a methoxy H atom, shown in Reaction (4.4), will create a highly unstable radical [$\text{CH}_3\text{C}(\text{O})\text{OCH}_2\cdot$]. This will quickly collapse to CH_3 , CO and $\text{CH}_2=\text{O}$. Alternatively, loss of a methyl H atom shown in Reaction

Alcohol Fragmentation



Radical Fragmentation



Scheme 4.2: Alcohol and Radical Fragmentation in the Pyrolysis of Methyl Acetate

Reactions 1 - 12	aE_a	$\Delta_{\text{rxn}}H_{298\text{ K}}$	refs.
$\text{CH}_3\text{COOCH}_3 \rightarrow \text{CH}_2=\text{C}=\text{O} + \text{CH}_3\text{OH}$	73	$39.4 \pm 0.5^*$	5, 14, 108, 116, 150
$\text{CH}_3\text{COO}-\text{CH}_3 \rightarrow \text{CH}_3\text{CO}_2 + \text{CH}_3$	86		116
$\text{CH}_3-\text{COOCH}_3 \rightarrow \text{CH}_3 + \text{COOCH}_3$	93		116
$\text{CH}_3\text{COOCH}_3 \rightarrow \text{CH}_2\text{COOCH}_3 + \text{H}$		94	est.
$\text{CH}_3\text{COOCH}_3 \rightarrow \text{CH}_3\text{COOCH}_2 + \text{H}$		97	150
$\text{CH}_3\text{CH}_2\text{CH}_2\text{COOCH}_3 \rightarrow \text{CH}_3\text{CH}_2\text{CH}=\text{C}=\text{O} + \text{CH}_3\text{OH}$	74 ± 1	40 ± 1	41
$\text{CH}_3\text{CH}_2\text{CH}_2\text{COOCH}_3 \rightarrow \text{CH}_2=\text{CH}_2 + \text{CH}_2=\text{C}(\text{OH})\text{OCH}_3$	68 ± 1	53 ± 1	41
$\text{CH}_3\text{CH}_2-\text{CH}_2\text{COOCH}_3 \rightarrow \text{CH}_3\text{CH}_2 + \text{CH}_2\text{COOCH}_3$		84 ± 1	41
$\text{CH}_3\text{CH}_2\text{CH}_2\text{COO}-\text{CH}_3 \rightarrow \text{CH}_3\text{CH}_2\text{CH}_2\text{CO}_2 + \text{CH}_3$		87 ± 1	41
$\text{CH}_3-\text{CH}_2\text{CH}_2\text{COOCH}_3 \rightarrow \text{CH}_3 + \text{CH}_2\text{CH}_2\text{COOCH}_3$		89 ± 1	41
$\text{CH}_3\text{CH}_2\text{CH}_2\text{COOCH}_3 \rightarrow \text{H} + \text{CH}_3\text{CH}_2\text{CH}-\text{COOCH}_3$		94 ± 1	41
$\text{CH}_3\text{CH}_2\text{CH}_2\text{COOCH}_3 \rightarrow \text{H} + \text{CH}_3\text{CH}_2\text{CH}_2\text{COOCH}_2$		99 ± 1	41

Table 4.1: Experimental, Calculated, and Estimated Thermochemistry for Rxs (1) - (12)

Additional reactions, kcal mol ⁻¹	^a E _a	Δ _{rxn} H _{298 K}	refs.
HCO-OCH ₃ → HCO + OCH ₃		100 ± 2*	5, 14, 62, 67, 150
HCOO-CH ₃ → HCO ₂ + CH ₃		90 ± 3*	5, 14, 62, 67, 150
HCOOCH ₃ → COOCH ₃ + H		88	est.
HCOOCH ₃ → HCOOCH ₂ + H		96	est.
CH ₂ =CHCH ₃ → CH ₂ =CHCH ₂ + H		88.6 ± 0.5*	14, 114, 149
CH ₂ =CHCH ₃ → CH ₂ =CH + CH ₃		101.3 ± 0.7*	14, 114
CH ₃ COOCH ₃ → CH ₂ =O + CH ₃ CHO		32.8 ± 0.4*	5, 14
CH ₃ COOCH ₃ → CH ₂ =C(OH)OCH ₃	71	29	116
CH ₃ CO-OCH ₃ → CH ₃ CO + OCH ₃		100.5 ± 0.7*	5, 14
CH ₃ COO-CH ₃ → CO ₂ + 2 CH ₃		74.0 ± 0.1*	5, 33, 127
CH ₃ CH ₂ CH ₂ CO-OCH ₃ → CH ₃ CH ₂ CH ₂ CO + OCH ₃		101 ± 1	41
CH ₃ CH ₂ CH ₂ COOCH ₃ → CH ₃ CH ₂ CH ₂ + COOCH ₃		93 ± 1	41
CH ₃ CH ₂ CH ₂ COOCH ₃ → CH ₃ CH ₂ CH=C(OH)OCH ₃		74 ± 1	41
CH ₃ CH ₂ CH ₂ COOCH ₃ → CH ₃ CH ₂ CH ₂ CHO + CH ₂ =O	77 ± 1	33 ± 1	41
CH ₃ CH ₂ CH ₂ COOCH ₃ → CH ₃ CH=CH ₂ + HCOOCH ₃	105 ± 1	81 ± 1	41

Table 4.2: Additional Thermochemistry

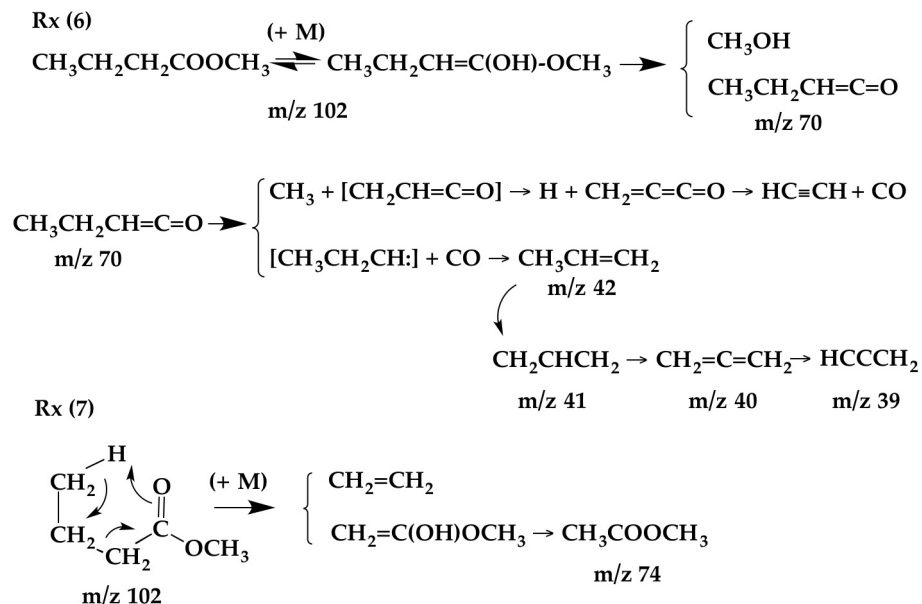
^aE_a energies of activation are reported at 298 K.

(4.5) creates the unstable radical [$\cdot\text{CH}_2(\text{O})\text{OCH}_3$]. This will likely form ketene $\text{CH}_2=\text{C}=\text{O}$ and methoxy radical OCH_3 , which will then proceed to eliminate H atom to form formaldehyde.

4.3.2 Methyl Butanoate

Potential decomposition pathways of methyl butanoate are summarized in Schemes 4.3 - 4.5. The lowest energy rearrangement is shown in Reaction (4.6), which forms ethylketene ($\text{CH}_3\text{CH}_2\text{CH}=\text{C}=\text{O}$) and methanol. Loss of CO from ethylketene followed by a rapid H atom shift leads to propene. This has the potential for multiple, additional H atoms losses, resulting first in allyl radical CH_2CHCH_2 , then allene $\text{CH}_2=\text{C}=\text{CH}_2$, and lastly propargyl radical HCCCH_2 . Alternatively, elimination of methyl radical and H atom from ethyl ketene will leave propadienone $\text{CH}_2=\text{C}=\text{C}=\text{O}$. This will continue to decompose, losing CO to form the carbene [$:\text{C}\equiv\text{CH}_2$], which will quickly rearrange to acetylene $\text{HC}\equiv\text{CH}$ [29]. Methyl butanoate could also eliminate ethylene *via* a Cope rearrangement [39], see Reaction (4.7). Any methyl acetate produced will continue to decompose as discussed in the previous section. It has also been proposed that a rearrangement to

Methyl Butanoate/Alcohol Formation



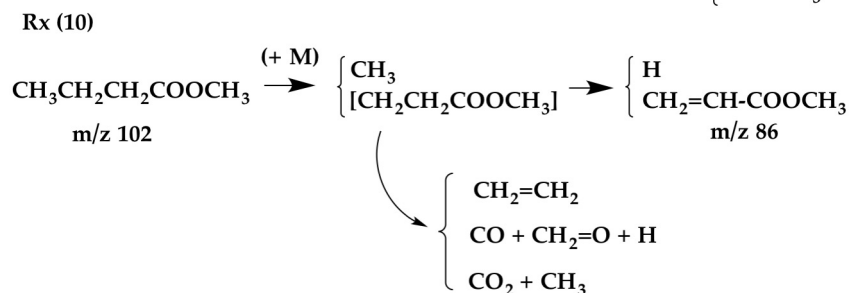
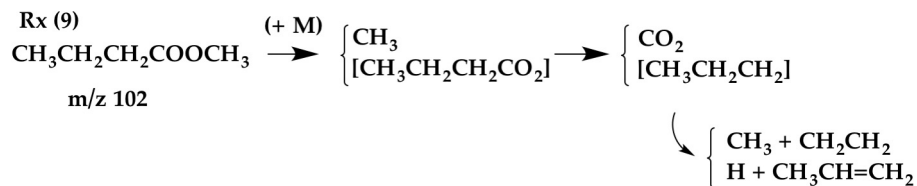
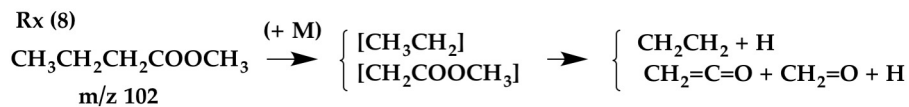
Scheme 4.3: Part 1 Decomposition Pathways of Methyl Butanoate

butyraldehyde $\text{CH}_3\text{CH}_2\text{CH}_2\text{CHO}$ and formaldehyde $\text{CH}_2=\text{O}$ faces a low barrier of activation [41,116], however we see no evidence that this reaction is important under the given conditions.

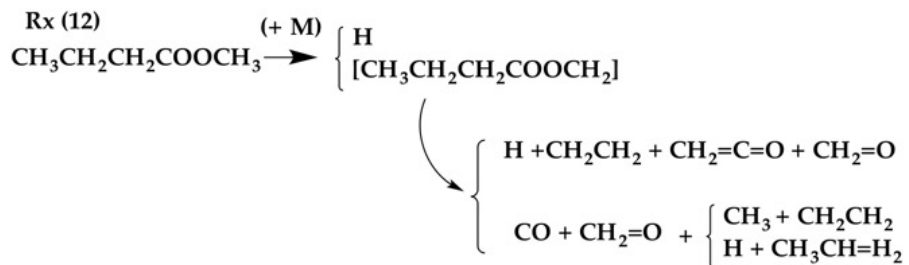
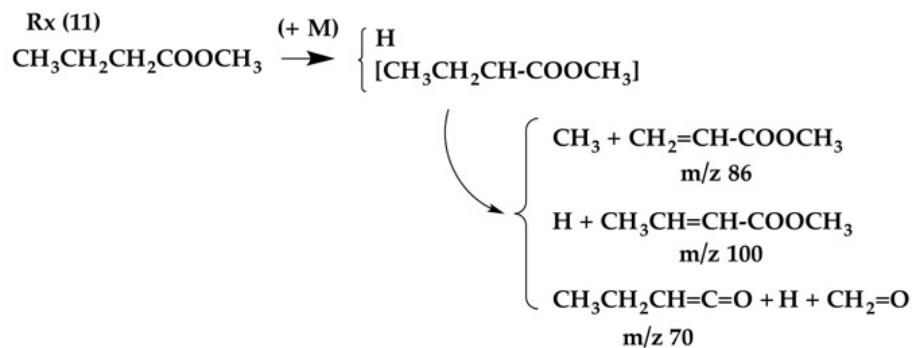
Higher in energy is cleavage of the C-C and C-O bonds, see Tables 4.1 and 4.1. Cleavage of the $\text{C}_\alpha - \text{C}_\beta$ results in Reaction (4.8); ethyl radical CH_3CH_2 will quickly eliminate H atom forming ethylene $\text{CH}_2=\text{CH}_2$. The $\text{CH}_2\text{C}(\text{O})\text{OCH}_3$ radical will decompose to ketene and methoxy radical, which ultimately leads to formaldehyde and H atom. Cleavage of the O-C bond shown in Reaction (4.9) forms a methyl and a $\text{CH}_3\text{CH}_2\text{CH}_2\text{CO}_2$ radical. The $\text{CH}_3\text{CH}_2\text{CH}_2\text{CO}_2$ radical will readily eliminate CO_2 leaving the propyl radical, which can omit an H atom to make propene $\text{CH}_3\text{CH}=\text{CH}_2$ or cleave to methyl radical and ethylene. Cleavage of the terminal $\text{C}_\beta - \text{C}_\gamma$ bond, see Reaction (4.10), forms methyl radical and the $\text{CH}_2\text{CH}_2\text{C}(\text{O})\text{OCH}_3$ radical, which could proceed to fragment in two different ways. Elimination of ethylene is followed by loss of CO or CO_2 , which ultimately results in formaldehyde and H atom, or a methyl radical, respectively. The $\text{CH}_2\text{CH}_2\text{C}(\text{O})\text{OCH}_3$ radical could instead remove a hydrogen *via* β -scission to form methyl acrylate, $\text{CH}_2=\text{CH}-\text{COOCH}_3$.

Highest in energy will be cleavage of C-H bonds, see Tables 4.1 and 4.2. There are two C-H bonds that will be lower in energy due to resonance stabilization of the resulting radical, see Reactions (4.11) and (4.12). In Reaction (4.11), loss of H atom from the α carbon results in the

Methyl Butanoate/Radical Formation



Scheme 4.4: Part 2 Decomposition Pathways of Methyl Butanoate



Scheme 4.5: Part 3 Decomposition Pathways of Methyl Butanoate

[CH₃CH₂CH–COOCH₃] radical. This unstable species can proceed in three potential ways. Loss of methyl radical ultimately forms methyl acrylate CH₂=CH–COOCH₃, elimination of H atom results in crotonic acid CH₃CH=CH–COOCH₃, or elimination of methoxy radical leads to ethyl ketene, H atom, and formaldehyde. Reaction (4.12) shows loss of a methyl group hydrogen, and produces the [CH₃CH₂CH₂COOCH₂] radical which could decompose in three ways. Elimination of formaldehyde followed by ketene leaves the ethyl radical, which ultimately forms H atom and ethylene H₂C=CH₂. Elimination of formaldehyde followed by CO produces the propyl radical, which can proceed as previously discussed.

Previous work [41, 112] suggests that isomerization reactions of the methyl esters to their respective enols (see Reactions (4.1) and (4.6)) face low barriers of around 70 kcal mol⁻¹ [41, 112]. These, however, will be difficult to discern given the current experimental setup due to similarities in mass and lack of vibrational data on these products. Using tunable synchrotron radiation in future studies, enols could be identified by their characteristically lower ionization energies than their carbonyl parents [118]. Alternatively, isotopic labeling studies would be useful to determine if these reactions are significant. One could at least estimate that the O-C single bond would still be somewhat weak in both enols. Loss of methyl radical from the enol of methyl acetate would result in further decomposition: CH₂=C(OH)O–CH₃ → CH₃ + [CH₂=C(OH)O·] → CH₂=C=O + OH. Similarly if there were loss of methyl from the enol of methyl butanoate: CH₃CH₂CH=C(OH)OCH₃ → CH₃ + [CH₃CH₂CH=C(OH)O·] → CH₃CH₂CH=C=O + OH. The hydroxyl radical, OH, is the only unique product of this process, and this cannot be ionized at 10.487 eV.

4.4 Results

4.4.1 Methyl Acetate

We begin our study with the analysis of photoionization mass spectra, see Table 4.3 for a list of ionization energies for important organic species. Figure 4.1 shows the result when methyl acetate (m/z 74) is diluted to 0.07% in helium and heated up to 1600 K. The spectrum is strikingly simple, with thermal decomposition beginning around 1000 K. At 1300 K onward, the only masses evident are m/z 42 and 15. A number of the predicted products from Reactions (4.1) through (4.5) are not expected to ionize at 10.487 eV (see Table 4.3). We assign m/z 42 to ketene produced by Reactions

(4.1) and (4.5), and m/z 15 to methyl radicals products by Reactions (4.2) - (4.4). Methyl acetate appears to be completely decomposed by 1600 K in helium.

In all matrix spectra presented, room temperature methyl acetate is shown in black and heated argon (1400 K) is shown in green for reference. Strong evidence for Reaction (4.1) is shown in Figures 4.2 and 4.3 with the infrared spectra that result when 0.13% methyl acetate in argon is heated at 1200 K and 1500 K. The presence of ketene is clearly indicated in Figure 4.2 by the absorption bands ν_1 (3062 cm^{-1}), ν_2 (2142 cm^{-1}) and ν_4 (1381 cm^{-1}); these are compared to an authentic sample of ketene shown in blue [97]. Figure 4.3 shows strong absorption bands of methanol, ν_3 (2848 cm^{-1}) and ν_8 (1033 cm^{-1}); these are compared to an authentic sample of methanol shown in blue [135].

The remaining products in the pyrolysis of methyl acetate are not unique to any particular pathway. Reactions (4.3) - (4.5) predict the formation of formaldehyde. Figure 4.4 displays three of the observed absorption features of formaldehyde ν_1 (2798 cm^{-1}), ν_2 (1742 cm^{-1}), and ν_3 (1499 cm^{-1}), respectively [104]. Figure 4.5 displays the carbonyl region, where the C=O stretch of ketene (ν_2) is displayed again as well as evidence for CO and CO₂. On the right hand side of Fig. 4.5 are the intense monomer and multimer absorption bands [81] of carbon monoxide at 2149 cm^{-1} and 2139 cm^{-1} , produced by Reactions (4.3) and (4.4). On the left hand side, a CO₂ monomer band at 2345 cm^{-1} and two multimer bands at 2340 cm^{-1} and 2339 cm^{-1} [49] are displayed, produced by Reactions 4.2 and 4.3. It is interesting to note that both panels in Fig. 4.5 are shown to scale; it appears as though CO formation becomes more important at 1500 K. This will be addressed in the Discussion section below.

4.4.2 Methyl Butanoate

Figure 4.6 is the resulting photoionization mass spectrum when 0.06% methyl butanoate (m/z 102) is heated in helium up to 1500 K. The fragment at room temperature m/z 74 is the result of dissociative ionization. Methyl butanoate, with an ionization energy of 10 eV, is imparted 0.487 eV excess energy upon ionization (see Table 4.3). This leads to dissociative ionization of the methyl butanoate cation *via* the McLafferty rearrangement [91], with charge retention on methyl acetate (m/z 74): $[\text{CH}_3\text{CH}_2\text{CH}_2\text{C}(\text{O})\text{OCH}_3^+] \rightarrow [\text{CH}_3\text{C}(\text{O})\text{OCH}_3^+] + \text{H}_2\text{C}=\text{CH}_2$.

Thermal decomposition begins around 800 K when m/z 70 appears in Fig. 4.6. We assign this

m/z	species	name	IE/eV		refs.
1	H	H atom	13.59884	± 0.00001	98
15	CH ₃	methyl radical	9.8380	± 0.0004	15
26	HC≡CH	acetylene	11.40081	± 0.00001	119
17	OH	hydroxyl radical	13.01698	± 0.00025	165
28	CH ₂ =CH ₂	ethylene	10.51268	± 0.00001	169
28	CO	carbon monoxide	14.0136	± 0.0005	44
30	CH ₂ =O	formaldehyde	10.8850	± 0.0002	130
31	CH ₃ O	methoxy radical	10.726	± 0.008	126
32	CH ₃ OH	methanol	10.85	± 0.01	11
39	HCCCH ₂	propargyl radical	8.7006	± 0.0002	54
40	CH ₂ =C=CH ₂	allene	9.6880	± 0.0020	173
41	CH ₂ HCCH ₂	allyl radical	8.13146	± 0.00025	170
42	CH ₃ CH=CH ₂	propene	9.7435	± 0.0005	24
42	CH ₂ =C=O	ketene	9.6191	± 0.0004	107
44	CO ₂	carbon dioxide	13.778	± 0.002	157
44	CH ₃ CHO	acetaldehyde	10.2295	± 0.0007	74
70	CH ₃ CH ₂ CH=C=O	ethylketene		8.8	16
72	CH ₃ CH ₂ CH ₂ CHO	butyraldehyde	9.73	± 0.03	30
74	CH ₃ C(O)OCH ₃	methyl acetate	10.25	± 0.05	9
86	CH ₂ =CHC(O)OCH ₃	methyl acrylate		10.74	153
100	CH ₃ CH=CHCOOCH ₃	methyl crotonate			
102	CH ₃ CH ₂ CH ₂ C(O)OCH ₃	methyl butanoate	10.07	± 0.03	159

Table 4.3: Mass and Ionization Energies of Important Organics

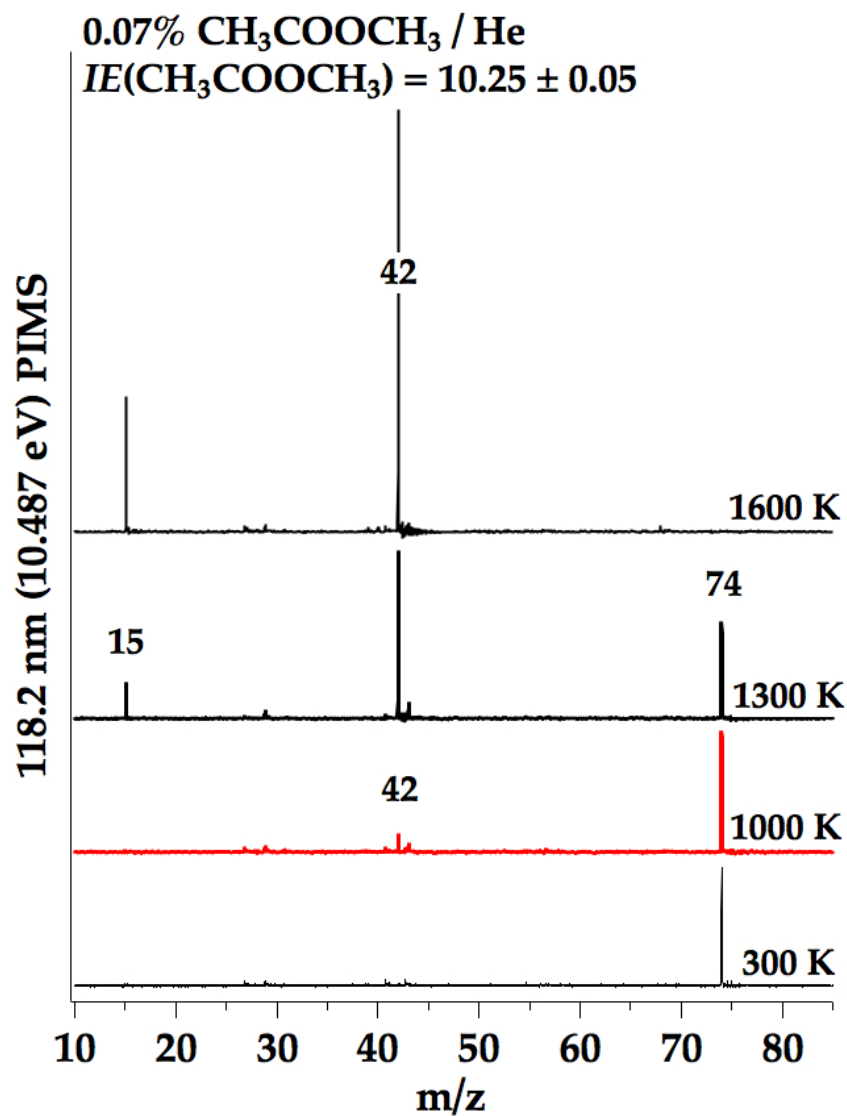


Figure 4.1: Photoionization mass spectrum of 0.07% methyl acetate in helium heated up to 1600 K in the micro reactor.

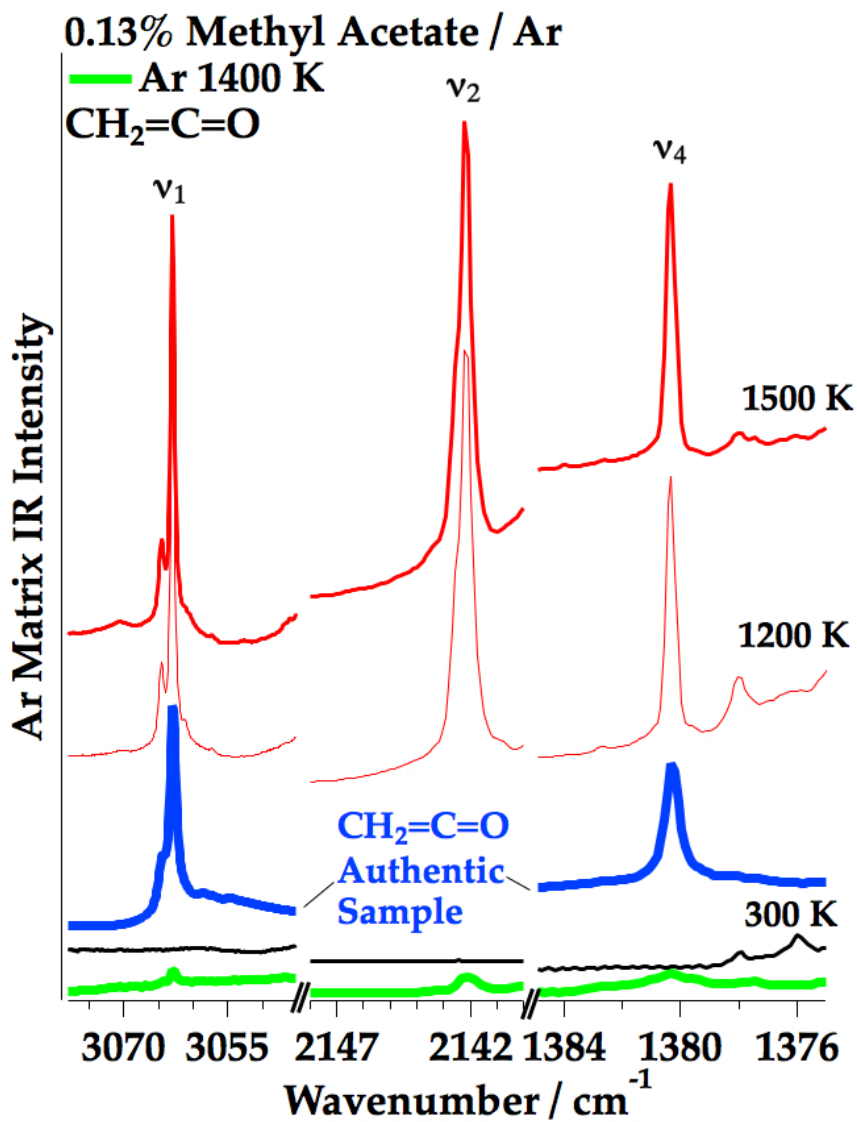


Figure 4.2: Matrix infrared spectrum of 0.13% methyl acetate heated to 1200 and 1500 K in argon. An authentic sample of ketene is shown in blue for reference, however the carbonyl stretch at 2142 cm^{-1} oversaturated the detector and is not displayed.

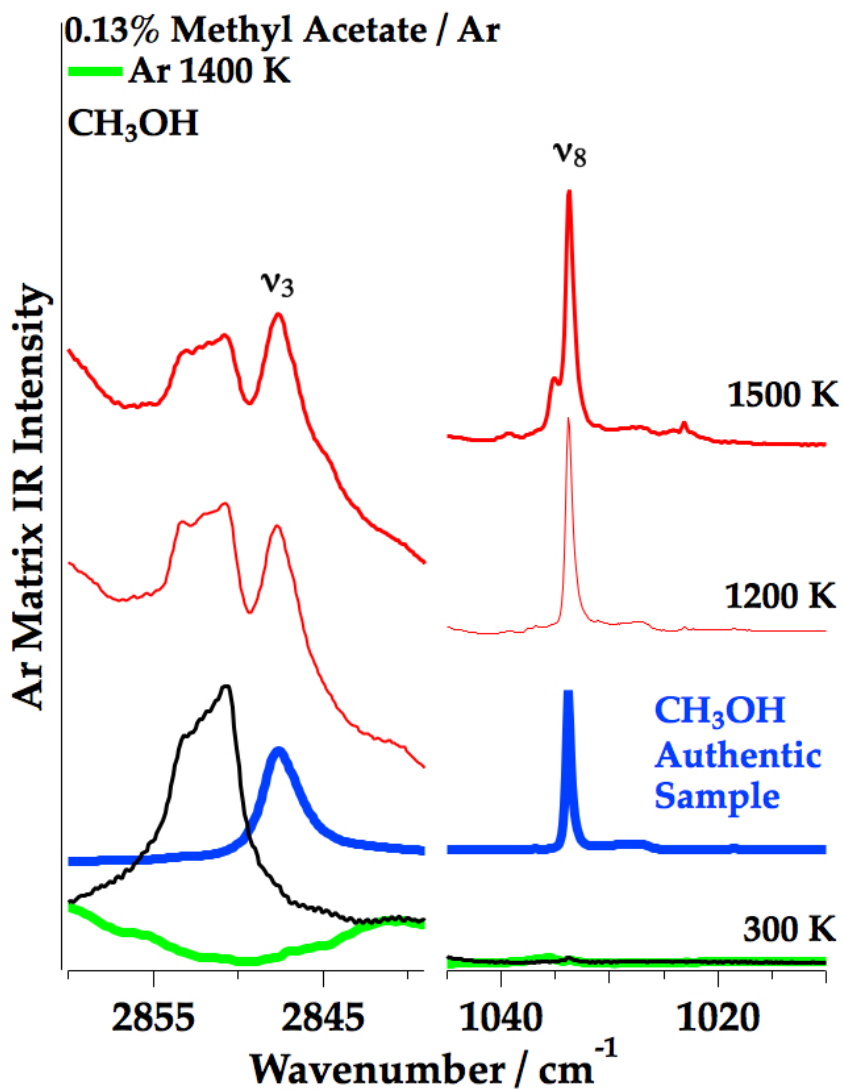


Figure 4.3: Matrix infrared spectrum of 0.13% methyl acetate heated to 1200 and 1500 K in argon. In blue is an authentic sample of methanol for reference.

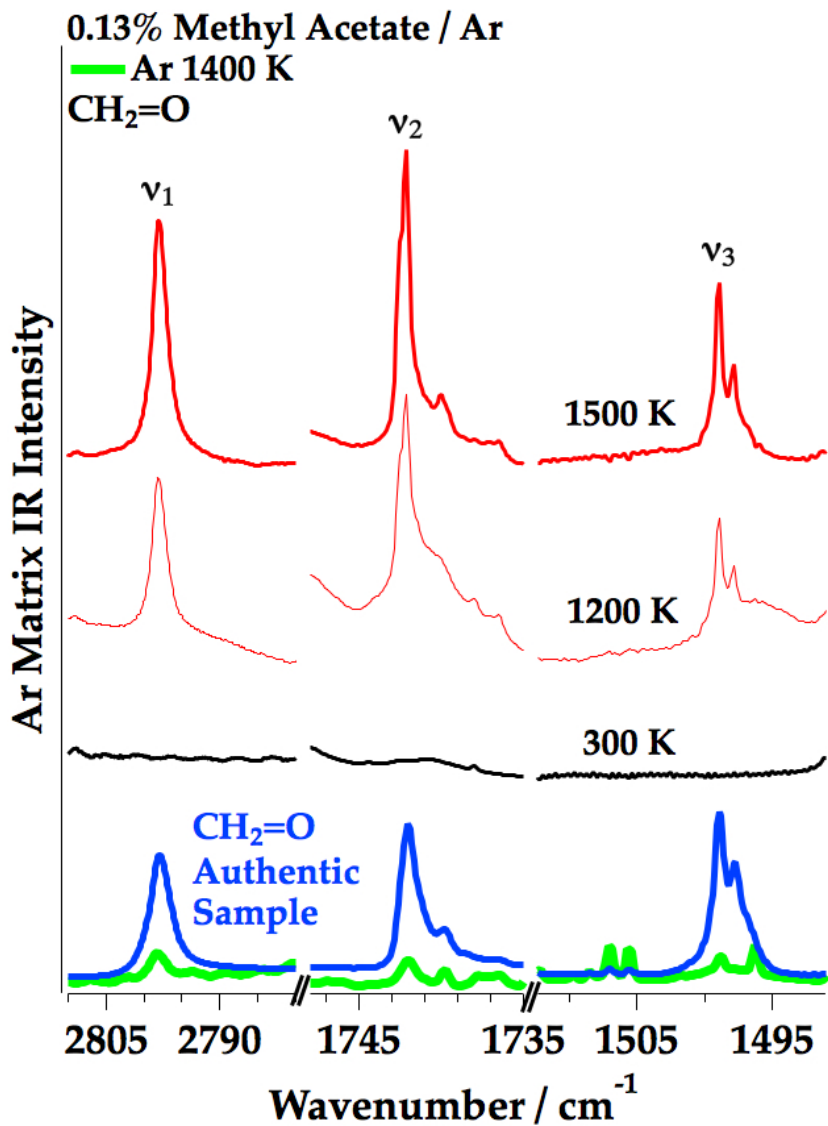


Figure 4.4: Matrix infrared spectrum of 0.13% methyl acetate heated to 1200 K and 1500 K in argon. In blue is an authentic sample of formaldehyde for reference.

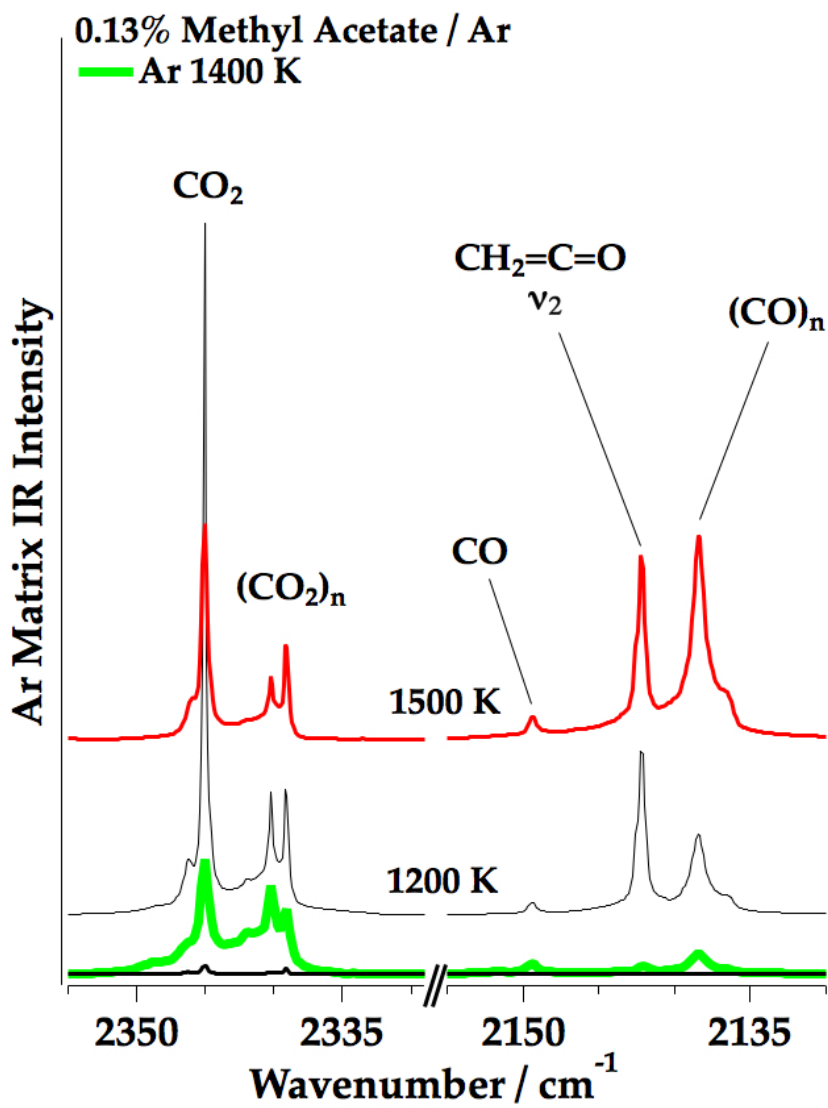


Figure 4.5: Matrix infrared spectrum of 0.13% methyl acetate heated to 1200 K and 1500 K in argon.

to ethylketene produced by Reaction (4.6), and do not expect to ionize methanol (IE = 10.85 eV). At 1300 K, m/z 42, 28 and 15 appear. Ketene produced by Reaction (4.8) and propene produced by Reactions (4.6) and (4.9) are both assigned to m/z 42. Small amounts of hot ethylene produced by Reaction (4.8) and (4.9) can be seen coming from the micro-reactor at 1300 K and 1500 K at m/z 28 (IE = 10.51 eV). Methyl radical at 1300 K onward is assigned to m/z 15 from Reactions (4.6) and (4.9) - (4.12). We cannot say definitively whether there is evidence for the production of methyl acetate *via* Reaction (4.7) due to the presence of m/z 74 at room temperature, this will be discussed in more detail later.

As temperatures approach 1500 K, we can see additional decomposition of primary products. Propene (m/z 42) in a series of H atom eliminations produces allyl radical (m/z 41), allene (m/z 40) and propargyl radical (m/z 39). Additional evidence for this is provided by an independent PIMS of 0.07% propene in He, see Figure 4.7. The bond energy to lose methyl (m/z 15) from propene is too high for the micro-reactor to break, so we believe m/z 15 is formed *via* H atom addition to propene followed by methyl radical elimination. In contrast to methyl acetate, methyl butanoate is almost completely decomposed by 1300 K in helium, see Fig. 4.1.

Strong support for Reaction (4.6) was found in the infrared and is shown in Figures 4.8 through 4.12. Absorption features of methanol ν_3 (2848 cm^{-1}) and ν_8 (1033 cm^{-1}) are clearly present in Fig. 4.8; these are compared to an authentic sample of methanol shown in blue [135]. Reaction (4.6) also predicts the formation of ethylketene ($\text{CH}_3\text{CH}_2\text{CH}=\text{C}=\text{O}$) and its products of decomposition: CH_3 , $\text{CH}_2=\text{C}=\text{C}=\text{O}$, CO , $\text{HC}\equiv\text{CH}$, and $\text{CH}_2=\text{CHCH}_3$. Figure 4.9 displays the carbonyl stretching region, where we see a strong feature at 2122 cm^{-1} that decreases in intensity from 1100 K to 1600 K; this is assigned to ethylketene [69]. The shoulder of this peak at 2125 cm^{-1} is assigned to propadienone ($\text{CH}_2=\text{C}=\text{C}=\text{O}$). The absorption bands for propadienone and ethylketene decrease in intensity from 1100 to 1600 K, and consequently we see the bands for acetylene grow in at higher temperatures, see Figure 4.10. The acetylene doublet ν_3 is observed at 3289 and 3240 cm^{-1} and ν_5 is observed at 737 cm^{-1} [135].

We also see evidence for propene as ethylketene decomposes, see Figure 4.11 for the observed bands ν_7 , ν_{18} , and ν_{19} at 1453, 998, and 908 cm^{-1} respectively. Two of the pyrolysis products of propene, allyl radical and allene, were also observed in the argon matrix. Figure 4.12 shows the presence of allyl radical CH_2CHCH_2 with absorption bands ν_1 at 3112 cm^{-1} and ν_{11} at 801

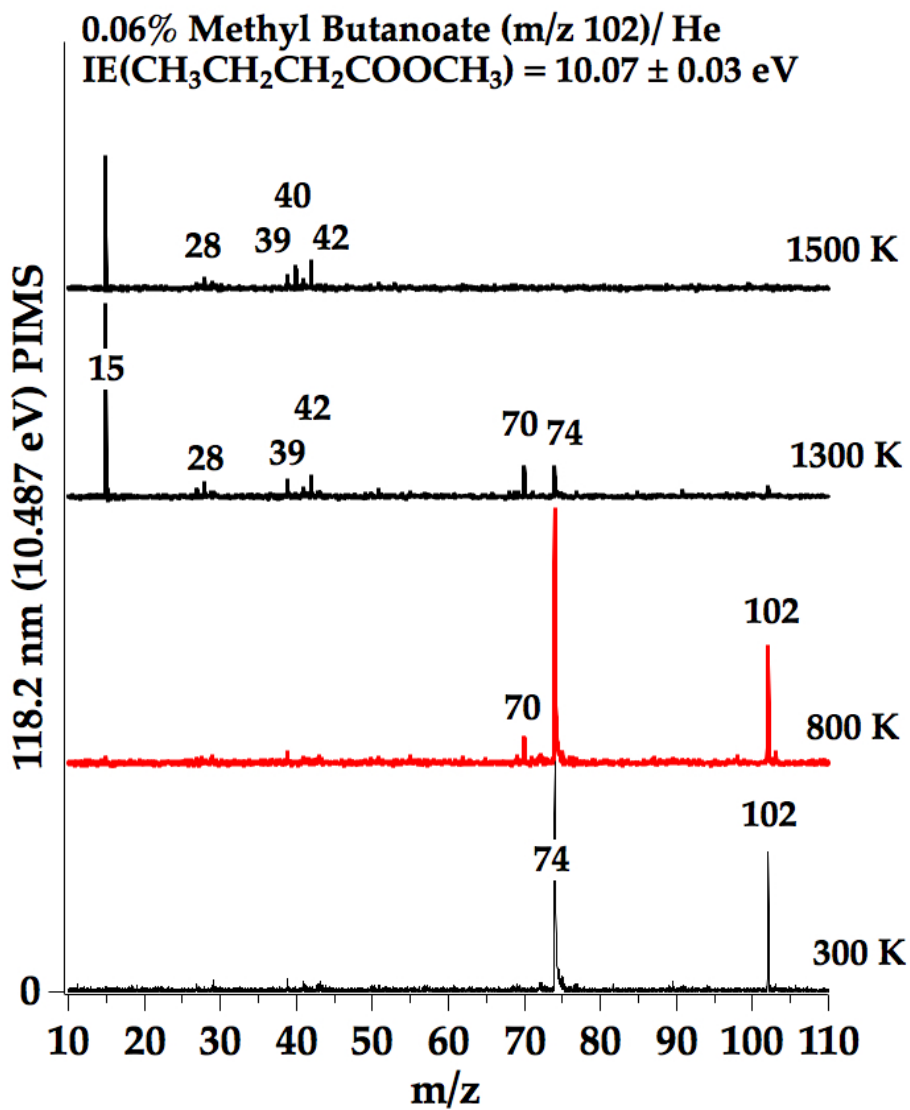


Figure 4.6: Photoionization mass spectrum of 0.06% methyl butanoate in helium heated to 1600 K in the micro-reactor.

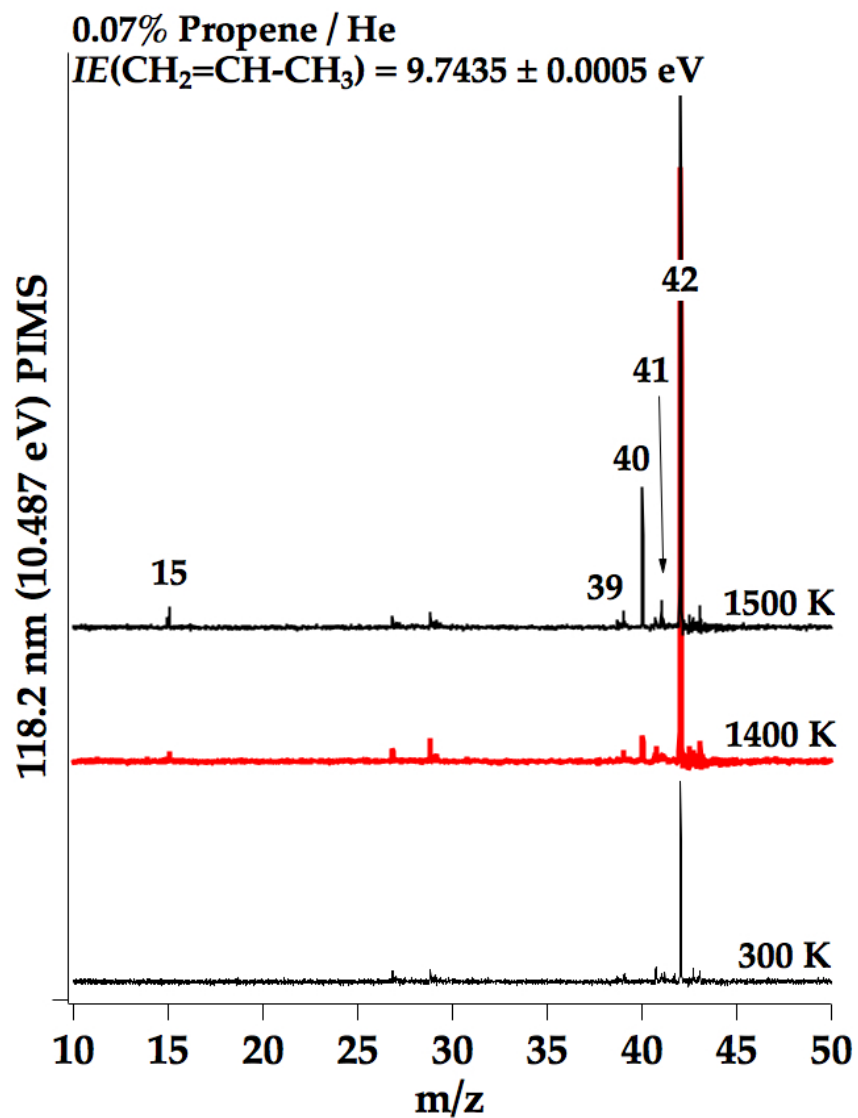


Figure 4.7: Photoionization mass spectrum at 10.487 eV (118.2 nm) of 0.07% propene heated in helium up to 1500 K.

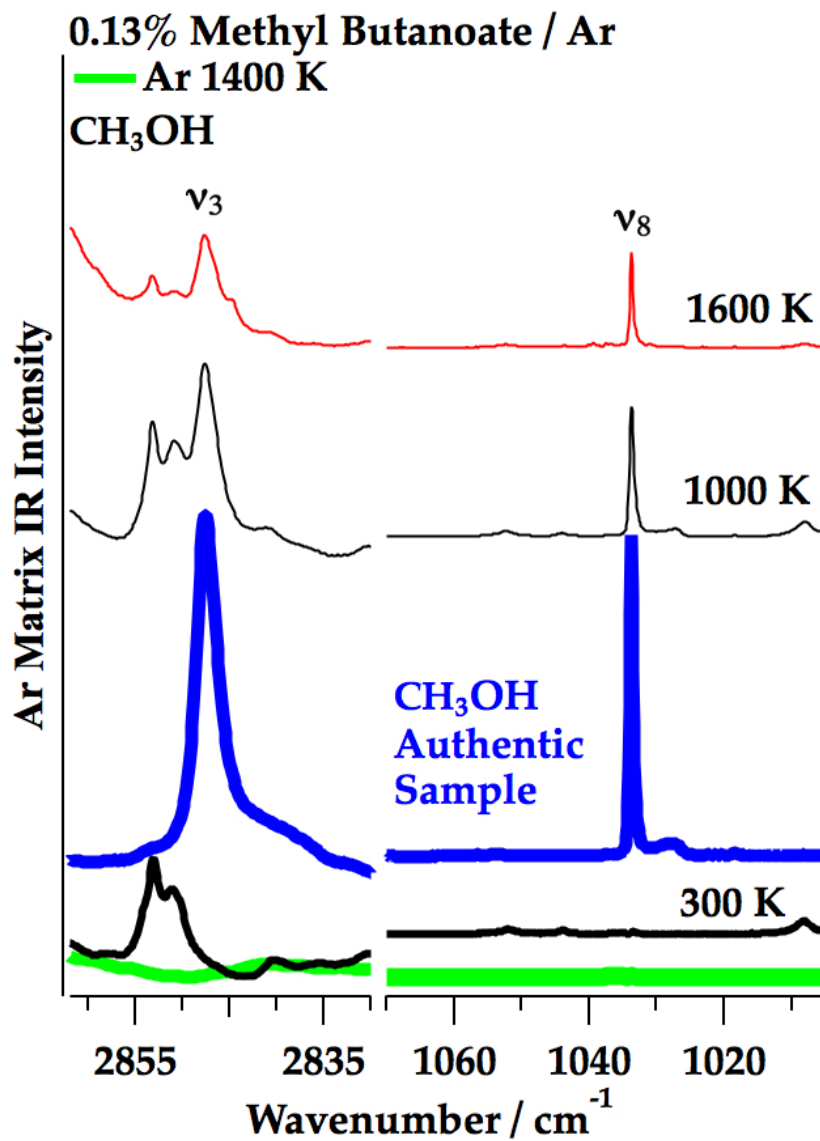


Figure 4.8: Matrix infrared spectrum of 0.13% methyl butanoate heated in argon to 1000 K and 1600 K. An authentic sample of methanol is shown in blue.

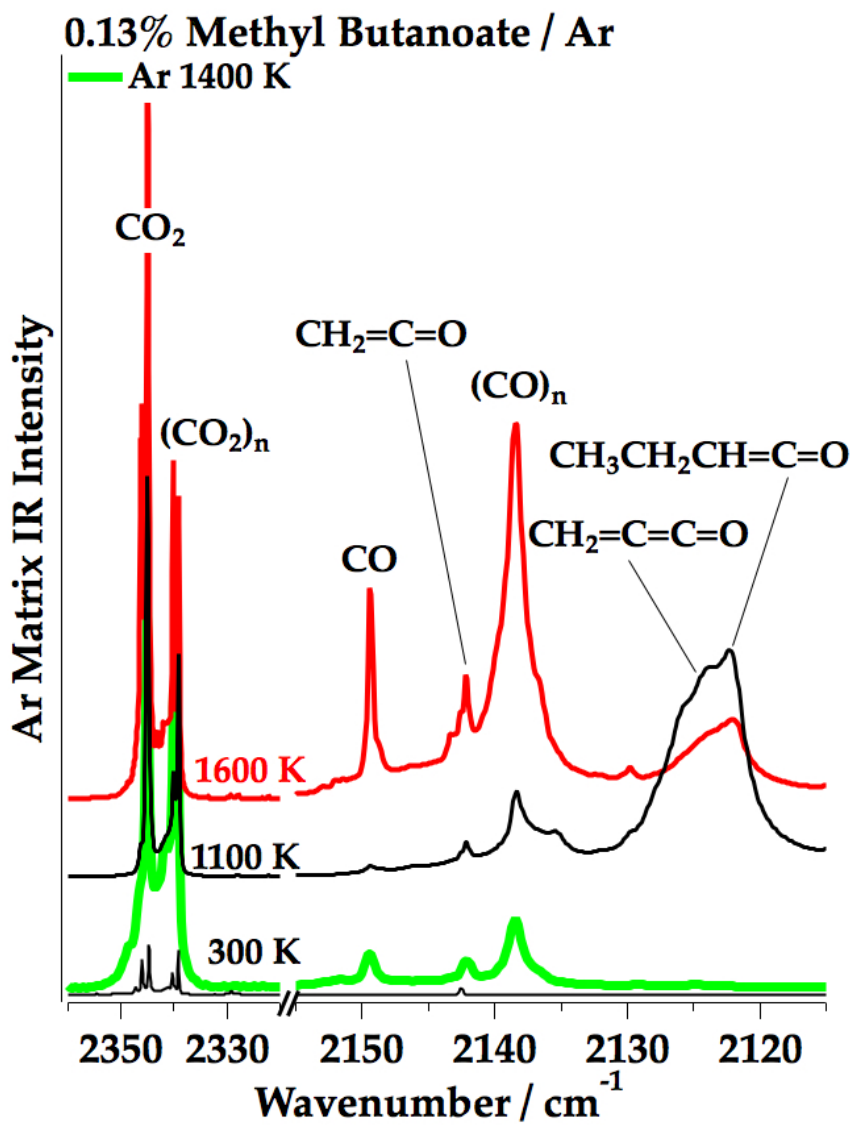


Figure 4.9: Matrix infrared spectrum of 0.13% methyl butanoate heated in argon to 1100 K and 1600 K.

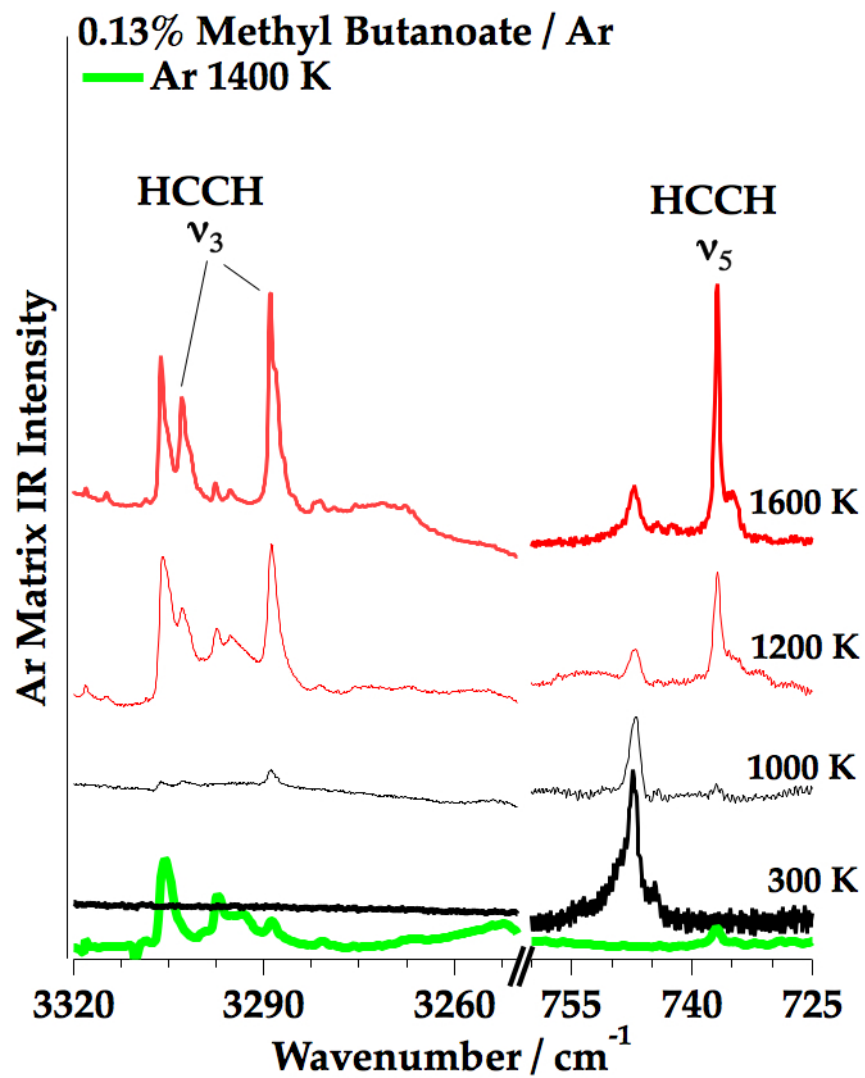


Figure 4.10: Matrix infrared spectrum of 0.13% methyl butanoate heated in argon to 1000 K, 1200 K and 1600 K. Evidence for acetylene HCCH.

CH ₃ COOCH ₃ (+M) → products							
Species	(1)	(2)	(3)	(4)	(5)	PIMS	FTIR
H			✓	✓	✓		
CH ₃		✓	✓	✓		Fig. 4.1	
CO			✓	✓			Fig. 4.5
CH ₂ =O			✓	✓	✓		Fig. 4.4
CH ₃ OH	✓						Fig. 4.3
CH ₂ =C=O	✓				✓	Fig. 4.1	Fig. 4.2
CO ₂		✓	✓				Fig. 4.5

Table 4.4: Summary of Detected Pyrolysis Products of Methyl Acetate

cm⁻¹. Loss of H atom from allyl radical leads to allene CH₂=C=CH₂, for which ν_6 at 1957 cm⁻¹ is displayed on the right hand side of Fig. 4.12. Propene could also have been produced by Reactions (4.9) and (4.12), which would give rise to the same results presented in Figs. 4.11 and 4.12.

The remaining products are not unique to any particular pathway. Evidence for ketene from Reactions (4.8) and (4.12) is displayed in Figure 4.13, with ν_1 (3062 cm⁻¹), ν_2 (2142 cm⁻¹) and ν_4 (1381 cm⁻¹) compared to an authentic sample of ketene shown in blue [97]. Reactions (4.8) and (4.10) - (4.12) are predicted to form formaldehyde, and Figure 4.14 shows its strong absorption features ν_1 and ν_2 at 2798 cm⁻¹ and 1742 cm⁻¹, respectively [104]. Reactions (4.8) - (4.10) and (4.12) all predict ethylene as a product, and Fig. 4.14 displays the strongest absorption band ν_7 at 947 cm⁻¹ [135]; multiple bands were observed. Lastly, CO₂ is expected to form *via* Reactions (9) and (10), and the monomer (2345 cm⁻¹ and multimer absorption bands (2340 cm⁻¹ and 2339 cm⁻¹) are shown in Figure 4.9.

4.5 Discussion

Many of the reactions listed in Schemes 4.2 and 4.3 predict the same products, making isolation of individual decomposition pathways difficult. Tables 4.4 and 4.5 provide a summary of reactions, products, and how they were detected for methyl acetate and methyl butanoate, respectively. From Table 4.4 it can be seen that only Reaction (4.1) has a unique product, methanol. Every other product could be made by at least one additional reaction, and consequently Reactions (4.1) through (4.5) are all still considered possibilities in the thermal decomposition of methyl acetate.

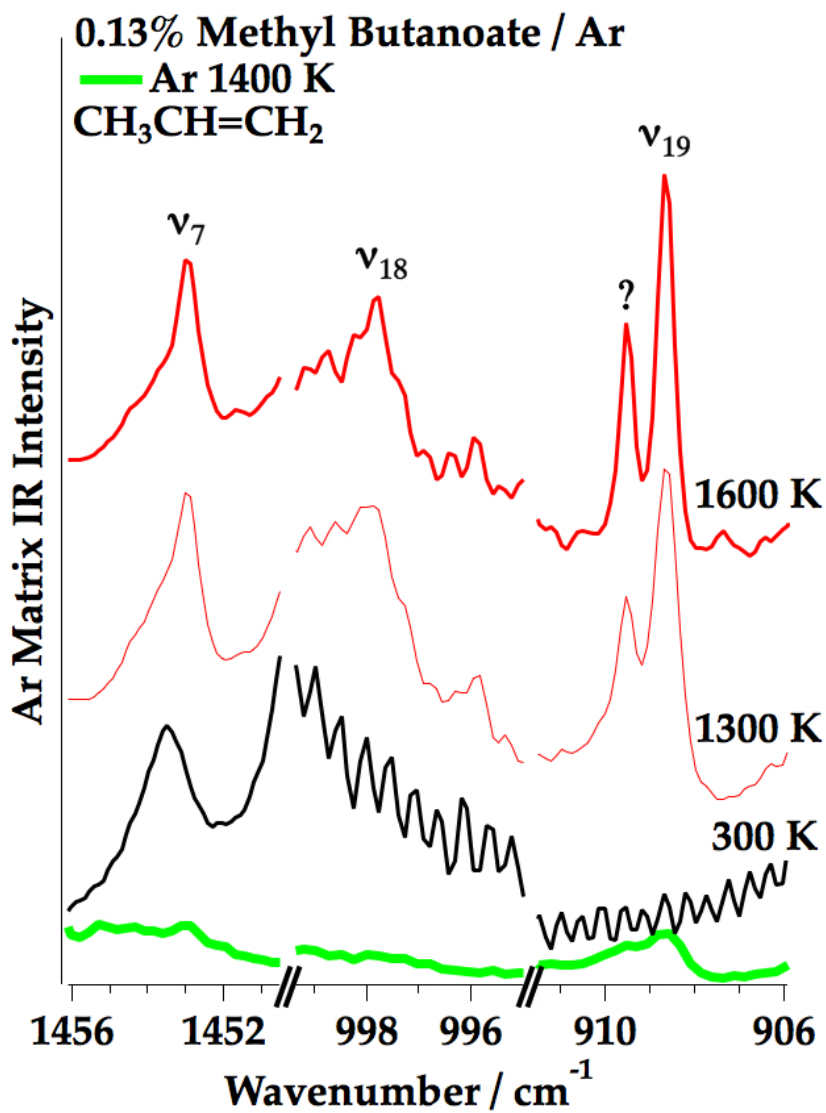


Figure 4.11: Matrix infrared spectrum of 0.13% methyl butanoate heated in argon to 1300 K and 1600 K. Evidence for propene CH₃-CH=CH₂.

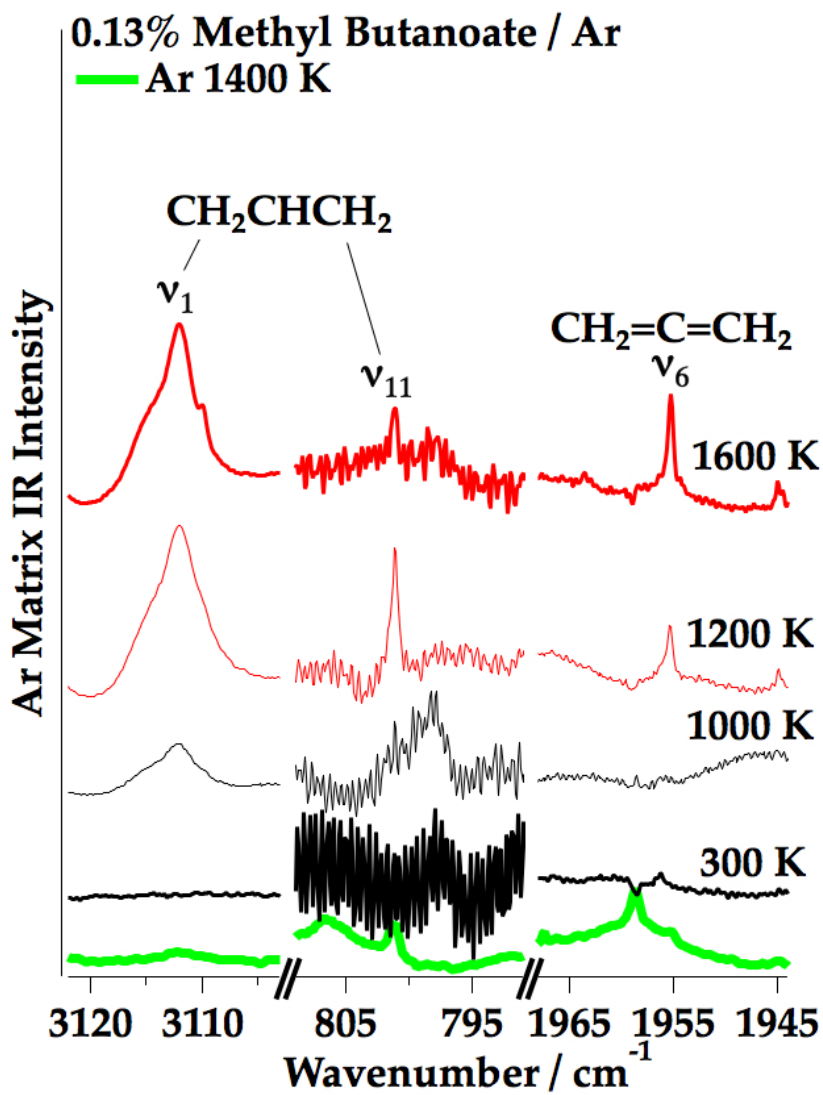


Figure 4.12: Matrix infrared spectrum of 0.13% methyl butanoate heated in argon to 1000 K, 1300 K and 1600 K.

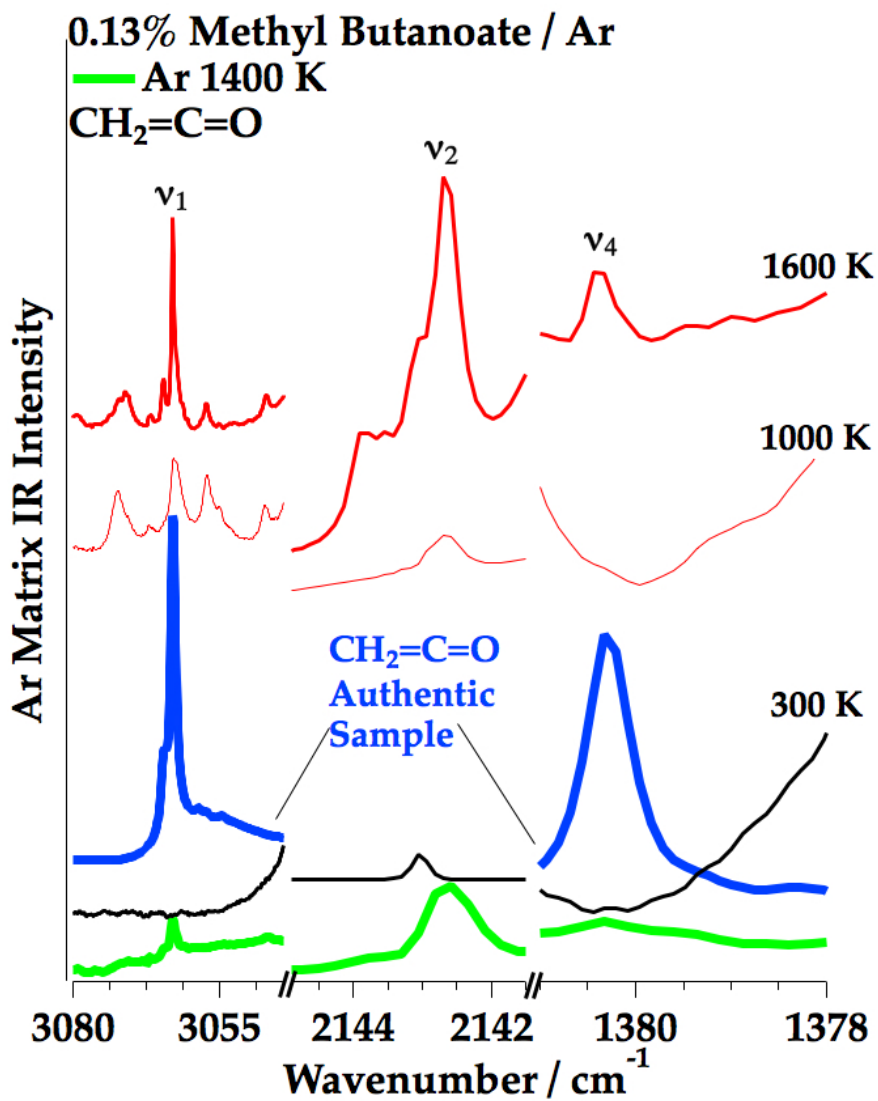


Figure 4.13: Matrix infrared spectrum of 0.13% methyl butanoate heated in argon to 1000 K and 1600 K. An authentic sample of ketene CH₂=C=O is shown in blue for reference.

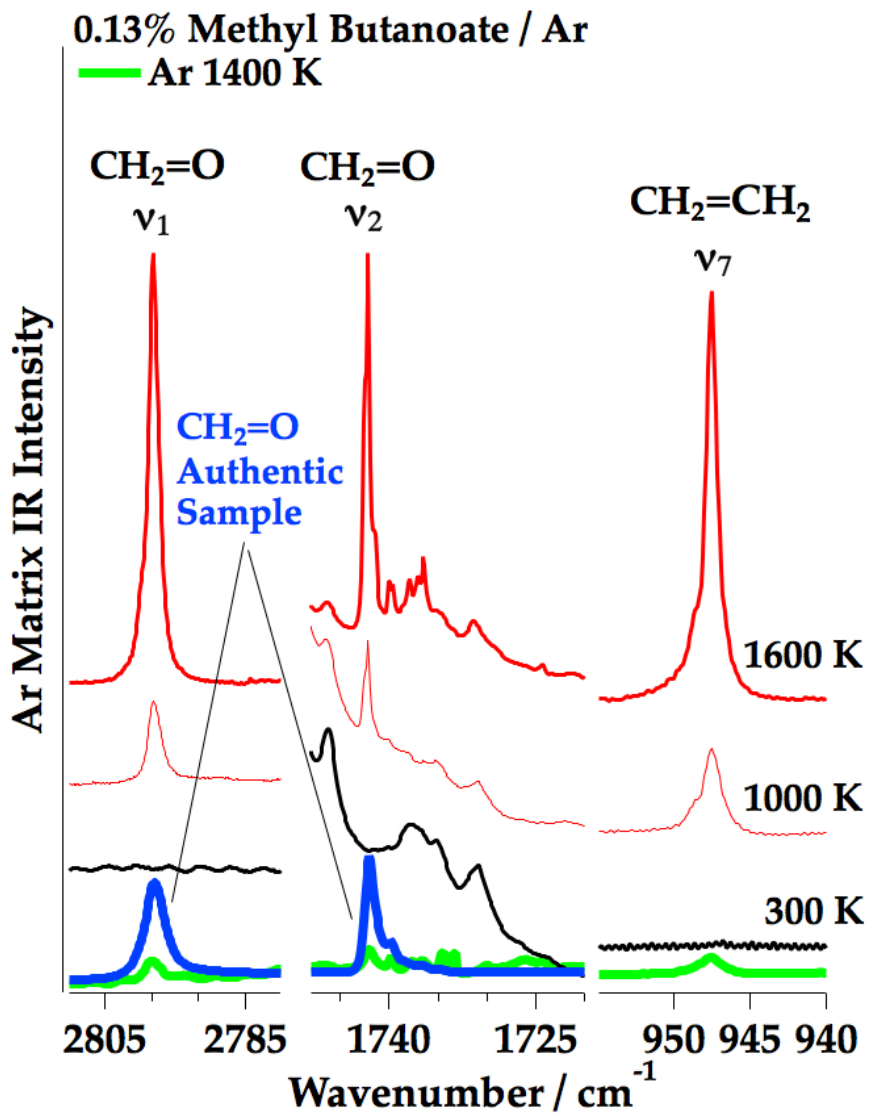


Figure 4.14: Matrix infrared spectrum of 0.13% methyl butanoate heated in argon to 1000 K and 1600 K.

CH ₃ CH ₂ CH ₂ COOCH ₃ (+M) → products									
Species	(6)	(7)	(8)	(9)	(10)	(11)	(12)	PIMS	FTIR
H	✓		✓	✓	✓	✓	✓		
CH ₃	✓			✓	✓	✓	✓	Fig. 4.6	
HC≡CH	✓								Fig. 4.10
CO	✓				✓		✓		Fig. 4.9
CH ₂ =CH ₂		✓	✓	✓	✓		✓	Fig. 4.6	Fig. 4.14
CH ₂ =O			✓		✓	✓	✓		Fig. 4.14
CH ₃ OH	✓								Fig. 4.8
CH ₂ =C=O			✓				✓	Fig. 4.6	Fig. 4.13
HCCCH ₂	✓			✓			✓	Figs. 4.6, 4.7	
CH ₂ =C=CH ₂	✓			✓			✓	Figs. 4.6, 4.7	Fig. 4.12
CH ₂ CHCH ₂	✓			✓			✓	Figs. 4.6, 4.7	Fig. 4.12
CH ₃ CH=CH ₂	✓			✓			✓	Figs. 4.6, 4.7	Fig. 4.11
CO ₂				✓	✓				Fig. 4.9
CH ₂ =C=C=O	✓								Fig. 4.9
CH ₃ CH ₂ CH=C=O	✓						✓	Fig. 4.6	Fig. 4.9
CH ₂ =C(OH)OCH ₃		✓							
CH ₃ COOCH ₃		✓							
CH ₂ =CH-COOCH ₃					✓	✓			
CH ₃ CH=CH-COOCH ₃						✓			
CH ₃ CH ₂ CH=C(OH)OCH ₃	✓								

Table 4.5: Summary of Observed Pyrolysis Products for Methyl Butanoate

There are a handful of previous studies with similar conditions to the micro-reactor. Back in 1981, Carlsen used a Knudsen reactor to pyrolyze methyl acetate and detected at moderate temperatures (1043 - 1404 K) and low pressures (1×10^{-3} Torr) exchange of the methyl group between oxygens [25]. They also observed traceable evidence for alcohol formation, but do not report on radical formation. Yang, using an atmospheric flow reactor from 500 - 1150 K, concluded that both radical and alcohol channels were important [171]. Ren most recently found that 92% of the oxygen recovered was through radical channels in a shock tube at 1406 - 1605 K and 1.5 atm [123]. Peukert also concluded that radical formation was primarily important using a shock tube at 1194 - 1371 K and 0.5 atm [116]. Annesley agreed, claiming that 83 - 88% of methyl acetate decomposed to CH_3 and CO_2 in a single pulse diaphragmless shock tube at 1492 - 2266 K and low pressures of 62 and 122 Torr [4].

Sulzmann reported the only conditions for strictly radical formation, with extreme shock tube conditions of 1425 - 1844 K and 1.17 - 5.65 atm [140]. The current study seems to fall into the mid pressure (200 Torr), mid temperature (1000 - 1600 K) range. Molecular products from Reaction (4.1) appear to be just as prevalent as radical products, which qualitatively agrees with the pressure trends in the literature and estimated energetics.

Another interesting observation was made by Ren, who observed higher concentrations of CO than CO_2 at 1605 K [123]. Figure 4.5 shows that at 1500 K, the multimer band of $(\text{CO})_n$ becomes much more intense than at 1200 K, while the CO_2 absorption appears to decrease at higher temperatures, in line with these findings [123]. We believe we have direct, unambiguous evidence that the products of methyl acetate decomposition come from both alcohol (Reaction 4.1) and radical (Reactions (2) through (5)) fragmentation pathways under the given reactor conditions.

Methyl butanoate has previously been studied by shock tube twice by Farooq et. al., however they did not consider alcohol formation products ethylketene and methanol [45,46]. Paradaman studied 2% methyl butanoate in argon behind reflected shockwaves at 1229 - 1427 K and detected the major products CH_4 , C_2H_4 and $\text{HC}\equiv\text{CH}$ by gas chromatography and FTIR. At these higher concentrations, CH_4 was likely formed by H atom abstraction from the parent by CH_3 , C_2H_4 was either formed by CH_3 recombination followed by loss of H_2 or from previously discussed pathways, and $\text{HC}\equiv\text{CH}$ was likely formed by the decomposition of the intermediate ethylketene.

All products of alcohol fragmentation (Reaction (4.6)) have been observed by FTIR, PIMS, or

both except for H atom and the enol of methyl butanoate (1-methoxy-1-buten-1-ol). Acetylene and methanol are both unique products to Reaction (4.6), see Figs. 4.8 and 4.10. As discussed previously, 1-methoxy-1-buten-1-ol could be identified by its characteristic ionization energy using tunable synchrotron radiation [118], however that is for another study. Reactions (4.1) and (4.7) also have enols that could be identified in the same manner, however there is also no vibrational data available on these enols.

Care was taken to study low temperature rearrangements (1000 K) of methyl butanoate in the matrix to identify intermediates before they decomposed. Reaction (4.7) predicts the formation of the enol of methyl acetate (1-methoxy-ethen-1-ol), which could then isomerize to methyl acetate. Methyl acetate has a very strong carbonyl stretch in the infrared [135] at 1760 cm^{-1} , and no evidence of this stretch was seen in the matrix between 1000 - 1600 K. This Cope rearrangement was concluded by El-Nahas *et.al.* to contribute to less than 1% of the overall product distribution in methyl acetate pyrolysis [41]. This leads us to believe Reaction (4.7) is insignificant under these conditions, however to be certain one would need the matrix infrared frequencies of 1-methoxy-ethen-1-ol. It remains possible, though unlikely, that methyl acetate is produced and then rapidly decomposes to common products.

Other cyclic rearrangements have been proposed for methyl butanoate by structural theorists, see Table 4.1 [3, 41, 112]. Specifically, decomposition of methyl butanoate to butyraldehyde and formaldehyde was considered, however no evidence of butyraldehyde was found in the PIMS or FTIR. It has also been proposed that methyl butanoate could rearrange to methyl formate and propene, however the strong carbonyl stretch of methyl formate was never observed in the FTIR.

4.6 Conclusions

The unimolecular thermal decomposition of methyl acetate and methyl butanoate has been studied in a heated micro-reactor. Methyl acetate decomposition first began in helium around 1000 K and resulted in the following products by 1600 K: H atom, CH_3 , CO, $\text{CH}_2=\text{O}$, CH_3OH , $\text{CH}_2=\text{C}=\text{O}$ and CO_2 . Under the given conditions, we believe these products are formed primarily through Reactions (1) - (3) with Reactions (4) and (5) being more important at higher temperatures and pressures. This is the first time that formaldehyde, methanol, and ketene have been observed

directly by FTIR in the pyrolysis of methyl acetate.

Methyl butanoate has been observed to decompose (beginning around 800 K) in helium to the following products by 1600 K: H atom, CH₃, HC≡CH, CO, CH₂=CH₂, CH₂=O, CH₃OH, CH₂=C=O, HCCCCH₂, CH₂=C=CH₂, CH₂CHCH₂, CH₃CH=CH₂, CO₂, CH₂=C=C=O, and CH₃CH₂CH=C=O. We believe the main pathways for this product distribution come from Reactions (6) and (8) - (10), with no evidence for the low energy rearrangement Reaction (7), and Reactions (11) and (12) being more important at higher temperatures and pressures. This is the first time that CH₂=O, CH₃OH, and CH₂=C=O have been detected by FTIR, and this is the very first direct observation of HCCCCH₂, CH₂=C=CH₂, CH₂CHCH₂, CH₂=C=C=O, and CH₃CH₂CH=C=O in the thermal decomposition of methyl butanoate. Radical fragmentation and alcohol fragmentation have both been shown to be important unimolecular pathways in the thermal decomposition of methyl acetate and methyl butanoate.

Chapter 5

X-ray Fluorescence Studies

5.1 Introduction

The previous chapters have discussed the thermal cracking of a number of potential biofuels. If these biofuels are going to become actual liquid fuels for transportation, then extracting reliable chemical kinetic data for their complex decomposition reactions is essential. The speed at which highly reactive radicals and intermediates are formed in an engine, as well as the heat released when they continue to react, are critical for evaluating the efficiency and viability of any fuel. Capturing this kinetic information really means deriving rate constants, gas laws as a function of temperature and pressure. This of course is only attainable for the micro-reactor if the gas pressure, temperature, flow conditions, and residence times are known. In situ, non-invasive measurements of the micro-reactor's internal conditions are difficult for two reasons. First, the micro-reactor being composed of opaque SiC cannot be probed with conventional optical techniques. Second, inserting a probe into the 1 mm in diameter tube would severely disrupt the gas flow dynamics.

In collaboration with Professor John W. Daily (Mechanical Engineering, University of Colorado), computational fluid dynamics (CFD) simulations [61] have provided estimates of the internal reactor conditions. These simulations reveal highly non-linear axial temperature and pressure distributions that are strongly dependent upon buffer gas and flow conditions. Baraban et. al. recently constructed an optically accessible micro-reactor [6] for measuring the reactor's internal temperature to compare to these CFD simulations. The reactor, composed of optically transparent quartz, was heated with a cleverly constructed clover shaped set of infrared mirrors. Gas flow

through the reactor was 5% NO in argon, and laser induced fluorescence using the well known $A^2\Sigma^+ - X^2\Pi$ band system of nitric oxide was used to extract the internal temperature of NO as a function of external wall temperature. The resulting temperature profile inside the reactor matched the CFD simulation results [6, 61]. The pressure profile also needs to be measured before biofuel decomposition rate constants can be obtained.

Experiments aimed at measuring the internal pressure of the micro-reactor were conducted at the Advanced Photon Source (APS) at Argonne National Labs in Chicago, IL [148]. Density profiles (which can be translated into pressure) of flowing gases within the opaque micro-reactor were measured for the first time using X-ray fluorescence (XRF) spectroscopy with krypton as the fluorescent species. In order to make in situ measurements in the SiC micro-reactors, two obstacles must be overcome. First, SiC is a very opaque material such as metal or ceramic, which eliminates the use of standard optical techniques. Second, the inner diameter of the tube is so small (0.6 to 1 mm) that a probe cannot be inserted without severely disrupting the internal flow field. Typically, as seen in Chapter 1, an inlet and outlet pressure, flow rate, and external wall temperature are reported with experimental data. Using this information, estimates can be made for residence time (of the target molecule inside the heated reactor) and internal gas temperature and pressure. These can only be estimated assuming either laminar or plugged flow. However, this has been shown by Guan et. al. to be an inaccurate assumption [61].

In the remainder of this chapter, non-intrusive XRF measurements are conducted on He/Kr flow inside the SiC micro-reactor at varied wall temperatures. Direct measurements of gas density within the SiC tube as well as the nearly supersonic jet that exits the reactor are measured with XRF. X-ray absorption measurements complement the XRF studies, and reveal a very intricate internal wall structure. The results provide relative gas density and future improvements are discussed that can yield absolute density measurements.

5.2 Experimental

A schematic is shown in Figure 5.1 along with a coordinate system for the experiment. The SiC tube was vertically suspended in a vacuum chamber with a highly focused X-ray beam (5 m x 7 m) aligned and focused on the tube center. One end of the tube was connected to a gas supply line,

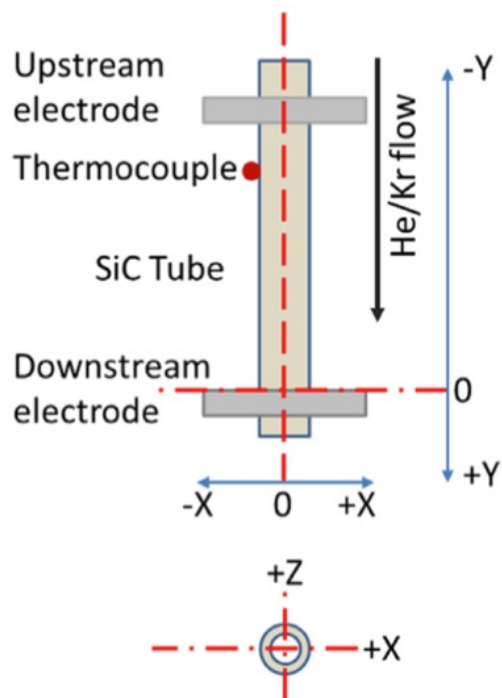


Figure 5.1: The experimental geometry for X-ray studies of Kr fluorescent tags in the microreactor where helium and krypton were independently regulated by mass flow controllers. The other end was open to the vacuum chamber. A total flow rate of 187 sccm was used. Signal trapping at the reactor exit was not as troublesome as it was inside the tube, where photons can be absorbed by the tube walls. Therefore studies done inside the tube required 57% Kr by mass, whereas studies of the eluting jet required only 6% Kr by mass. This Kr concentration was selected to provide sufficient fluorescent signal as well as reasonable collection times of 30 seconds per data point. Inlet pressures (P_{inlet}) were measured using capacitance manometer, and the vacuum chamber pressures were measured with a MicroIon gauge (Granville Phillips) reported as P_{outlet} in Table 5.1. The vacuum chamber was held at 1×10^{-7} Torr by a 550 L/s turbo pump. This was around 1×10^{-3} Torr under gas load. Table 5.1 summarizes experimental conditions for two different SiC tubes used in this study.

The SiC tube was heated in the region between the two electrodes, and the distance between electrodes is contained in Table 5.1. A thick layer of graphite pencil lead was applied to obtain appropriate resistance for heating, as noted in Chapter 1. About 1 mm of the tube extended beyond the electrodes, and was therefore not heated resistively. This section of the tube still appeared to be

	i.d./mm	L/mm	ΔL /mm	T_{wall} /K	P_{inlet} /Torr	P_{outlet} /Torr
#1	0.6	30	18	300	25	1.4×10^{-3}
				1090	65	1.3×10^{-3}
#2	1.0	25	13	300	23	1.4×10^{-3}
				800	48	1.4×10^{-3}
				925	52	1.3×10^{-3}

Table 5.1: SiC tube dimensions and experimental ranges. Gas flow was held at 187 sccm. Here, L represents tube length, ΔL represents distance between electrodes.

heated due to heat transfer from the flowing gases, reducing gas temperatures near the reactor exit. The temperature was monitored by Type K thermocouple, as opposed to the typically used Type C, and this was fastened to the tube exterior with 0.25 mm tantalum wire without any tantalum foil support. The tube, electrodes, and thermocouple had to be placed in the chamber carefully, as not to obstruct the paths of incoming or exiting photons. After about 24 hours of heating, a hole developed in tube #1. The replacement was shorter, forcing the electrodes closer together, see Table 5.1 for tube #2 dimensions. The thermocouple unfortunately interfered excessively with raster scans of tube #2, and we report only the freely expanding jet downstream of the tube.

5.2.1 X-ray diagnostics

These experiments were conducted at beamline 7-BM-B at the Advanced Photon Source (APS), a schematic including the X-ray beam is shown in Figure 5.2. The beamline was composed of a nearly collimated X-ray beam at 15 keV (mean photon energy). Two different measurements were conducted using either an unfocused or focused beam. The unfocused monochromatic beam was used to obtain a series of absorption images (1.3 mm in X, 1.75 mm in Y, see Fig. 5.4) of tube #1, using a LYSO:Ce scintillator (100 μm thick) and an optical microscope.

Most experiments used a focused beam to simultaneously measure fluorescence from Kr in the tube and absorption by the tube walls. The beam was focused using a pair of 300 mm long Kirkpatrick-Baez focusing mirrors. The resulting beam cross section was 5 by 7 μm at full width half maximum. This remained a relatively constant size throughout the 1 mm tube. The incident flux was roughly 1.6×10^{11} photons/s, monitored by diamond photodiode (52 μm thick) prior to the reactor, see Fig 5.2. The absorption was determined with a silicon PIN photodiode (300 μm thick) placed in the beam path after the reaction chamber. This absorption proved very useful in

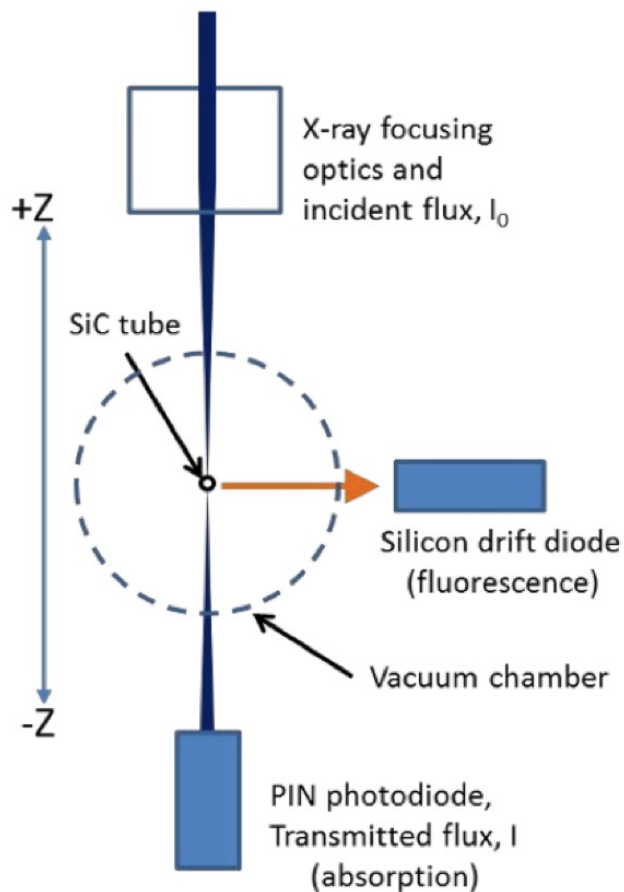


Figure 5.2: The experimental geometry for X-ray studies of Kr fluorescent tags in the microreactor

better understanding the internal shape of the tube.

Krypton has a K-edge energy of 14.325 keV; this is the energy at which a 1s electron will be removed due to absorption of an incident X-ray photon [8]. A resulting $[\text{Kr}^+]^*$ cation has excess energy, which can be relieved by Auger emission (another electron fills its place, releasing energy and emitting an Auger electron) or by fluorescence at 12.649 keV ($\text{KrK}\alpha_1$) [8]. The X-ray fluorescence is directly proportional to the initial X-ray flux and path length integrated density of krypton in the beam path. The fluorescence signal can therefore be used as a direct measure of the gas density. Each element emits fluorescent photons at a unique energy, allowing the Kr signal to be separated from other elements, see Figure 5.3

Previously, argon has been used as an XRF tracer, with a $\text{K}\alpha_2 = 2.995$ keV [70]. It was important for this experiment, however, that the X-rays were of sufficient energy to penetrate the

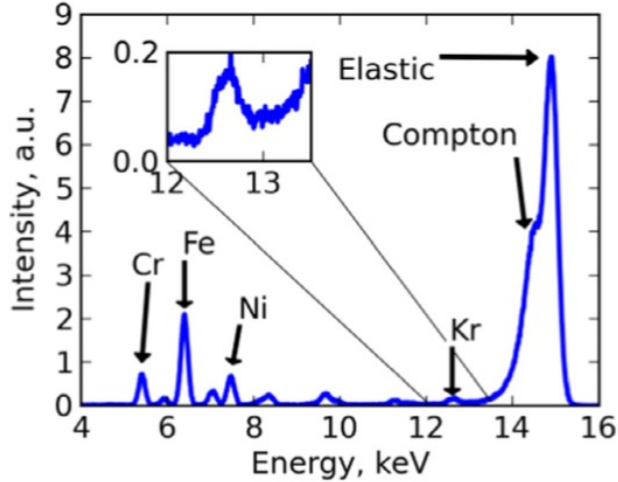


Figure 5.3: Example of fluorescence signal from 15 keV X-rays, used to penetrate the SiC walls and ionize Kr inside the tube.

SiC walls. The resulting fluorescence also needed to meet this requirement. In these experiments the tube walls were roughly $500 \mu\text{m}$ thick, and transmission through one tube was 0.325 at 15 keV (absorption coefficient = $7.48 \text{ cm}^2/\text{g}$ [10]). The X-ray transmission is much lower at the $\text{KrK}\alpha_1$ energy, only 0.153 around 12.7 keV (absorption coefficient of $12.45 \text{ cm}^2/\text{g}$ [10]). Although the incident and fluorescent photons have enough energy to transmit through the walls of the tube, corrections are still needed due to signal trapping.

X-rays were able to enter and exit the chamber thanks to thin (0.127 mm) polyimide windows, which absorb a very small but known amount of X-ray photons. To detect the fluorescent photons, a silicon drift diode detector was used, which was placed at a 90° from the propagation direction of the incident beam, see Fig. 5.2. The position $X = 0.0 \text{ mm}$ was defined on the centerline of the tube, with raster scans taken from $X = -1.5 \text{ mm}$ to 1.5 mm at 0.5 mm intervals. Vertical steps in the Y direction were 1 mm over the length of the tube. Translation of the tube around the fixed beam was accomplished by mounting the vacuum chamber onto precision step motors that moved the vacuum chamber in the X and Y directions. The tube remained fixed with respect to the beam axis Z . $Y = 0.0 \text{ mm}$ was defined as the upstream edge of the downstream electrode, see Fig. 5.1. Full raster scans (0.5 mm steps from $X = -1.5$ to 1.5 mm) took about 8 hours for each Y position.

Figure 5.3 shows a sample signal from the fluorescence detector. Peaks from Compton and elastic scattering are observed along with the Kr fluorescence signal. These are primarily due to the

stainless steel chamber walls, excited by scattering X-rays, or due to contaminants in the pencil lead source of graphite used to alter the resistance of the tube (see Experimental section of Chapter 1). Calibration attempts were made by operating the tube under incompressible flow conditions (i.e. slowly eluting Kr/He mixture through the tube at atmospheric pressure). Buildup of Kr in the chamber, however, made extraction of calibration signal difficult. In future attempts, the SiC tube will be capped and loaded with known amount of Kr/He to obtain a calibration curve that can be used in extraction of absolute Kr densities.

5.3 Results

The analysis of absorption signal is straight forward, and described in great detail here [148]. A detailed composite radiograph is shown in Figure 5.4 where X-ray absorption by the tube at 15 keV is evident. The upstream edge of the downstream electrode is the black vertical line on the left side of the image. The lightest gray color at the top and the bottom of the image highlight the edges of the tube, hence the light color due to lack of absorption. The darker horizontal lines represent the tube walls, with the bottom wall in this image clearly thicker than the wall shown on top. A raster scan image of the absorption signal from room temperature tube #1 is shown in Figure 5.5a, and in 5.5b the same image is shown with an external wall temperature of 1090 K. Here the background is in black, and the SiC is shown absorbing incoming X-rays in yellow orange and red. The white spot on the right side of Fig. 5b located at $Y = -12$ mm is absorption due to the thermocouple, which reoriented itself a bit upon heating. These two images are essentially a vertical cross section of the SiC tube, with the tube inlet located at the most negative Y values. The geometry of the tube leads to the longest path-length, and therefore most X-ray absorption, to be through the walls in the Z direction (same direction as the beam). The thicker wall in this image is shown on the right hand side, highlighted in yellow and white. In contrast, the thinner wall is located on the left. The tube interior is clearly not smooth, with bumps on the order of $0.1 \times$ tube i.d.

Figure 5.6 shows the extracted fluorescence signal from within the tube, again at room temperature (5.6a) and 1090 K (5.6b). This was a bit more challenging to obtain because as can be seen in Fig. 5.3, the tail of the Compton scattering interferes with the comparatively weak Kr signal. For details on extraction of the fluorescence signal, see 5.5. The black horizontal lines in these images

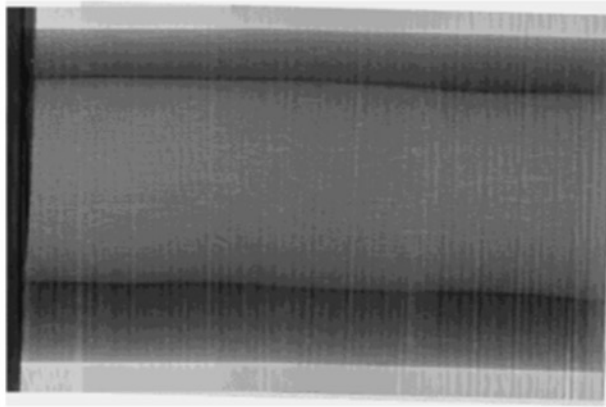


Figure 5.4: Composite radiograph of the SiC tube #1. The upstream edge of the downstream electrode is in the image in black on the left edge.

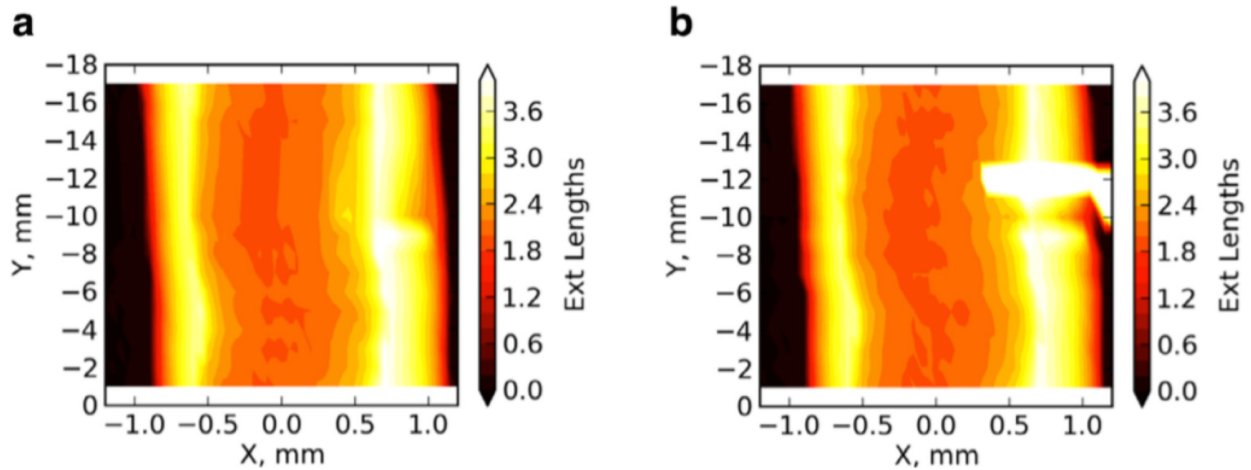


Figure 5.5: Absorption raster scans of SiC tube #1, gas flow is in the $Y = -18 \text{ mm} \rightarrow Y = 0 \text{ mm}$ direction. External wall temperature measured by Type K thermocouple: a) 300 K and b) 1090 K. The tube exit is a few mm downstream towards $Y = +3 \text{ mm}$; the bottom of this image is the upstream edge of the downstream electrode. SiC wall thickness is highlighted in yellow and white, with the wall on the right being thicker than on the left.

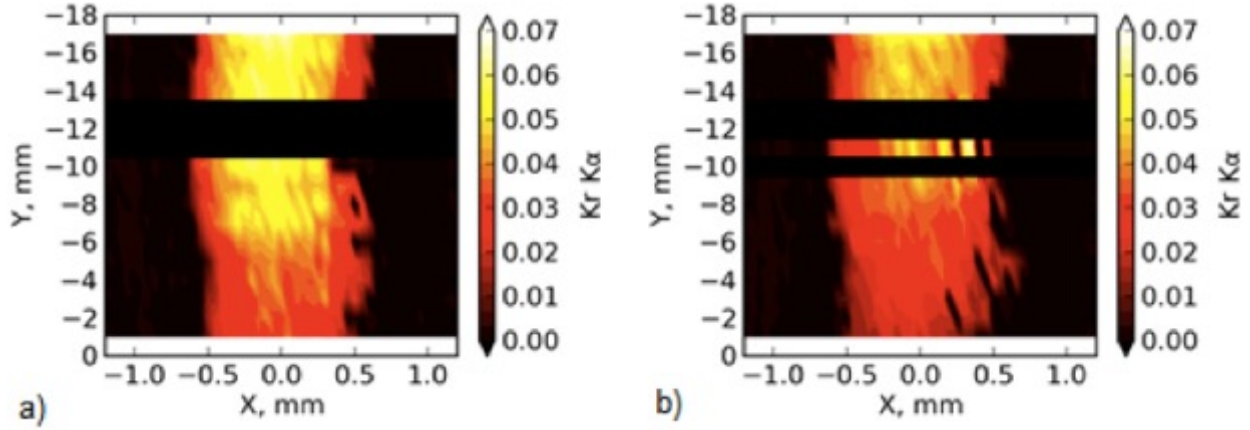


Figure 5.6: Krypton fluorescence images captured at the same time as absorption images shown in Fig. 5.5. The black horizontal lines are regions obscured by the thermocouple. Gas mixture is 67% Kr diluted in He by Mass. a) 300 K and b) 1090 K.

are due to absorption of fluorescent photons by the thermocouple wrap. It is clear that the signal decreases as the gas flows downstream (towards $Y = 0$). This is consistent with calculations by Guan et. al. [61], and is due to the fact that the gas is expanding (becoming less dense) as it passes through the SiC tube toward the vacuum chamber exit. Caution should be taken when evaluating these images however, because the entire tube is an absorber. As the beam moves away from $X = 0$, the cylindrical geometry of the tube leads to a longer effective path length for the incident X-ray beam to travel through (longest path length at the walls around $X = \pm 0.75$ mm), which will also increase the overall X-ray absorption.

A plot is shown in Figure 5.7 of the X integrated Kr fluorescence signal with respect to each Y position. It is very clear here again that the gas density is decreasing towards the tube exit. The rate of this decrease in density is considerably greater for the tube at 1090 K than at 300 K. This indicated greater expansion of the gas, again consistent with calculations by Guan et. al. [61].

Figure 5.8 is a composite image of the absorption and fluorescence data. The background in this image has been reduced to a single shade (black) to allow the tube walls, indicated in light blue, to be seen clearly. The non-uniformity of the tube wall thickness is very prominent in this composite image. It is clear that the gas flow is heavily influenced by the wall shape as well. There appears to be a thin layer of low density gas flush against the walls of the reactor, perhaps a boundary layer. There are also pockets of low density gas following divets in the walls of the reactor, particularly in

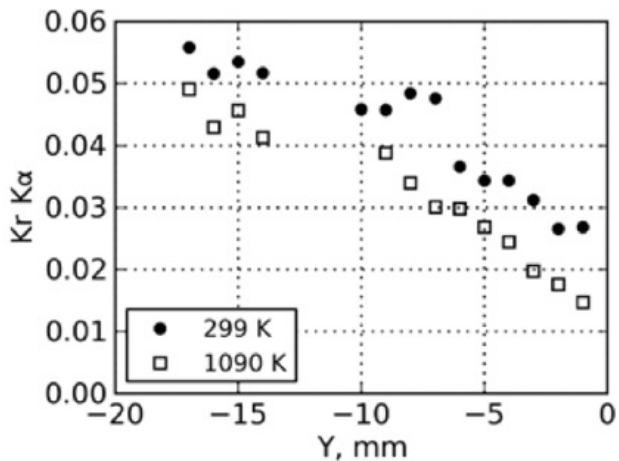


Figure 5.7: Integration of relative Kr density across X as a function of vertical position Y .

the bottom right half of Fig 5.8.

Raster scans were also taken of the jet eluting from the reactor, see Figure 5.9. Tube #1 eventually developed a hole, and tube #2 was used for images of the expanding jet. The pressure differential (see P_{inlet} and P_{outlet} on Table 5.1) at the entrance and exit of the tube was not large enough for a true supersonic jet to form, although it should be noted that chamber pressure and outlet pressure will not be identical. The conditions of this experiment most likely lie somewhere between an effusive and supersonic jet. The strong jet, shifted slightly towards the positive X , persists for roughly 2 mm before dissipating for several millimeters. Above room temperature, images show a similar structure. An additional takeaway from this experiment is that the ideal location for the skimmer in PIMS experiments under these experimental conditions is within 1-2 mm of the tube exit if maximum signal is to be obtained. This is much closer than expected for a true supersonic jet.

5.4 Conclusions

Gas density maps have been successfully obtained for the first time with XRF of krypton inside a heated, opaque SiC micro-reactor. This is also the first time images of such a low pressure jet have been taken. Useful information about the flowfields inside the reactor have been obtained, as well an evaluation of the non-uniformity of the SiC tube interior. Quantitative data can be made with a

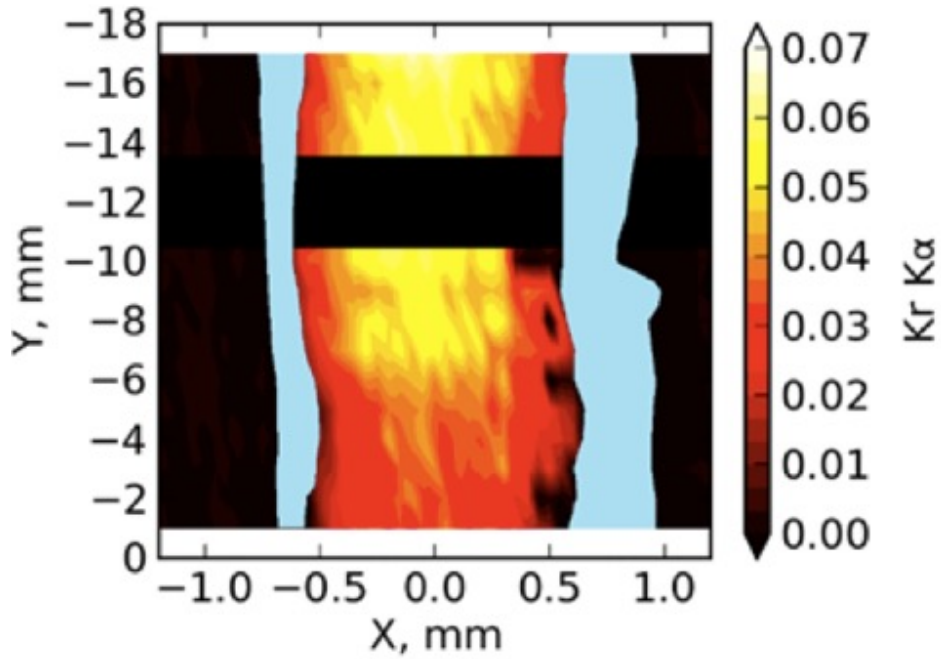


Figure 5.8: Composite image of Kr fluorescence and X-ray absorption data. Vertical blue lines represent absorption due to walls of SiC tube, vertical black is the background, and horizontal black line is absorption due to the thermocouple. Kr fluorescence is shown increasing from black to red to yellow to white. The tube exit is around $Y = +3$ mm; this image stops at $Y = 0$ mm at the upstream edge of the downstream electrode.

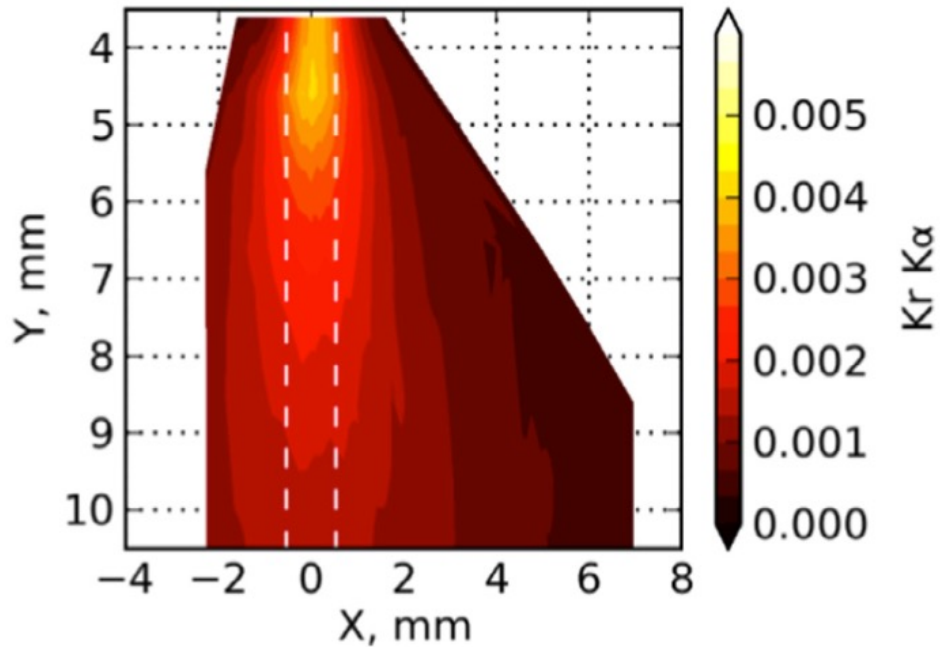


Figure 5.9: Composite image of Kr fluorescence and X-ray absorption data

few modifications to the experiment. A tube with uniform wall thickness and smooth wall interior would improve the signal trapping model. Calibrations could be made by capping the end of the tube and filling it with a known gas mixture. X-ray tomography would be well-suited for providing high resolution tube density in three dimensions and improving the signal trapping model. Removal of the Compton scattering that is adjacent to the Kr fluorescence peak could be achieved using an Se- or Br- containing filter between the reactor and the detector. Chemically pure graphite could remove some of the interfering fluorescent signal as well. Higher energy X-rays could be used, with lower absorption through the SiC walls, and the fluorescent detector could be placed closer to the reactor. With these improvements, it seems likely that density measurements with $\pm 5\%$ precision or better are possible in future measurements. This will effectively make the SiC an invaluable tool not only useful for chemical decomposition studies, but also for rate determination studies that are important if this chemistry is to be applied to further studies on combustion.

Bibliography

- [1] W. Acree Jr and J. S. Chickos. Phase Transition Enthalpy Measurements of Organic and Organometallic Compounds. Sublimation, Vaporization and Fusion Enthalpies from 1880 to 2010. *Journal of Physical and Chemical Reference Data*, 39(4):043101, 2010.
- [2] H. Afeefy, J. Liebman, S. Stein, W. Mallard, and P. Linstrom. NIST Standard Reference Database Number 69. *Mallard, W. G*, 1997.
- [3] M. Akbar Ali and A. Violi. Reaction pathways for the thermal decomposition of methyl butanoate. *The Journal of Organic Chemistry*, 78(12):5898–5908, 2013.
- [4] C. J. Annesley, C. F. Goldsmith, and R. S. Tranter. A shock tube laser schlieren study of methyl acetate dissociation in the fall-off regime. *Physical Chemistry Chemical Physics*, 16(16):7241–7250, 2014.
- [5] J. Baldt and H. K. K. Hall Jr. Thermochemistry of strained-ring bridgehead nitriles and esters. *Journal of the American Chemical Society*, 93(1):140–145, 1971.
- [6] J. Baraban, D. David, G. B. Ellison, and J. Daily. An optically accessible pyrolysis microreactor. *Review of Scientific Instruments*, 87(1):014101, 2016.
- [7] J. E. Bartmess, J. A. Scott, and R. T. McIver Jr. Scale of acidities in the gas phase from methanol to phenol. *Journal of the American Chemical Society*, 101(20):6046–6056, 1979.
- [8] J. A. Bearden and A. F. Burr. Reevaluation of x-ray atomic energy levels. *Review of Modern Physics*, 39:125–142, Jan 1967.

- [9] F. Benoit, A. Harrison, and F. Lossing. Hydrogen migrations in mass spectrometry. III—Energetics of formation of $[R\ CO_2H_2]^+$ in the mass spectra of $R\ CO_2R$. *Organic Mass Spectrometry*, 12(2):78–82, 1977.
- [10] M. Berger and J. Hubbell. NBSIR 87-3597: Photon cross-sections on a personal computer. National Institute of Standards, Gaithersburg. MD 20899, USA; 1987.
- [11] J. Berkowitz. Photoionization of CH_3OH , CD_3OH , and CH_3OD : Dissociative ionization mechanisms and ionic structures. *The Journal of Chemical Physics*, 69(7):3044–3054, 1978.
- [12] G. Bieri, F. Burger, E. Heilbronner, and J. P. Maier. Valence ionization energies of hydrocarbons. *Helvetica Chimica Acta*, 60(7):2213–2233, 1977.
- [13] E. M. Bilger and H. Hibbert. Mechanism of Organic Reactions. IV. Pyrolysis of Esters and Acetals. *Journal of the American Chemical Society*, 58(5):823–826, 1936.
- [14] S. J. Blanksby and G. B. Ellison. Bond dissociation energies of organic molecules. *Accounts of chemical research*, 36(4):255–263, 2003.
- [15] J. A. Blush, P. Chen, R. T. Wiedmann, and M. G. White. Rotationally resolved threshold photoelectron spectrum of the methyl radical. *The Journal of chemical physics*, 98(4):3557–3559, 1993.
- [16] H. Bock, T. Hirabayashi, and S. Mohmand. Gasphasen-Reaktionen, 21. Thermische Erzeugung von Alkyl-und Halogenketenen. *Chemische Berichte*, 114(7):2595–2608, 1981.
- [17] Y. J. Bomble, J. Vázquez, M. Kállay, C. Michauk, P. G. Szalay, A. G. Császár, J. Gauss, and J. F. Stanton. High-accuracy extrapolated ab initio thermochemistry. II. Minor improvements to the protocol and a vital simplification. *The Journal of chemical physics*, 125(6):064108, 2006.
- [18] M. Boot, P. Frijters, C. Luijten, B. Somers, R. Baert, A. Donkerbroek, R. J. Klein-Douwel, and N. Dam. Cyclic oxygenates: A new class of second-generation biofuels for diesel engines. *Energy & Fuels*, 23(4):1808–1817, 2008.

- [19] A. Bouchez, L. Margulès, R. Motiyenko, J.-C. Guillemin, A. Walters, S. Bottinelli, C. Ceccarelli, and C. Kahane. The submillimeter spectrum of deuterated glycolaldehydes. *Astronomy & Astrophysics*, 540:A51, 2012.
- [20] G. Bouchoux, F. Penaud-Berruyer, and W. Bertrand. Structure, thermochemistry and reactivity of protonated glycolaldehyde. *European Journal of Mass Spectrometry*, 7(4-5):351–358, 2001.
- [21] G. T. Buckingham, T. K. Ormond, J. P. Porterfield, P. Hemberger, O. Kostko, M. Ahmed, D. J. Robichaud, M. R. Nimlos, J. W. Daily, and G. B. Ellison. The thermal decomposition of the benzyl radical in a heated micro-reactor. I. Experimental findings. *The Journal of Chemical Physics*, 142(4):044307, 2015.
- [22] G. T. Buckingham, J. P. Porterfield, O. Kostko, T. P. Troy, M. Ahmed, D. J. Robichaud, M. R. Nimlos, J. W. Daily, and G. B. Ellison. The thermal decomposition of the benzyl radical in a heated micro-reactor. II. Pyrolysis of the tropylium radical. *The Journal of Chemical Physics*, 145(1):014305, 2016.
- [23] M. Buehl, R. Kramme, H.-D. Martin, B. Mayer, and G. Nowack. Chromophoric Systems. Part 1. Conformation and Absorption of Light in Hexa-1, 5-diene-3, 4-dione (Divinylglyoxal). *ChemInform*, 22(25), 1991.
- [24] A. Burrill and P. Johnson. Torsional analyses of trans-2-butene and propene cations: A comparative investigation of two prototypical ions with different degrees of symmetry. *The Journal of chemical physics*, 115(1):133–138, 2001.
- [25] L. Carlsen, H. Egsgaard, and P. Pagsberg. Gas-phase thermolyses. Part 5. Thermally-induced rearrangement of methyl acetate in the gas phase. *Journal of the Chemical Society, Perkin Transactions 2*, (9):1256–1259, 1981.
- [26] P. B. Carroll, B. J. Drouin, and S. L. W. Weaver. The submillimeter spectrum of glycolaldehyde. *The Astrophysical Journal*, 723(1):845, 2010.

- [27] P. B. Carroll, B. A. McGuire, D. P. Zaleski, J. L. Neill, B. H. Pate, and S. L. W. Weaver. The pure rotational spectrum of glycolaldehyde isotopologues observed in natural abundance. *Journal of Molecular Spectroscopy*, 284:21–28, 2013.
- [28] J. Ceponkus, W. Chin, M. Chevalier, M. Broquier, A. Limongi, and C. Crépin. Infrared study of glycolaldehyde isolated in parahydrogen matrix. *The Journal of chemical physics*, 133(9):094502, 2010.
- [29] O. L. Chapman, M. D. Miller, and S. M. Pitzenberger. Infrared spectroscopy of matrix-isolated propadienone. *Journal of the American Chemical Society*, 109(22):6867–6868, 1987.
- [30] B. Cocksey, J. Eland, and C. Danby. The effect of alkyl substitution on ionisation potential. *Journal of the Chemical Society B: Physical Organic*, pages 790–792, 1971.
- [31] L. Coniglio, H. Bennadji, P. A. Glaude, O. Herbinet, and F. Billaud. Combustion chemical kinetics of biodiesel and related compounds (methyl and ethyl esters): experiments and modeling—advances and future refinements. *Progress in Energy and Combustion Science*, 39(4):340–382, 2013.
- [32] C. Costain. Determination of molecular structures from ground state rotational constants. *The Journal of Chemical Physics*, 29(4):864–874, 1958.
- [33] J. D. Cox and G. Pilcher. Thermochemistry of organic and organometallic compounds. 1970.
- [34] C. J. Cramer and D. G. Truhlar. Quantum chemical conformational analysis of 1, 2-ethanediol: Correlation and solvation effects on the tendency to form internal hydrogen bonds in the gas phase and in aqueous solution. *Journal of the American Chemical Society*, 116(9):3892–3900, 1994.
- [35] L. S. Crocker. Thermochemical investigation of carbonyl compounds by reaction calorimetry. *PhD Thesis, Yale Univ.*, 1989.
- [36] G. da Silva, C.-H. Kim, and J. W. Bozzelli. Thermodynamic properties (enthalpy, bond energy, entropy, and heat capacity) and internal rotor potentials of vinyl alcohol, methyl vinyl ether, and their corresponding radicals. *The Journal of Physical Chemistry A*, 110(25):7925–7934, 2006.

- [37] P. Dagaut, N. Smoucovit, M. Cathonnet, et al. Methyl acetate oxidation in a JSR: Experimental and detailed kinetic modeling study. *Combustion Science and Technology*, 127(1):275–292, 1997.
- [38] P. De Mayo and D. Verdun. Flash thermolysis. IV. Thermal fragmentation of cyclohexanone. *Journal of the American Chemical Society*, 92(20):6079–6080, 1970.
- [39] M. J. Dewar and L. E. Wade Jr. A study of the mechanism of the Cope rearrangement. *Journal of the American Chemical Society*, 99(13):4417–4424, 1977.
- [40] S. Dooley, H. J. Curran, and J. M. Simmie. Autoignition measurements and a validated kinetic model for the biodiesel surrogate, methyl butanoate. *Combustion and Flame*, 153(1):2–32, 2008.
- [41] A. M. El-Nahas, M. V. Navarro, J. M. Simmie, J. W. Bozzelli, H. J. Curran, S. Dooley, and W. Metcalfe. Enthalpies of formation, bond dissociation energies and reaction paths for the decomposition of model biofuels: ethyl propanoate and methyl butanoate. *The Journal of Physical Chemistry A*, 111(19):3727–3739, 2007.
- [42] A. Engdahl and B. Nelander. Infrared spectrum of cis-glyoxal. *Chemical physics letters*, 148(2):264–268, 1988.
- [43] J. Espinosa-García and S. Dóbé. Theoretical enthalpies of formation for atmospheric hydroxy-carbonyls. *Journal of Molecular Structure*, 713(1):119–125, 2005.
- [44] M. Evans and C.-Y. Ng. Rotationally resolved pulsed field ionization photoelectron bands for CO^+ ($X, v^+= 0-42$) in the energy range of 13.98-21.92 eV. *Journal of Chemical Physics*, 111(LBNL-44116), 1999.
- [45] A. Farooq, D. Davidson, R. Hanson, L. Huynh, and A. Violi. An experimental and computational study of methyl ester decomposition pathways using shock tubes. *Proceedings of the Combustion Institute*, 32(1):247–253, 2009.
- [46] A. Farooq, W. Ren, K. Y. Lam, D. F. Davidson, R. K. Hanson, and C. K. Westbrook. Shock tube studies of methyl butanoate pyrolysis with relevance to biodiesel. *Combustion and Flame*, 159(11):3235–3241, 2012.

- [47] E. M. Fisher, W. J. Pitz, H. J. Curran, and C. K. Westbrook. Detailed chemical kinetic mechanisms for combustion of oxygenated fuels. *Proceedings of the Combustion Institute*, 28(2):1579–1586, 2000.
- [48] R. A. Fletcher and G. Pilcher. Measurements of heats of combustion by flame calorimetry. Part 6.—Formaldehyde glyoxal. *Transactions of the Faraday Society*, 66:794–799, 1970.
- [49] L. Fredin, B. Nelander, and G. Ribbegård. On the dimerization of carbon dioxide in nitrogen and argon matrices. *Journal of Molecular Spectroscopy*, 53(3):410–416, 1974.
- [50] G. Friedrichs, M. Colberg, J. Dammeier, T. Bentz, and M. Olzmann. HCO formation in the thermal unimolecular decomposition of glyoxal: rotational and weak collision effects. *Physical Chemistry Chemical Physics*, 10(43):6520–6533, 2008.
- [51] M. J. Frisch. Gaussian. 2003.
- [52] S. Gail, S. Sarathy, M. Thomson, P. Diévar, and P. Dagaut. Experimental and chemical kinetic modeling study of small methyl esters oxidation: Methyl (E)-2-butenate and methyl butanoate. *Combustion and Flame*, 155(4):635–650, 2008.
- [53] S. Gail, M. J. Thomson, S. M. Sarathy, S. A. Syed, P. Dagaut, P. Diévar, A. J. Marchese, and F. L. Dryer. A wide-ranging kinetic modeling study of methyl butanoate combustion. *Proceedings of the Combustion Institute*, 31(1):305–311, 2007.
- [54] H. Gao, Y. Xu, L. Yang, C.-S. Lam, H. Wang, J. Zhou, and C. Ng. High-resolution threshold photoelectron study of the propargyl radical by the vacuum ultraviolet laser velocity-map imaging method. *The Journal of Chemical Physics*, 135(22):224304, 2011.
- [55] I. García-Moreno and C. B. Moore. Spectroscopy of methylene: Einstein coefficients for CH₂ (b 1B₁– \tilde{a} 1A₁) transitions. *The Journal of chemical physics*, 99(9):6429–6435, 1993.
- [56] P. A. Glaude, W. J. Pitz, and M. J. Thomson. Chemical kinetic modeling of dimethyl carbonate in an opposed-flow diffusion flame. *Proceedings of the Combustion Institute*, 30(1):1111–1118, 2005.

- [57] W. A. Goddard III and L. B. Harding. The description of chemical bonding from ab initio calculations. *Annual Review of Physical Chemistry*, 29(1):363–396, 1978.
- [58] W. Gordy and R. Cook. Microwave molecular spectra interscience publications. *New York*, page 587, 1970.
- [59] R. Grana, A. Frassoldati, A. Cuoci, T. Faravelli, and E. Ranzi. A wide range kinetic modeling study of pyrolysis and oxidation of methyl butanoate and methyl decanoate. Note I: Lumped kinetic model of methyl butanoate and small methyl esters. *Energy*, 43(1):124–139, 2012.
- [60] R. Grana, A. Frassoldati, C. Saggese, T. Faravelli, and E. Ranzi. A wide range kinetic modeling study of pyrolysis and oxidation of methyl butanoate and methyl decanoate—Note II: Lumped kinetic model of decomposition and combustion of methyl esters up to methyl decanoate. *Combustion and Flame*, 159(7):2280–2294, 2012.
- [61] Q. Guan, K. N. Urness, T. K. Ormond, D. E. David, G. Barney Ellison, and J. W. Daily. The properties of a micro-reactor for the study of the unimolecular decomposition of large molecules. *International Reviews in Physical Chemistry*, 33(4):447–487, 2014.
- [62] J. P. Guthrie. Hydration of carboxamides. Evaluation of the free energy change for addition of water to acetamide and formamide derivatives. *Journal of the American Chemical Society*, 96(11):3608–3615, 1974.
- [63] M. E. Harding, J. Vázquez, B. Ruscic, A. K. Wilson, J. Gauss, and J. F. Stanton. High-accuracy extrapolated ab initio thermochemistry. III. Additional improvements and overview. *The Journal of chemical physics*, 128(11):114111, 2008.
- [64] D. Hartley. Chemiluminescent recombination of formyl radicals. *Chemical Communications (London)*, (24):1281–1282, 1967.
- [65] I. Haykal, R. Motiyenko, L. Margulès, and T. Huet. Millimeter and submillimeter wave spectra of ¹³C-glycolaldehydes. *Astronomy & Astrophysics*, 549:A96, 2013.
- [66] W. J. Hehre. Spartan '08. 2009.

- [67] J. Hine and A. W. Klueppel. Structural effects on rates and equilibria. XVIII. Thermodynamic stability of ortho esters. *Journal of the American Chemical Society*, 96(9):2924–2929, 1974.
- [68] L. K. Huynh and A. Violi. Thermal decomposition of methyl butanoate: Ab initio study of a biodiesel fuel surrogate. *The Journal of Organic Chemistry*, 73(1):94–101, 2008.
- [69] D. E. Johnstone and J. R. Sodeau. Photochemistry of the matrix-isolated α , β -unsaturated aldehydes acrolein, methacrolein and crotonaldehyde at 4.2 K. *Journal of the Chemical Society, Faraday Transactions*, 88(3):409–415, 1992.
- [70] A. Kastengren, C. F. Powell, E. M. Dufresne, and D. A. Walko. Application of X-ray fluorescence to turbulent mixing. *Journal of Synchrotron Radiation*, 18(5):811–815, Sep 2011.
- [71] J. Kiefer, K. Gupte, L. Harding, and S. Klippenstein. Shock tube and theory investigation of cyclohexane and 1-hexene decomposition. *The Journal of Physical Chemistry A*, 113(48):13570–13583, 2009.
- [72] J. H. Kiefer and J. N. Shah. Unimolecular dissociation of cyclohexene at extremely high temperatures: behavior of the energy-transfer collision efficiency. *Journal of Physical Chemistry*, 91(11):3024–3030, 1987.
- [73] R. Klein-Douwel, A. Donkerbroek, A. Van Vliet, M. Boot, L. Somers, R. Baert, N. Dam, and J. Ter Meulen. Soot and chemiluminescence in diesel combustion of bio-derived, oxygenated and reference fuels. *Proceedings of the Combustion Institute*, 32(2):2817–2825, 2009.
- [74] D. Knowles and A. Nicholson. Ionization energies of formic and acetic acid monomers. *The Journal of Chemical Physics*, 60(3):1180–1181, 1974.
- [75] Y. Kobayashi, H. Takahara, H. Takahashi, and K. Higasi. Infrared and raman studies of the structure of crystalline glycolaldehyde. *Journal of Molecular Structure*, 32(2):235–246, 1976.
- [76] J. Kraitchman. Determination of molecular structure from microwave spectroscopic data. *American Journal of Physics*, 21(1):17–24, 1953.

- [77] A. Krantz, T. Goldfarb, and C. Lin. Simple method for assigning vibrational frequencies to rapidly equilibrating rotational isomers. *Journal of the American Chemical Society*, 94(11):4022–4024, 1972.
- [78] H. W. Kroto. *Molecular rotation spectra*. 1975.
- [79] K. Kumar and C.-J. Sung. Autoignition of methyl butanoate under engine relevant conditions. *Combustion and Flame*, 171:1–14, 2016.
- [80] J. Y. Lai, K. C. Lin, and A. Violi. Biodiesel combustion: Advances in chemical kinetic modeling. *Progress in Energy and Combustion Science*, 37(1):1 – 14, 2011.
- [81] G. E. Leroi, G. E. Ewing, and G. C. Pimentel. Infrared spectra of carbon monoxide in an argon matrix. *The Journal of Chemical Physics*, 40(8):2298–2303, 1964.
- [82] W. Liu, R. Sivaramakrishnan, M. J. Davis, S. Som, D. Longman, and T. Lu. Development of a reduced biodiesel surrogate model for compression ignition engine modeling. *Proceedings of the Combustion Institute*, 34(1):401–409, 2013.
- [83] M. Loudet, M. Grimaud, F. Metras, and G. Pfsierguillouzo. Intramolecular interactions in cyclohexane series. 2. photoelectron-spectra of 2-chlorocyclohexanones. *Journal of Molecular Structure*, 35(2):213–222, 1976.
- [84] A. Magalhães and P. Chalk. Determination of the purity of methyl nitrite. *Analytica Chimica Acta*, 182:251 – 255, 1986.
- [85] W. G. Mallard, J. H. Miller, and K. C. Smyth. The ns Rydberg series of 1, 3-trans-butadiene observed using multiphoton ionization. *The Journal of chemical physics*, 79(12):5900–5905, 1983.
- [86] K.-M. Marstokk and H. Møllendal. Microwave spectra of isotopic glycolaldehydes, substitution structure, intramolecular hydrogen bond and dipole moment. *Journal of Molecular Structure*, 16(2):259–270, 1973.
- [87] E. J. Martin. Investigations of structure-energy relationships by reaction calorimetry. *PhD Thesis, Yale Univ.*, 1984.

- [88] P. Masclet and G. Mouvier. Study of conjugated ethylenic aldehydes and ketones using photoelectric spectrometry. *Journal of Electron Spectroscopy and Related Phenomena*, 14(2):77–97, 1978.
- [89] L. R. McCunn, K.-C. Lau, M. J. Krisch, L. J. Butler, J.-W. Tsung, and J. J. Lin. Unimolecular dissociation of the CH₃OCO radical: an intermediate in the CH₃O+ CO reaction. *The Journal of Physical Chemistry A*, 110(4):1625–1634, 2006.
- [90] F. McLafferty, D. McAdoo, J. S. Smith, and R. Kornfeld. Metastable ions characteristics. XVIII. Enolic C₃H₆O⁺ ion formed from aliphatic ketones. *Journal of the American Chemical Society*, 93(15):3720–3730, 1971.
- [91] F. W. McLafferty. *Interpretation of Mass Spectra*. University Science Books, Mill Valley, CA 94941, third edition, 1980.
- [92] D. A. McQuarrie and J. D. Simon. *Molecular thermodynamics*, volume 450. University Science Books Sausalito, CA, 1999.
- [93] W. K. Metcalfe, S. Dooley, H. J. Curran, J. M. Simmie, A. M. El-Nahas, and M. V. Navarro. Experimental and modeling study of C₅H₁₀O₂ ethyl and methyl esters. *The Journal of Physical Chemistry A*, 111(19):4001–4014, 2007.
- [94] H. Michelsen and P. Klaboe. Spectroscopic studies of glycolaldehyde. *Journal of Molecular Structure*, 4(2):293–302, 1969.
- [95] I. M. Mills. 3.2 Vibration-Rotation Structure in Asymmetric-and Symmetric-Top Molecules. *Molecular Spectroscopy: Modern Research*, 1:115, 1972.
- [96] V. Mohaček-Grošev, B. Prugovečki, S. Prugovečki, and N. Strukan. Glycolaldehyde dimer in the stable crystal phase has axial oh groups: Raman, infrared and x-ray data analysis. *Journal of Molecular Structure*, 1047:209–215, 2013.
- [97] C. B. Moore and G. C. Pimentel. Infrared spectrum and vibrational potential function of ketene and the deuterated ketenes. *The Journal of Chemical Physics*, 38(12):2816–2829, 1963.

- [98] C. E. Moore. Selected Tables of Atomic Spectra, Atomic Energy Levels. Multiplet Tables N IV, NV, N VI, N VII. Technical report, DTIC Document, 1971.
- [99] K. M. Morgan, J. A. Ellis, J. Lee, A. Fulton, S. L. Wilson, P. S. Dupart, and R. Dastoori. Thermochemical studies of epoxides and related compounds. *The Journal of organic chemistry*, 78(9):4303–4311, 2013.
- [100] M. Mucha and Z. Mielke. Complexes of atmospheric α -dicarbonyls with water: FTIR matrix isolation and theoretical study. *The Journal of Physical Chemistry A*, 111(12):2398–2406, 2007.
- [101] C. V. Naik, C. K. Westbrook, O. Herbinet, W. J. Pitz, and M. Mehl. Detailed chemical kinetic reaction mechanism for biodiesel components methyl stearate and methyl oleate. *Proceedings of the Combustion Institute*, 33(1):383–389, 2011.
- [102] D. Y. Nakaji. An ab initio study of the effects of hetero-substitution on π -interactions, and, calorimetry of nitrogen containing heterocycles. *PhD Thesis, Yale Univ.*, 1992.
- [103] S. Nandi, P. A. Arnold, B. K. Carpenter, M. R. Nimlos, D. C. Dayton, and G. B. Ellison. Polarized infrared absorption spectra of matrix-isolated allyl radicals. *The Journal of Physical Chemistry A*, 105(32):7514–7524, 2001.
- [104] B. Nelander. A matrix isolation study of the water-formaldehyde complex. The far-infrared region. *Chemical Physics*, 159(2):281–287, 1992.
- [105] T. L. Nguyen and J. R. Barker. Sums and densities of fully coupled anharmonic vibrational states: A comparison of three practical methods. *The Journal of Physical Chemistry A*, 114(10):3718–3730, 2010.
- [106] T. L. Nguyen, M. C. McCarthy, and J. F. Stanton. Relatively selective production of the simplest Criegee intermediate in a CH₄/O₂ electric discharge: Kinetic analysis of a plausible mechanism. *The Journal of Physical Chemistry A*, 2014.
- [107] B. Niu, Y. Bai, and D. A. Shirley. High resolution photoelectron spectroscopy and femtosecond intramolecular dynamics of H₂CCO⁺ and D₂CCO⁺. *The Journal of chemical physics*, 99(4):2520–2532, 1993.

- [108] R. Nuttall, A. Laufer, and M. Kilday. The enthalpy of formation of ketene. *The Journal of Chemical Thermodynamics*, 3(2):167–174, 1971.
- [109] J. W. Ochterski, G. A. Petersson, and J. A. Montgomery Jr. A complete basis set model chemistry. V. Extensions to six or more heavy atoms. *The Journal of chemical physics*, 104(7):2598–2619, 1996.
- [110] T. K. Ormond, A. M. Scheer, M. R. Nimlos, D. J. Robichaud, T. P. Troy, M. Ahmed, J. W. Daily, T. L. Nguyen, J. F. Stanton, and G. B. Ellison. Pyrolysis of cyclopentadienone: Mechanistic insights from a direct measurement of product branching ratios. *The Journal of Physical Chemistry A*, 2015.
- [111] P. Osswald, U. Struckmeier, T. Kasper, K. Kohse-Höinghaus, J. Wang, T. A. Cool, N. Hansen, and P. R. Westmoreland. Isomer-specific fuel destruction pathways in rich flames of methyl acetate and ethyl formate and consequences for the combustion chemistry of esters. *The Journal of Physical Chemistry A*, 111(19):4093–4101, 2007.
- [112] A. Parandaman, M. Balaganesh, and B. Rajakumar. Experimental and theoretical study on thermal decomposition of methyl butanoate behind reflected shock waves. *RSC Advances*, 5(105):86536–86550, 2015.
- [113] B. I. Parsons and C. Hinshelwood. The oxidation of hydrocarbons and their derivatives. Part II. Structural effects in the ester series. *J. Chem. Soc.*, pages 1799–1803, 1956.
- [114] J. Pedley, R. Naylor, and S. Kirby. Thermochemistry of organic compounds. *Chapman and Hall, New York*, 1986.
- [115] M. Petitjean, E. Reyès-Pérez, D. Perez, P. Mirabel, and S. Le Calve. Vapor pressure measurements of hydroxyacetaldehyde and hydroxyacetone in the temperature range (273 to 356) K. *Journal of Chemical & Engineering Data*, 55(2):852–855, 2009.
- [116] S. L. Peukert, R. Sivaramakrishnan, M.-C. Su, and J. V. Michael. Experiment and theory on methylformate and methylacetate kinetics at high temperatures: Rate constants for H-atom abstraction and thermal decomposition. *Combustion and Flame*, 159(7):2312–2323, 2012.

- [117] J. P. Porterfield, J. H. Baraban, T. P. Troy, M. Ahmed, M. C. McCarthy, K. M. Morgan, J. W. Daily, T. L. Nguyen, J. F. Stanton, and G. B. Ellison. Pyrolysis of the Simplest Carbohydrate, Glycolaldehyde (CHO-CH₂OH), and Glyoxal in a Heated Microreactor. *The Journal of Physical Chemistry A*, 120(14):2161–2172, 2016.
- [118] J. P. Porterfield, T. L. Nguyen, J. H. Baraban, G. T. Buckingham, T. P. Troy, O. Kostko, M. Ahmed, J. F. Stanton, J. W. Daily, and G. B. Ellison. Isomerization and Fragmentation of Cyclohexanone in a Heated Micro-Reactor. *The Journal of Physical Chemistry A*, 119(51):12635–12647, 2015.
- [119] S. Pratt, P. Dehmer, and J. Dehmer. Zero-kinetic-energy photoelectron spectroscopy from the A 1Au state of acetylene: Renner–Teller interactions in the trans-bending vibration of C₂H⁺. *The Journal of chemical physics*, 99(9):6233–6244, 1993.
- [120] S. Ptasińska, S. Denifl, P. Scheier, and T. D. Märk. Electron impact ionization of glycolaldehyde. *International Journal of Mass Spectrometry*, 243(2):171–176, 2005.
- [121] F. Qiu, Y. Li, D. Yang, X. Li, and P. Sun. Biodiesel production from mixed soybean oil and rapeseed oil. *Applied Energy*, 88(6):2050–2055, 2011.
- [122] R. C. Reid, J. M. Prausnitz, and B. E. Poling. *The properties of gases and liquids*. 1987.
- [123] W. Ren, K.-Y. Lam, D. F. Davidson, R. K. Hanson, and X. Yang. Pyrolysis and oxidation of methyl acetate in a shock tube: A multi-species time-history study. *Proceedings of the Combustion Institute*, 2016.
- [124] J. C. Rienstra-Kiracofe, G. S. Tschumper, H. F. Schaefer, S. Nandi, and G. B. Ellison. Atomic and molecular electron affinities: photoelectron experiments and theoretical computations. *Chemical Reviews*, 102(1):231–282, 2002.
- [125] F. D. Rossini. Assignment of uncertainties to thermochemical data. *Experimental Thermochemistry*, 1:297–320, 1956.
- [126] a. Ruscic and J. Berkowitz. Photoionization mass spectrometric studies of the isomeric transient species cd₂oh and cd₃o. *The Journal of Chemical Physics*, 95(6):4033–4039, 1991.

- [127] B. Ruscic, J. E. Boggs, A. Burcat, A. G. Császár, J. Demaison, R. Janoschek, J. M. Martin, M. L. Morton, M. J. Rossi, J. F. Stanton, et al. IUPAC critical evaluation of thermochemical properties of selected radicals. Part I. *Journal of physical and chemical reference data*, 34(2):573–656, 2005.
- [128] S. Sarathy, S. Gail, S. Syed, M. Thomson, and P. Dagaut. A comparison of saturated and unsaturated c 4 fatty acid methyl esters in an opposed flow diffusion flame and a jet stirred reactor. *Proceedings of the Combustion Institute*, 31(1):1015–1022, 2007.
- [129] A. M. Scheer, C. Mukarakate, D. J. Robichaud, M. R. Nimlos, H.-H. Carstensen, and G. B. Ellison. Unimolecular thermal decomposition of phenol and d5-phenol: Direct observation of cyclopentadiene formation via cyclohexadienone. *The Journal of chemical physics*, 136(4):044309, 2012.
- [130] A. Schulenburg, M. Meisinger, P. Radi, and F. Merkt. The formaldehyde cation: Rovibrational energy level structure and coriolis interaction near the adiabatic ionization threshold. *Journal of Molecular Spectroscopy*, 250(1):44–50, 2008.
- [131] W. R. Schwartz, C. S. McEnally, and L. D. Pfefferle. Decomposition and hydrocarbon growth processes for esters in non-premixed flames. *The Journal of Physical Chemistry A*, 110(21):6643–6648, 2006.
- [132] M. Schwell, F. Gaie-Levrel, Y. Bénilan, M.-C. Gazeau, N. Fray, G. Saul, N. Champion, S. Leach, and J.-C. Guillemin. VUV spectroscopy and photochemistry of five interstellar and putative prebiotic molecules. *EAS Publications Series*, 58:301–306, 2012.
- [133] Z. Serinyel, C. Togbé, A. Zaras, G. Dayma, and P. Dagaut. Kinetics of oxidation of cyclohexanone in a jet-stirred reactor: Experimental and modeling. *Proceedings of the Combustion Institute*, 35(1):507–514, 2015.
- [134] T. Shimanouchi. Tables of Molecular Vibrational Frequencies Consolidated. Volume I. Technical report, DTIC Document, 1972.
- [135] T. Shimanouchi. Tables of molecular vibrational frequencies. Consolidated volume II. *Journal of Physical and Chemical Reference Data*, 6(3):993–1102, 1977.

- [136] J. M. Simmie and H. J. Curran. Energy Barriers for the Addition of H, CH₃, and C₂H₅ to CH₂=CHX [X=H, CH₃, OH] and for H-Atom Addition to RCH=O [R=H, CH₃, C₂H₅, n-C₃H₇]: Implications for the Gas-Phase Chemistry of Enols. *The Journal of Physical Chemistry A*, 113(27):7834–7845, 2009.
- [137] I. W. Smith and A. Ravishankara. Role of hydrogen-bonded intermediates in the bimolecular reactions of the hydroxyl radical. *The Journal of Physical Chemistry A*, 106(19):4798–4807, 2002.
- [138] J. F. Stanton, J. Gauss, M. E. Harding, and P. G. Szalay. CFOUR, Coupled-Cluster Techniques for Computational Chemistry. 2015.
- [139] A. Streitwieser, E. M. Kosower, and C. Heathcock. *Introduction to organic chemistry*. Prentice Hall, Upper Saddle River, NJ, 4th edition, 1977.
- [140] K. Sulzmann, D. Baxter, M. Khazra, and T. Lund. Initiation of methyl acetate pyrolysis in argon-diluted mixtures behind reflected shock waves. *The Journal of Physical Chemistry*, 89(16):3561–3566, 1985.
- [141] S. Sunner and I. Wadsö. On the design and efficiency of isothermal reaction calorimeters. *Acta Chem. Scand*, 13:97–108, 1959.
- [142] C. A. Taatjes, N. Hansen, A. McIlroy, J. A. Miller, J. P. Senosiain, S. J. Klippenstein, F. Qi, L. Sheng, Y. Zhang, T. A. Cool, et al. Enols are common intermediates in hydrocarbon oxidation. *Science*, 308(5730):1887–1889, 2005.
- [143] A. Tajti, P. G. Szalay, A. G. Császár, M. Kállay, J. Gauss, E. F. Valeev, B. A. Flowers, J. Vázquez, and J. F. Stanton. HEAT: High accuracy extrapolated ab initio thermochemistry. *The Journal of chemical physics*, 121(23):11599–11613, 2004.
- [144] T. Tan, X. Yang, Y. Ju, and E. A. Carter. Ab Initio Unimolecular Reaction Kinetics of CH₂C(=O)OCH₃ and CH₃(C=O)OCH₂ Radicals. *The Journal of Physical Chemistry A*, 119(42):10553–10562, 2015.

- [145] H. Tao and K. C. Lin. Pathways, kinetics and thermochemistry of methyl-ester peroxy radical decomposition in the low-temperature oxidation of methyl butanoate: A computational study of a biodiesel fuel surrogate. *Combustion and Flame*, 161(9):2270–2287, 2014.
- [146] R. G. Tonkyn, J. W. Winniczek, and M. G. White. Rotationally resolved photoionization of O_2^+ near threshold. *Chemical physics letters*, 164(2):137–142, 1989.
- [147] R. S. Tranter, A. W. Jasper, J. B. Randazzo, J. P. Lockhart, and J. P. Porterfield. Recombination and dissociation of 2-methyl allyl radicals: Experiment and theory. *Proceedings of the Combustion Institute*, *accepted*, 2016.
- [148] R. S. Tranter, A. L. Kastengren, J. P. Porterfield, J. B. Randazzo, J. P. Lockhart, J. H. Baraban, and G. B. Ellison. Measuring flow profiles in heated miniature reactors with x-ray fluorescence spectroscopy. *Proceedings of the Combustion Institute*, 2016.
- [149] W. Tsang. Heats of formation of organic free radicals by kinetic methods. In *Energetics of organic free radicals*, pages 22–58. Springer, 1996.
- [150] V. Tumanov, E. Kromkin, and E. Denisov. Estimation of dissociation energies of C—H bonds in oxygen-containing compounds from kinetic data for radical abstraction reactions. *Russian Chemical Bulletin*, 51(9):1641–1650, 2002.
- [151] F. Tureček. 2-hydroxybutadiene: Preparation, ionization energy and heat of formation. *Tetrahedron letters*, 25(45):5133–5134, 1984.
- [152] K. N. Urness, Q. Guan, A. Golan, J. W. Daily, M. R. Nimlos, J. F. Stanton, M. Ahmed, and G. B. Ellison. Pyrolysis of furan in a microreactor. *The Journal of chemical physics*, 139(12):124305, 2013.
- [153] H. Van Dam and A. Oskam. He (I) and He (II) photoelectron spectra of some substituted ethylenes. *Journal of Electron Spectroscopy and Related Phenomena*, 13(3):273–290, 1978.
- [154] A. Vasiliou, K. M. Piech, X. Zhang, M. R. Nimlos, M. Ahmed, A. Golan, O. Kostko, D. L. Osborn, J. W. Daily, J. F. Stanton, et al. The products of the thermal decomposition of CH_3CHO . *The Journal of chemical physics*, 135(1):014306, 2011.

- [155] A. K. Vasiliou, J. H. Kim, T. K. Ormond, K. M. Piech, K. N. Urness, A. M. Scheer, D. J. Robichaud, C. Mukarakate, M. R. Nimlos, J. W. Daily, et al. Biomass pyrolysis: thermal decomposition mechanisms of furfural and benzaldehyde. *The Journal of chemical physics*, 139(10):104310, 2013.
- [156] A. K. Vasiliou, K. M. Piech, B. Reed, X. Zhang, M. R. Nimlos, M. Ahmed, A. Golan, O. Kostko, D. L. Osborn, D. E. David, et al. Thermal decomposition of CH₃CHO studied by matrix infrared spectroscopy and photoionization mass spectroscopy. *The Journal of chemical physics*, 137(16):164308, 2012.
- [157] L.-S. Wang, J. Reutt, Y. Lee, and D. Shirley. High resolution UV photoelectron spectroscopy of CO₂⁺, COS⁺ and CS₂⁺ using supersonic molecular beams. *Journal of electron spectroscopy and related phenomena*, 47:167–186, 1988.
- [158] Y. L. Wang, D. J. Lee, C. K. Westbrook, F. N. Egolfopoulos, and T. T. Tsotsis. Oxidation of small alkyl esters in flames. *Combustion and Flame*, 161(3):810–817, 2014.
- [159] K. Watanabe, T. Nakayama, and J. Mottl. Ionization potentials of some molecules. *Journal of Quantitative Spectroscopy and Radiative Transfer*, 2(4):369–382, 1962.
- [160] C. K. Westbrook. Biofuels combustion. *Annual review of physical chemistry*, 64:201–219, 2013.
- [161] C. K. Westbrook, W. J. Pitz, P. R. Westmoreland, F. L. Dryer, M. Chaos, P. Oßwald, K. Kohse-Höinghaus, T. A. Cool, J. Wang, B. Yang, et al. A detailed chemical kinetic reaction mechanism for oxidation of four small alkyl esters in laminar premixed flames. *Proceedings of the combustion institute*, 32(1):221–228, 2009.
- [162] K. B. Wiberg. Accuracy of calculations of heats of reduction/hydrogenation: Application to some small ring systems. *The Journal of organic chemistry*, 77(22):10393–10398, 2012.
- [163] K. B. Wiberg, L. S. Crocker, and K. M. Morgan. Thermochemical studies of carbonyl compounds. 5. Enthalpies of reduction of carbonyl groups. *Journal of the American Chemical Society*, 113(9):3447–3450, 1991.

- [164] K. B. Wiberg and R. F. Waldron. Lactones. 2. Enthalpies of hydrolysis, reduction, and formation of the C4-C13 monocyclic lactones. Strain energies and conformations. *Journal of the American Chemical Society*, 113(20):7697–7705, 1991.
- [165] R. Wiedmann, R. Tonkyn, M. White, K. Wang, and V. McKoy. Rotationally resolved threshold photoelectron spectra of OH and OD. *The Journal of chemical physics*, 97(2):768–772, 1992.
- [166] S. Willitsch, U. Hollenstein, and F. Merkt. Ionization from a double bond: Rovibronic photoionization dynamics of ethylene, large amplitude torsional motion and vibronic coupling in the ground state of C2H4+. *Journal of Chemical Physics*, 120(4):1761–1774, 2004.
- [167] T. Wolf and D. M. Rosie. Pyrolysis-gas chromatography of simple organic molecules. *Analytical Chemistry*, 39(7):725–729, 1967.
- [168] X. Xing, M.-K. Bahng, B. Reed, C.-S. Lam, K.-C. Lau, and C.-Y. Ng. Rovibrationally selected and resolved pulsed field ionization-photoelectron study of propyne: ionization energy and spin-orbit interaction in propyne cation. *The Journal of chemical physics*, 128(9):094311–094311, 2008.
- [169] X. Xing, B. Reed, M.-K. Bahng, and C.-Y. Ng. Infrared-vacuum ultraviolet pulsed field ionization-photoelectron study of C2H4+ using a high-resolution infrared laser. *The Journal of Physical Chemistry A*, 112(12):2572–2578, 2008.
- [170] X. Xing, B. Reed, K.-C. Lau, C. Ng, X. Zhang, and G. B. Ellison. Vacuum ultraviolet laser pulsed field ionization-photoelectron study of allyl radical CH2CHCH2. *The Journal of chemical physics*, 126(17):171101–171101, 2007.
- [171] X. Yang, D. Felsmann, N. Kurimoto, J. Krüger, T. Wada, T. Tan, E. A. Carter, K. Kohse-Höinghaus, and Y. Ju. Kinetic studies of methyl acetate pyrolysis and oxidation in a flow reactor and a low-pressure flat flame using molecular-beam mass spectrometry. *Proceedings of the Combustion Institute*, 35(1):491–498, 2015.
- [172] X. Yang, B. Yan, H.-f. Xu, R.-h. Zhu, M.-x. Zhang, and D.-j. Ding. Analysis of potential energy surface for butanone isomerization. *Chinese Journal of Chemical Physics*, 26(5):519–525, 2013.

- [173] Z. Yang, L. Wang, Y. Lee, D. Shirley, S. Huang, and W. Lester. Molecular beam photoelectron spectroscopy of allene. *Chemical Physics Letters*, 171(1):9–13, 1990.
- [174] M. Zamanpour, A. Bahkshandeh, S. Ghaffarzadeh, and J. Dyke. Observation and assignment of the first photoelectron band of the CH₃CO (X 2A) radical. *Journal of Electron Spectroscopy and Related Phenomena*, 162(3):122–126, 2008.
- [175] A. M. Zaras, P. Dagaut, and Z. Serinyel. Computational kinetic study for the unimolecular decomposition pathways of cyclohexanone. *The Journal of Physical Chemistry A*, 2014.
- [176] X.-M. Zhang, D. Malick, and G. A. Petersson. Enolization enthalpies for aliphatic carbonyl and thiocarbonyl compounds. *The Journal of Organic Chemistry*, 63(16):5314–5317, 1998.
- [177] Z. Zhang, E. Hu, C. Peng, X. Meng, Y. Chen, and Z. Huang. Shock tube measurements and kinetic study of methyl acetate ignition. *Energy & Fuels*, 29(4):2719–2728, 2015.